Electron spins in semiconductor quantum dots

Electron spins in semiconductor quantum dots

Proefschrift

ter verkrijging van de graad van doctor
aan de Technische Universiteit Delft,
op gezag van de Rector Magnificus prof.dr.ir. J.T. Fokkema,
voorzitter van het College voor Promoties,
in het openbaar te verdedigen ten overstaan van een commissie,
door het College voor Promoties aangewezen,

op woensdag 23 februari 2005 om 10.30 uur

door

Ronald HANSON

natuurkundig ingenieur
geboren te Groningen.

Dit proefschrift is goedgekeurd door de promotor:
  Prof. dr. ir. L. P. Kouwenhoven

Samenstelling van de promotiecommissie:

Rector Magnificus,	voorzitter
Prof. dr. ir. L. P. Kouwenhoven	Technische Universiteit Delft, promotor
Prof. dr. G. Abstreiter	Technische Universität München, Duitsland
Prof. dr. G. E. W. Bauer	Technische Universiteit Delft
Prof. dr. C. W. J. Beenakker	Universiteit Leiden
Prof. dr. ir. J. E. Mooij	Technische Universiteit Delft
Prof. dr. ir. B. J. van Wees	Universiteit Groningen
Dr. Y. Hirayama	NTT Basic Research Laboratories, Japan

Preface

This thesis describes the results of four years of experimental research on electron spins on quantum dots in the Quantum Transport group of Leo Kouwenhoven and Hans Mooij. This research has been carried out in a small team, and some excellent people have contributed to these results. At the same time, I have had the freedom (and the privilege) to develop and prove myself on every element of the research cycle: creating ideas for an experiment, fabricating the nanodevices, cooling them down to 10 mK and performing measurements on them, analyzing and publishing the results and finally presenting these results at international conferences at beautiful locations. Looking back, I can't help thinking of the typical job demands of today's 'high-potentials' (as spelled out in every company's recruiting folder): 'solving complex problems in a creative environment with a steep learning curve, in a team with highly intelligent and inspiring people'. The past four years could not have been described any better.

Since this thesis is the result of a team effort, I owe much to everyone who has contributed to it. First of all, I thank my advisor Leo Kouwenhoven for the excellent mix of (in chronological order) guidance, freedom and responsibility I have received during the four years. I sincerely hope your funding successes will not stop you from using your huge knowledge in the lab (and on the football field).

When I started my PhD, the team working on quantum dots consisted of the Kondo heroes Silvano de Franceschi, Wilfred van der Wiel and Jeroen Elzerman. Silvano taught me the basics of quantum dots and of dilution fridge operation. His determination and knowledge, displayed during my first (and last) Kondo experiment, have had a major impact on the rest of my PhD. I thank 'Willie' for giving me directions on the 'royal road' to device fabrication. 'Jero' Elzerman has been a very important person during my PhD, both scientifically and as a friend. I have especially enjoyed our frequent discussions, which have sprouted ideas and solutions crucial to the success of many experiments. Laurens and Lieven joined the team about three years ago, when Wilfred and Silvano left. Laurens started as my 'fabrication apprentice', but single-handedly succeeded in fabricating the first Delft few-electron dots. He also carried on the vital Japan-link (but how

come some Thai kids have curly blond hair?). Lieven was the quantum computing knowledge source that we desperately needed three years ago, and has developed to become one on quantum dots too, in a surprisingly short time. Thanks for the many important contributions. The new guys, Frank and Ivo, will have to carry the torch in the coming years. Ivo, I am convinced that the days and nights we spent in the lab during Christmas holidays, without the ESR reward, will be compensated for by many successes during your PhD. Frank, good luck in the Overhauser fields!

Our collaboration with Prof. Tarucha and Dr. Hirayama has been of great importance to this work. I have spent two fruitful springs in Dr. Hirayama's group at NTT Basic Research Labs in Atsugi (Japan), where I learned the tricks of device fabrication from Toshiaki Hayashi and Toshimasa Fujisawa. I thank Dr. Hirayama for this kind hospitality. Our research has benefitted enormously from the pioneering work of Fujisawa *et al.*, and I am very grateful for the help and many useful discussions during the years. Furthermore, I thank T. Saku for growing the wafers, Mike Stopa for simulations and discussions (over a beer or two), Hashi for the 'social activities' and all the other people at NTT and at Tokyo University for assistance and discussions. Especially, I would like to acknowledge Prof. Tarucha who, in spite of his busy schedule, always took the time to discuss the most basic issues with me. Doumo arigatou gozaimashita!

The theorists in the Basel group of Daniel Loss (especially Hansres Engel, Guido Burkard and Vitaly Golovach) have all been very valuable for my understanding and the stimulation of ideas. Daniel, your input, directly and indirectly via your students, has been of tremendous value. David DiVincenzo spent a couple of months in our group, and I would like to thank him for the many exchanges of ideas about possible experiments and theoretical insight. Also, I have benefitted greatly from discussions with the theorists in Delft, especially with Siggi Erlingsson, Oleg Jouravlev, Miriam Blaauboer and Yuli Nazarov. Furthermore, I thank Lingxiao Zhang and Prof. Leburton for the simulations on our devices. Finally, I'd like to acknowledge Josh Folk and Xuedong Hu for many (email) discussions.

Many undergraduate students have chosen to do their research project on quantum dots: Joris Wijpkema, Jabob Greidanus, Jort Wever, Benoit Witkamp, Ivo Vink and Wouter Naber. I've learned a lot from supervising you and working with you. It's especially nice to see that two of 'my' students are now doing a PhD in our group. (While the others are stuffing their bank accounts!) Good luck to all of you!

The Quantum Transport group offers a lot more besides quantum dot research. Hans Mooij has managed to create a very stimulating and active environment,

Contents

Chapter 1

Introduction

1.1 Motivation

The world as we experience it in our daily lives is well described by classical theories, such as Newtonian mechanics, that were developed before the 20th century. It came therefore as a huge surprise that, when scientists started investigating ever smaller and smaller units of matter, they stumbled onto very weird behaviour of small particles and light that could not be explained at all by these classical theories.

From the initial confusion, the theory of quantum mechanics emerged in the 1920s. It ascribes to all particles a wave function, responsible for intriguing effects such as energy quantization and interference. This quantum theory was very successful in explaining some of the major puzzles of that time, such as the photo-electric effect and the stability of atoms – in fact, the whole periodic system of the elements! The theory has been used to explain phenomena in many other fields, and has yielded well-known applications such as lasers and Magnetic Resonance Imaging (MRI). Actually, most scientists today believe that quantum mechanics is the true fundamental theory of nature, of which the classical theories just represent a limiting case. How exactly the 'macroscopic' classical world that we experience emerges from the 'microscopic' quantum world, however, is still subject of debate [1].

These days, the computer chip industry is about to experience the same transition as science did in the early 20th century. As transistors are made smaller and smaller, a world is entered that does not obey the classical laws of physics. Certainly, the famous Moore's law, which states that the number of transistors on integrated circuits (a rough measure of computer processing power) doubles every 18 months, will not hold any longer when transistors reach the size of individual atoms [2]. Indeed, gate leakage currents due to quantum-mechanical tunneling

1

already pose one of the most difficult hurdles for further decreasing the transistor size.

Rather than viewing the quantum-mechanical behaviour as a problem, we might also ask ourselves whether it is possible to actually *use* quantum mechanics for computing. One approach is to integrate a quantum property in a classical computing scheme. For example, the field of *spintronics* aims to use the spin degree of freedom of electrons as a carrier of classical information (bits) [3]. Alternatively, we might try to build a computer that exploits the unique features of quantum mechanics to perform computations that are not possible classically: a true *quantum computer*.

The research described in this thesis constitutes a first step towards a small-scale quantum computer where the spins of electrons serve as quantum bits, the basic building blocks of a quantum computer. In the next sections, the concept of quantum computing is explained, and the basic ingredients for implementing quantum bits with electron spins confined in quantum dots are outlined.

1.2   Quantum computing

In 1982, Richard Feynman speculated [4] that quantum systems might be able to perform certain tasks more efficiently than would be possible in classical systems. Important theoretical breakthroughs in the 1980s and 1990s have led to a realistic idea of what a quantum computer should look like. Before we continue discussing the quantum computer, we need to understand two important concepts from quantum mechanics: superpositions and entanglement.

Unlike a classical two-level system, which is always either in state 0 or in state 1, a quantum two-level system can be in an arbitrary *superposition* of states $|0\rangle$ and $|1\rangle$: $\alpha|0\rangle + \beta|1\rangle$, where $|\alpha|^2 + |\beta|^2 = 1$. The evolution of this system is deterministic, as it is governed by a first-order differential equation – the Schrödinger equation. However, coupling this quantum system to a measurement apparatus forces it into one of the possible measurement eigenstates in an apparently non-deterministic way: the particular measurement outcome is random, only the probability for each outcome can be determined [5]. In the case of the above superposition state, the probability for measuring $|0\rangle$ is $|\alpha|^2$, and for $|1\rangle$ is $|\beta|^2$. The question of what exactly constitutes a measurement, which seems to be closely related to the transition from quantum to classical behaviour, is not fully understood [6].

The second property of quantum mechanics that is needed is one which has sprouted controversy for many years: *entanglement*. By interacting with each

other, two quantum two-level systems can become entangled, which means that we can not fully describe one system independently of the other. For example, the state $(|01\rangle - |10\rangle)/\sqrt{2}$ gives a complete description of the whole system, but the two subsystems do not have a definite state. Due to this strong connection between the two systems, a measurement made on one, which forces it into one of the two states $|0\rangle$ or $|1\rangle$, immediately influences the state of the other, even though it may be arbitrarily far away. People have questioned whether it is not just a lack of our knowledge of some 'hidden variable' that hinders the prediction of a measurement outcome. However, measurements on so-called EPR pairs of photons (named after a landmark thought experiment by Einstein, Podolsky and Rosen [7]) have clearly shown that the non-local correlations between the photons are significantly larger than permitted by any local hidden-variable theory [8, 9]. Thus, entanglement is real, and constitutes one of the essential resources for quantum computing.

Using the concepts of superposition and entanglement, we now give a simplified view of the difference between a classical and a quantum computer in Fig. 1.1. A one-bit classical computer is a machine that takes one input value, 0 or 1, and computes the corresponding output value, $f(0)$ or $f(1)$. A quantum computer with one quantum bit (or 'qubit') could take as an input value a superposition of $|0\rangle$ and $|1\rangle$, and due to the linearity of quantum mechanics the output would be a superposition of $F|0\rangle$ and $F|1\rangle$. So, in a sense it has performed two calculations
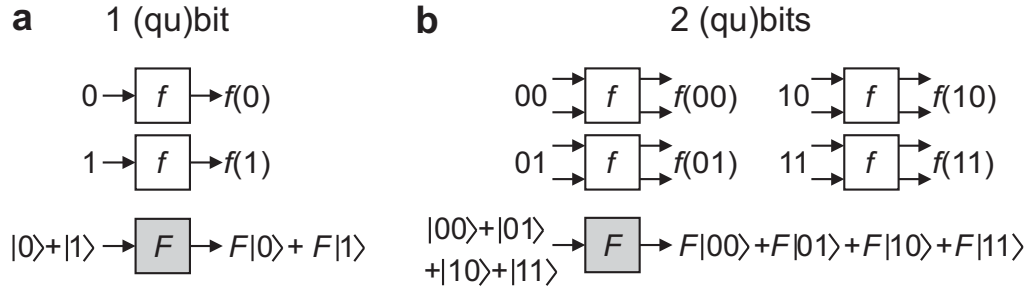
Figure 1.1: Difference between a classical and a quantum computer. **(a)** To determine the function f for the two possible input states 0 and 1, a one-bit classical computer needs to evaluate the function twice, once for every input state. In contrast, a one-qubit quantum computer can have a superposition of $|0\rangle$ and $|1\rangle$ as an input, to end up in a superposition of the two output values, $F|0\rangle$ and $F|1\rangle$. It has taken only half the number of steps as its classical counterpart. **(b)** Similarly, a two-qubit quantum computer needs only a quarter of the number of steps that are required classically. The computing power of a quantum computer scales exponentially with the number of qubits, for a classical computer the scaling is only linear.

in a single step. For a two-qubit system, the gain becomes even more significant: now the input can be a superposition of four states, so the quantum computer can perform four calculations in one step. The operation on many input states simultaneously is termed 'quantum parallelism' and is at the heart of quantum computing. In fact, it can be proved [10] that the computing power of a quantum computer scales exponentially with the number of qubits, whereas this scaling is only linear for a classical computer.

It might appear that a fundamental problem has been overlooked: according to quantum mechanics, a superposition of possible measurement outcomes can only exist before it is measured, and the measurement gives only one actual outcome. The exponential computing power thus appears inaccessible. However, by using carefully tailored quantum algorithms, an exponential speed-up can be achieved for some problems such as factoring integers [11] or simulating a quantum system [12]. For other tasks, such as searching a database, a quadratic speed-up is possible [13]. Using such quantum algorithms, a quantum computer can indeed be far more efficient than a classical one, performing tasks that a classical computer could not possibly finish before the sun will burn up the earth. As thinking about quantum algorithms has only barely begun, it is not unreasonable to assume that more applications of quantum computing will be discovered in the future.

Another fundamental issue is the interaction of the quantum system with the (uncontrolled) environment, which inevitably disturbs the desired quantum evolution. This process, known as 'decoherence', results in errors in the computation. Additional errors are introduced by imperfections in the quantum operations that are applied. All these errors propagate, and after some time the state of the computer will be significantly different from what it should be. It would seem that this prohibits any long computations, making it impossible for a quantum computer to use its exponential power for a non-trivial task. Fortunately, it has been shown that methods to detect and correct any errors exist [14, 15], keeping the computation on track. Of course, such methods only help if the error rate is small enough, since otherwise the correction operations create more errors than they remove. This sets a so-called 'accuracy threshold' [16, 17], which is currently believed to be around 10^{-4}. If the error per quantum operation is smaller than this threshold, any errors can be corrected and an arbitrarily long computation is possible.

Due to the development of quantum algorithms and error correction, quantum computation is feasible from a theoretical point of view. The challenge is building an actual quantum computer with a sufficiently large number of coupled qubits. Probably, more than a hundred qubits will be required for useful computations,

but a system of about thirty qubits might already be able to perform valuable simulations of quantum systems.

1.3 Electron spin as a quantum bit

Any quantum two-level system can in principle function as a qubit, but for a scalable quantum computer a number of additional features are required [18]. Essentially, we have to reconcile the conflicting demands of good access to the quantum system (in order to perform fast and reliable operations or measurements) with sufficient isolation from the environment (for long coherence times). Current state-of-the-art is a seven-bit quantum computer, built up from the nuclear spins of molecules in a liquid solution. In this system, Shor's factoring algorithm has been demonstrated on the number 15 using nuclear magnetic resonance (NMR) techniques [19]. Practical limitations do not allow the NMR approach to be scaled up to more than about ten qubits. Therefore, many other implementations are currently being studied (a frequently updated overview of the progress on the different implementations can be found at Ref. [20]).

Typically, microscopic systems such as atoms or ions have good coherence properties, but are not easily accessible or scalable; on the other hand, larger systems such as solid-state devices can be accessed and scaled more easily, but often lack a long coherence time. A solid-state device with a long coherence time would represent the best of both worlds.

Precisely such a system was proposed by Loss and DiVincenzo [21] in 1997: the spin orientation of a single electron trapped in a semiconductor quantum dot. We outline the basic ingredients of this proposal below.

An electron spin can point 'up' or 'down' with respect to an external magnetic field. These eigenstates, $|\uparrow\rangle$ and $|\downarrow\rangle$, correspond to the two basis states of the qubit.

The electron is trapped on a quantum dot, which is basically a small electrically defined box with a discrete energy spectrum. The quantum dots that we use are defined by metal 'gate' electrodes on top of a semiconductor (GaAs/AlGaAs) heterostructure (see Fig. 1.2). At the interface between GaAs and AlGaAs, conduction band electrons accumulate that can only move in the lateral direction. Applying negative voltages to the gates locally depletes this two-dimensional electron gas underneath. The resulting gated quantum dots are very controllable and versatile systems, which can be manipulated and probed electrically. With the external magnetic field, B, we can tune the Zeeman splitting, $\Delta E_Z = g\mu_B B$, where $g \approx -0.44$ is the g-factor of GaAs, and $\mu_B = 9.27 \times 10^{-24}$ J/T is the Bohr
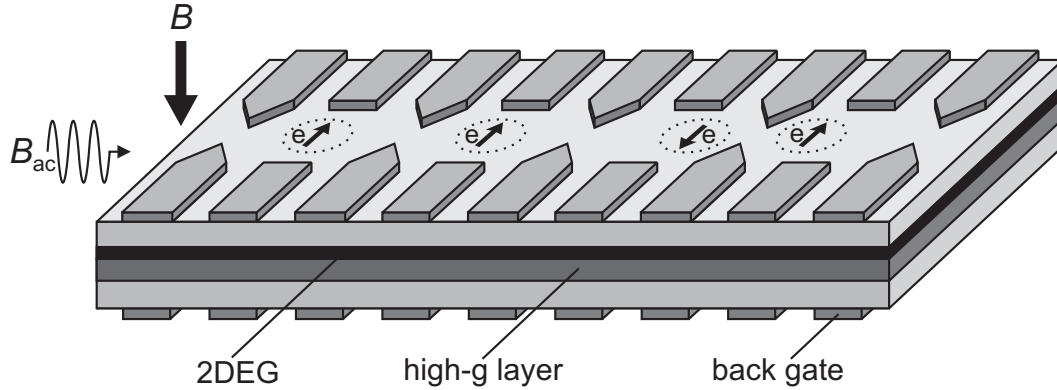
Figure 1.2: Schematic picture of the electron spin quantum computer as proposed by Loss and DiVincenzo [21]. The array of metal electrodes on top of a semiconductor heterostructure, containing a two-dimensional electron gas (2DEG) below the surface, defines a number of quantum dots (dotted circles), each holding a single electron spin (arrow). A magnetic field, B, induces a Zeeman splitting between the spin-up and spin-down states of each electron spin. The spin state is controlled either via an oscillating magnetic field, B_{ac} (on resonance with the Zeeman splitting), or via an oscillating electric field created with the back gates, which can pull the electron wavefunction into a layer with a large g-factor. Coupling between two spins is controlled by changing the voltage on the electrodes between the two dots. (Adapted from Ref. [21].)

magneton. In this way, we can control the energy levels of the qubit.

To perform single-qubit operations, we can apply a microwave magnetic field on resonance with the Zeeman splitting, i.e. with a frequency $f = \Delta E_Z / h$, where h is Planck's constant. The oscillating magnetic component perpendicular to the static magnetic field B results in a spin nutation. By applying the oscillating field for a fixed duration, a superposition of $|\uparrow\rangle$ and $|\downarrow\rangle$ can be created. This magnetic technique is known as electron spin resonance (ESR).

Two-qubit operations can be carried out purely electrically, by varying the gate voltages that control the potential barrier between two dots. It has been shown [21] that the system of two electron spins on neighboring dots, S_1 and S_2, coupled via a tunnel barrier, can be mapped onto the Heisenberg exchange Hamiltonian $H = J\vec{S}_1 \cdot \vec{S}_2$. The strength of this interaction, J, depends on the wave function overlap of the electrons and can be controlled electrically. By turning the two-spin interaction on for a certain well-defined time, the two electron spins can be swapped or even entangled. With combinations of arbitrary single-spin rotations and the two-spin interaction, any quantum gate can be implemented [21].

A last crucial ingredient is a method to read out the state of the spin qubit. This implies measuring the spin orientation of a single electron – a daunting task,

since the electron spin magnetic moment is exceedingly small (equal to the Bohr magneton μ_B). Therefore, an indirect spin measurement is proposed [21]. First the spin orientation of the electron is correlated with its position, via 'spin-to-charge conversion'. Then an electrometer is used to measure the position of the charge, thereby revealing its spin. In this way, the problem of measuring the spin orientation has been replaced by the much easier measurement of charge.

The ideas of Loss and DiVincenzo have led to an enormous research effort aiming at implementing the different parts of the proposal. Currently, among the most active players in this rapidly moving field are the groups of prof. S. Tarucha (Tokyo University, Japan), dr. T. Fujisawa and dr. Y. Hirayama (NTT Basic Research Labs, Japan), Prof. J.P. Kotthaus (LUM München, Germany), prof. C.M. Marcus and Prof. R. Westervelt (Harvard University, USA), prof. M.A Kastner (MIT, USA), and prof. D. Goldhaber-Gordon (Stanford University, USA).

Finally, it should be stressed that our efforts to create a spin qubit are not purely application-driven. If we have the ability to control and read out a single electron spin, we are in a unique position to study the interaction of the spin with its environment. This may lead to a better understanding of decoherence, and will also allow us to study the semiconductor environment using the spin as a probe.

1.4   Outline of this thesis

This thesis describes a series of experiments aimed at understanding and controlling single electron spins confined in a semiconductor quantum dot, with the long-term goal of creating of a small-scale quantum computer.

We start with explaining the basic theory of quantum dots and the measurement techniques applied in this work. In chapter 3, the hardware for the experiments on electron spins is developed: a double quantum dot circuit with a voltage-tunable number of electrons, with an integrated charge detector. We show that using this charge detector, we can monitor single-electron tunneling in real time.

In the next two chapters, 4 and 5, we investigate the spin states of a one- and a two-electron quantum dot by measurements of electron transport through the dot. In chapter 4, we use an in-plane magnetic field to directly detect the Zeeman splitting of a single electron. Furthermore, we find a lower bound on the spin relaxation time of 50 μs, by using fast voltage pulses. In chapter 5, we demonstrate that a few-electron dot can be operated as an electrically tunable

bipolar spin filter.

In chapters 6 to 8, we use the charge detector for measurements in the regime of very weak dot-lead coupling, where we can resolve single-electron tunnel events in real time. First, a novel method is presented for finding the relevant dot parameters in this regime (chapter 6). Then, we demonstrate one of the key ingredients for a quantum computer: single-shot read-out of the spin states. To convert the spin information to charge information, we have exploited the spin-dependent energy (chapter 7), and spin-dependent tunnel rates (chapter 8), achieving a measurement visibility of more than 80%. Both for a single spin and for the two-electron spin states, we find that the relaxation can be very slow (relaxation times up to milliseconds). We find a strong magnetic field dependence that hints at spin-orbit interaction as the dominant relaxation mechanism.

The current status of the field and the remaining issues are discussed in the concluding chapter. Also, detailed measurement schemes for single-spin rotations and the two-spin SWAP operation are proposed. Finally, the possibility of performing a test of Bell's inequalities using present-day techniques is discussed.

References

[1] See e.g. A. J. Leggett, A. Garg, "Quantum mechanics versus macroscopic realism: Is the flux there when nobody looks?", Phys. Rev. Let. **54**, 857 (1985), and A.J. Leggett, "Testing the limits of quantum mechanics: motivation, state of play, prospects", J. Phys. Condens. Matter 14, R415 (2002).

[2] For up-to-date information and prospects, see the International Technology Roadmap for Semiconductors at http://public.itrs.net/.

[3] S.A. Wolf *et al.*, "Spintronics: A Spin-Based Electronics Vision for the Future", Science **294**, 1488 (2001).

[4] R.P. Feynman, *The Feynman Lectures on Computation*, edited by R.W. Allen and T. Hey (Perseus Publishing, 2000).

[5] R.P. Feynman, *The Feynman Lectures on Physics*, Vol. 3 (Addison Wesley, 1970).

[6] V.B. Braginsky and F.Y. Khalili, *Quantum Measurement* (Cambridge University Press, 1992).

[7] A. Einstein, B. Podolsky, and N. Rosen , "Can Quantum-Mechanical Description of Physical Reality Be Considered Complete?", Phys. Rev. **47**, 777 (1935).

[8] A. Aspect, P. Grangier, and G. Roger, "Experimental Realization of Einstein-Podolsky-Rosen-Bohm Gedankenexperiment: A New Violation of Bell's Inequalities", Phys. Rev. Lett. **49**, 91 (1982).

[9] J.S. Bell, "On the Einstein Podolsky Rosen paradox", *Physics* **1**, 195 (1964); S.J. Freedman and John Clauser, "Experimental test of local Hidden-variable Theories", Phys. Rev. Let. **28**, 14 (1972).

[10] D. Deutsch, "Quantum theory, the Church-Turing principle, and the universal quantum computer", Proc. R. Soc. Lond. A, 400 (1985).

[11] P.W. Shor, "Algorithms for quantum computation: discrete logarithms and factoring", in *Proceedings of 35th Annual Symposium on Foundations of Computer Science* (IEEE Press, 1994).

[12] S. Lloyd, "Universal quantum simulators", Science **273**, 1073 (1996).

[13] L.K. Grover, "Quantum mechanics helps in searching needle in a haystack", Phys. Rev. Lett. **79**, 325 (1997).

[14] P.W. Shor, "Fault-tolerant quantum computation", in *Proceedings of 37th Annual Symposium on Foundations of Computer Science*, 56 (IEEE Press, 1996).

[15] A.M. Steane, "Error correction codes in quantum information processing", Phys. Rev. Lett. **77**, 793 (1996).

[16] A.Y. Kitaev, "Quantum error correction with imperfect gates", in *Quantum Communication, Computing, and Measurement*, edited by A.S. Holevo, O. Hirota and C.M. Caves, 181 (Plenum Press, 1997).

[17] D. Aharonov and M. Ben-Or, "Fault-tolerant quantum computation with constant error rate", quant-ph/9906129 (1999).

[18] D.P. DiVincenzo, "The physical implementation of quantum computation", Fortschr. Phys. **48**, 771 (2000).

[19] L.M.K. Vandersypen *et al.*, "Experimental realization of Shor's quantum factoring algorithm using nuclear magnetic resonance", Nature **414**, 883 (2001).

[20] Quantum Information Science and Technology roadmapping project, available at http://qist.lanl.gov/.

[21] D. Loss and D.P. DiVincenzo, "Quantum computation with quantum dots", Phys. Rev. A **57**, 120 (1998).

Chapter 2

Theory, device fabrication and measurement techniques

2.1 Quantum dots

A quantum dot is simply a small box that can be filled with electrons. The box is coupled via tunnel barriers to a source and drain reservoir, with which particles can be exchanged (see Fig. 2.1). By attaching current and voltage probes to these reservoirs, we can measure the electronic properties of the dot. The dot is also coupled capacitively to one or more 'gate' electrodes, which can be used to tune the electrostatic potential of the dot with respect to the reservoirs. When the size of the dot is comparable to the wavelength of the electrons that occupy it, the system exhibits a discrete energy spectrum, resembling that of an atom. As a result, quantum dots behave in many ways as *artificial atoms* [1].

Because a quantum dot is such a general kind of system, there exist quantum
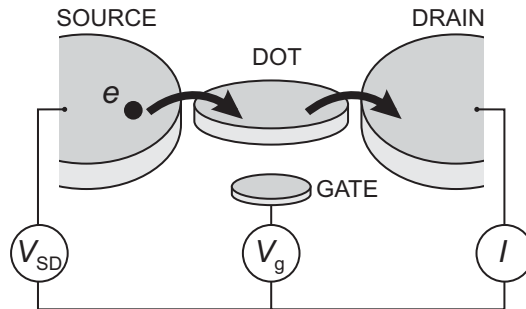
Figure 2.1: Schematic picture of a quantum dot in a lateral geometry. The quantum dot (represented by a disk) is connected to source and drain contacts via tunnel barriers, allowing the current through the device, I, to be measured in response to a bias voltage, V_{SD} and a gate voltage, V_g.

dots of many different sizes and materials: for instance single molecules trapped between electrodes, metallic or superconducting nanoparticles, self-assembled quantum dots, semiconductor lateral or vertical dots, and also semiconducting nanowires or carbon nanotubes between closely spaced electrodes. In this thesis, we focus on lateral (gated) semiconductor quantum dots [2]. These lateral devices allow all relevant parameters to be controlled *in situ*.

In this thesis, two different ways are used to probe the behavior of electrons on a quantum dot. We can measure the current due to transport of electrons through the dot, and we can use an electrometer to detect changes in the number of electrons on the dot. These experiments are conveniently understood using the constant interaction (CI) model [2].

2.1.1   Constant Interaction model

The CI model makes two important assumptions. First, the Coulomb interactions among electrons in the dot, and between electrons in the dot and those in the environment, are parameterized by a single, constant capacitance, C. This capacitance can be thought of as the sum of the capacitances between the dot and the source, C_S, the drain, C_D, and the gate, C_g: $C = C_S + C_D + C_g$. Second, the discrete energy spectrum can be described independently of the number of electrons on the dot. Under these assumptions the total energy of a N-electron dot in the ground state with the source-drain voltage, V_{SD}, applied to the source (and the drain grounded), is given by

$$U(N) = \frac{[-|e|(N - N_0) + C_S V_{SD} + C_g V_g]^2}{2C} + \sum_{n=1}^{N} E_n(B) \tag{2.1}$$

where $-|e|$ is the electron charge and N_0 the number of electrons in the dot at zero gate voltage, which compensates the positive background charge originating from the donors in the heterostructure. The terms $C_S V_{SD}$ and $C_g V_g$ can change continuously and represent the charge on the dot that is induced by the bias voltage (through the capacitance C_S) and by the gate voltage V_g (through the capacitance C_g), respectively. The last term of Eq. 2.1 is a sum over the occupied single-particle energy levels $E_n(B)$, which are separated by an energy $\Delta E_n = E_n - E_{n-1}$. These energy levels depend on the characteristics of the confinement potential. Note that, within the CI model, only these single-particle states depend on magnetic field, B.

To describe transport experiments, it is often more convenient to use the electrochemical potential. The electrochemical potential of the dot is by definition
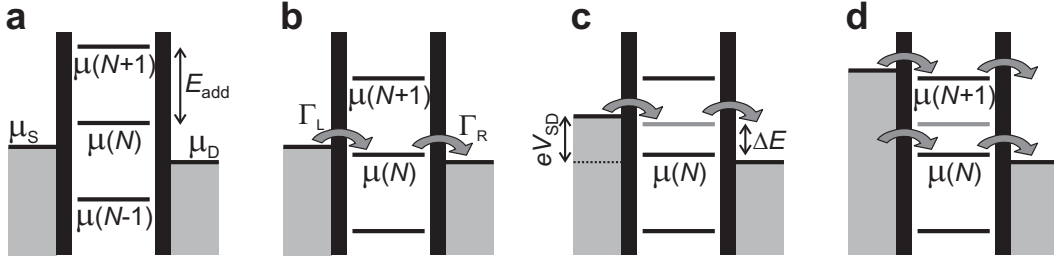
Figure 2.2: Schematic diagrams of the electrochemical potential of the quantum dot for different electron numbers. **(a)** No level falls within the bias window between μ_S and μ_D, so the electron number is fixed at $N-1$ due to Coulomb blockade. **(b)** The $\mu(N)$ level is aligned, so the number of electrons can alternate between N and $N-1$, resulting in a single-electron tunneling current. The magnitude of the current depends on the tunnel rate between the dot and the reservoir on the left, Γ_L, and on the right, Γ_R. **(c)** Both the ground-state transition between $N-1$ and N electrons (black line), as well as the transition to an N-electron excited state (gray line) fall within the bias window and can thus be used for transport (though not at the same time, due to Coulomb blockade). This results in a current that is different from the situation in (b). **(d)** The bias window is so large that the number of electrons can alternate between $N-1$, N and $N+1$, i.e. two electrons can tunnel onto the dot at the same time.

the energy required for adding the Nth electron to the dot:

$$\mu(N) \equiv U(N) - U(N-1) =$$
$$= (N - N_0 - \frac{1}{2})E_C - \frac{E_C}{|e|}(C_S V_{SD} + C_g V_g) + E_N \qquad (2.2)$$

where $E_C = e^2/C$ is the charging energy. This expression denotes the transition between the N-electron ground state and $N-1$-electron ground state. To avoid confusion when also excited states play a role, we will sometimes use a more explicit notation: the electrochemical potential for the transition between the $N-1$-electron state $|a\rangle$ and the N-electron state $|b\rangle$ is then denoted as $\mu_{a \leftrightarrow b}$, and is defined as $U_b - U_a$.

The electrochemical potential for the transitions between ground states with a different electron number N is shown in Fig. 2.2a. The discrete levels are spaced by the so-called addition energy:

$$E_{add}(N) = \mu(N+1) - \mu(N) = E_C + \Delta E. \qquad (2.3)$$

The addition energy consists of a purely electrostatic part, the charging energy E_C, plus the energy spacing between two discrete quantum levels, ΔE. Note

that ΔE can be zero, when two consecutive electrons are added to the same spin-degenerate level.

Of course, for transport to occur, energy conservation needs to be satisfied. This is the case when an electrochemical potential level falls within the 'bias window' between the electrochemical potential (Fermi energy) of the source (μ_S) and the drain (μ_D), i.e. $\mu_S \geq \mu \geq \mu_D$ with $-|e|V_{SD} = \mu_S - \mu_D$. Only then can an electron tunnel from the source onto the dot, and then tunnel off to the drain without losing or gaining energy. The important point to realize is that since the dot is very small, it has a very small capacitance and therefore a large charging energy – for typical dots $E_C \approx$ a few meV. If the electrochemical potential levels are as shown in Fig. 2.2a, this energy is not available (at low temperatures and small bias voltage). So, the number of electrons on the dot remains fixed and no current flows through the dot. This is known as Coulomb blockade.

The Coulomb blockade can be lifted by changing the voltage applied to the gate electrode. This changes the electrostatic potential of the dot with respect to that of the reservoirs, shifting the whole 'ladder' of electrochemical potential levels up or down. When a level falls within the bias window, the current through the device is switched on. In Fig. 2.2b $\mu(N)$ is aligned, so the electron number alternates between $N - 1$ and N. This means that the Nth electron can tunnel onto the dot from the source, but only after it tunnels off to the drain can another electron come onto the dot again from the source. This cycle is known as single-electron tunneling.

By sweeping the gate voltage and measuring the current, we obtain a trace
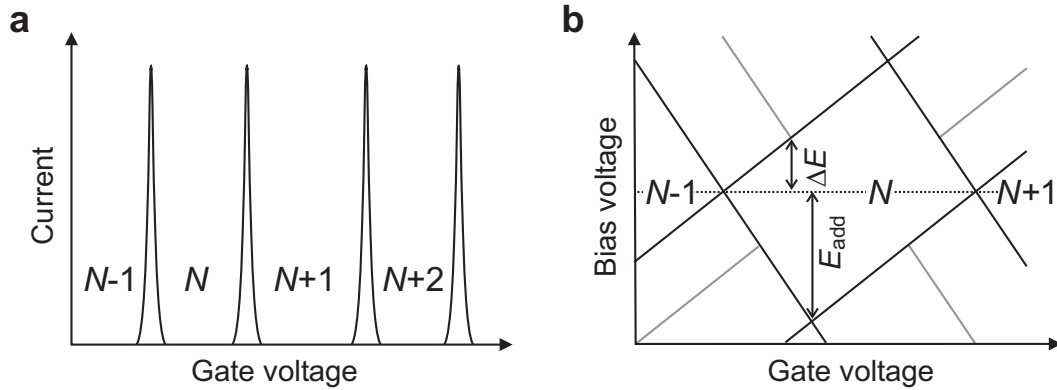
Figure 2.3: Transport through a quantum dot. **(a)** Coulomb peaks in current versus gate voltage in the linear-response regime. **(b)** Coulomb diamonds in differential conductance, dI/dV_{SD}, versus V_{SD} and V_g, up to large bias. The edges of the diamond-shaped regions (black) correspond to the onset of current. Diagonal lines emanating from the diamonds (gray) indicate the onset of transport through excited states.

as shown in Fig. 2.3a. At the positions of the peaks, an electrochemical potential level is aligned with the source and drain and a single-electron tunneling current flows. In the valleys between the peaks, the number of electrons on the dot is fixed due to Coulomb blockade. By tuning the gate voltage from one valley to the next one, the number of electrons on the dot can be precisely controlled. The distance between the peaks corresponds to $E_C + \Delta E$, and can therefore give information about the energy spectrum of the dot.

A second way to lift Coulomb blockade is by changing the source-drain voltage, V_{SD} (see Fig. 2.2c). (In general, we change the electrochemical potential of only one of the reservoirs, and keeping the other one fixed.) This increases the bias window and also 'drags' the electrochemical potential of the dot along, due to the capacitive coupling to the source. Again, a current can flow only when an electrochemical potential level falls within the bias window. When V_{SD} is increased so much that both the ground state as well as an excited state transition fall within the bias window, there are two paths available for electrons tunneling through the dot. In general, this will lead to a change in the current, enabling us to perform energy spectroscopy of the excited states. How exactly the current changes depends on the tunnel rates of the two paths [3].

Usually, we measure the current or differential conductance (the derivative of the current with respect to the source-drain bias) while sweeping the bias voltage, for a series of different values of the gate voltage. Such a measurement is shown schematically in Fig. 2.3b. Inside the diamond-shaped region, the number of electrons is fixed due to Coulomb blockade, and no current flows. Outside the diamonds, Coulomb blockade is lifted and single-electron tunneling can take place (or for larger bias voltages even double-electron tunneling is possible, see Fig. 2.2d). Excited states are revealed as changes in the current, i.e. as peaks or dips in the differential conductance. From such a 'Coulomb diamond' the energy of excited states as well as the charging energy can be read off directly.

The simple model described above explains successfully how quantization of charge and energy leads to effects like Coulomb blockade and Coulomb oscillations. Nevertheless, it is too simplified in many respects. For instance, the model considers only first-order tunneling processes, in which an electron tunnels first from one reservoir onto the dot, and then from the dot to the other reservoir. But when the tunnel rate between the dot and the leads, Γ, is increased, higher-order tunneling via virtual intermediate states becomes important. Such processes are known as 'cotunneling'. Furthermore, the simple model does not take into account the spin of the electrons, thereby excluding for instance exchange effects.

2.1.2   Spin configurations in few-electron quantum dots

The fact that electrons carry spin determines the electronic states of the quantum dot, in quite the same way as it does in real atoms. In fact, a group of physicists that pioneered measurements on few-electron (vertical) dots, have established a periodic system of elements in two dimensions [1]. In the simplest case – a dot containing just a single electron (artificial Hydrogen)– spin leads to a splitting of all orbitals into Zeeman doublets, with the ground state corresponding to the electron spin pointing up ($\uparrow$), i.e. parallel to the magnetic field, and the excited state to the spin pointing down ($\downarrow$), i.e. antiparallel to the magnetic field. The difference between the corresponding energy levels $E_\uparrow$ and $E_\downarrow$ is given by the Zeeman energy, $\Delta E_Z = g\mu_B B$, which is approximately 25 μeV/T in GaAs.

For two electrons in a quantum dot (artificial Helium), the situation is more complicated. For a Hamiltonian without spin-orbit coupling terms (which is true to a good approximation for our system), the two-electron state is the product of the orbital and spin state. Since electrons are fermions, the total two-electron state has to be anti-symmetric under exchange of the two particles. Therefore, if the orbital part is symmetric, the spin state must be anti-symmetric, and if the spin part is anti-symmetric, the orbital state must be symmetric. The anti-symmetric two-spin state is the spin singlet $|S\rangle$:

$$|S\rangle = \frac{|\uparrow\downarrow\rangle - |\downarrow\uparrow\rangle}{\sqrt{2}} \qquad (2.4)$$

which has total spin $S = 0$. The symmetric two-spin states are the so-called spin triplets ($|T_+\rangle$, $|T_0\rangle$ and $|T_-\rangle$):

$$|T_+\rangle = |\uparrow\uparrow\rangle \qquad |T_0\rangle = \frac{|\uparrow\downarrow\rangle + |\downarrow\uparrow\rangle}{\sqrt{2}} \qquad |T_-\rangle = |\downarrow\downarrow\rangle \qquad (2.5)$$

which have total spin $S = 1$ and a quantum number m_s (corresponding to the spin z-component) of 1, 0, and -1, respectively. In a finite magnetic field, the three triplet states are split by the Zeeman splitting, ΔE_Z.

Even at zero magnetic field, the energy of the two-electron system depends on its spin configuration, through the requirement of anti-symmetry of the total state. If we consider just the two lowest orbitals, ε_0 and ε_1, then there are six possibilities to fill these with two electrons (Fig. 2.4). At zero magnetic field [4], the two-electron ground state is always the spin singlet with both electrons on the lowest orbital (Fig. 2.4a), and the lowest excited states are then the three spin triplets (Fig. 2.4b–d). The energy gain of T_0 with respect to the excited spin singlet S_1 (Fig. 2.4e) is known as the exchange energy. It essentially results from the fact that electrons in the triplet states tend to avoid each other, reducing
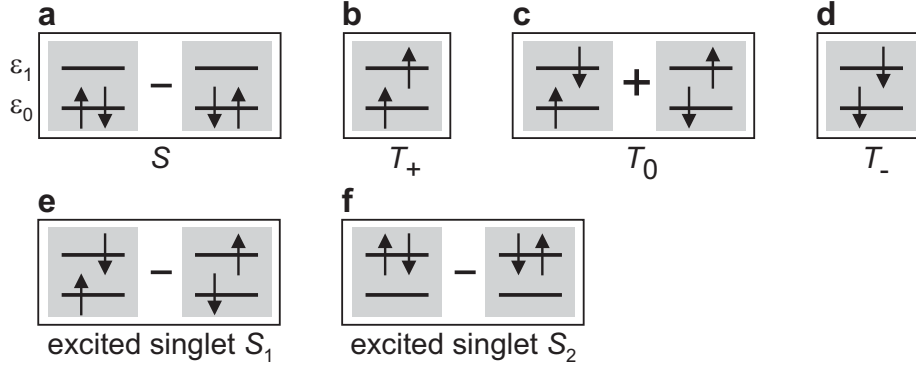
Figure 2.4: Schematic energy diagrams depicting the spin states of two electrons occupying two spin degenerate single-particle levels (ε_0 and ε_1). **(a)** Spin singlet, which is the ground state at zero magnetic field. **(b)**–**(d)** Lowest three spin triplet states, $|T_+\rangle$, $|T_0\rangle$ and $|T_-\rangle$, which have total spin $S = 1$ and quantum number $m_s = +1$, 0 and -1, respectively. In finite magnetic field, the triplet states are split by the Zeeman energy. **(e)** Excited spin singlet state, S_1. The energy difference between S_1 and the triplet state T_0 is the exchange energy. **(f)** Highest excited spin singlet state, S_2.

their mutual Coulomb energy. As the Coulomb interaction is very strong, the exchange energy can be quite large (a few 100 μeV) [5].

For more than two electrons, the spin states can be much more complicated. However, in some cases and for certain magnetic field regimes they might be well approximated by a one-electron Zeeman doublet (when N is odd) or by two-electron singlet or triplet states (when N is even). But there are still differences – for instance, if $N > 2$ the ground state at zero field can be a spin triplet, due to Hund's rule [6].

The eigenstates of a two-electron double dot (artificial Hydrogen molecule) are also spin singlets and triplets. We can again use the diagrams in Fig. 2.4, but now the single-particle eigenstates ε_0 and ε_1 represent the symmetric and anti-symmetric combination of the lowest orbital on each of the two dots, respectively. Due to tunneling between the dots, with tunneling matrix element t, ε_0 (the 'bonding state') and ε_1 (the 'anti-bonding state') are split by an energy $2t$. By filling the two states with two electrons, we again get a spin singlet ground state and a triplet first excited state (at zero field). However, the singlet ground state is not purely S (Fig. 2.4a), but also contains a small admixture of the excited singlet S_2 (Fig. 2.4f). The admixture of S_2 depends on the competition between inter-dot tunneling and the Coulomb repulsion, and serves to lower the Coulomb energy by reducing the double occupancy of the dots [7].

If we focus only on the singlet ground state and the triplet first excited states, then we can describe the two spins $\vec{S_1}$ and $\vec{S_2}$ by the Heisenberg Hamiltonian, $H =$

$J\vec{S_1}\cdot\vec{S_2}$. Due to this mapping procedure, J is now defined as the energy difference between the triplet state T_0 and the singlet ground state, which depends on the details of the double dot orbital states. From a Hund-Mulliken calculation [8], J is approximately given by $4t^2/U + V$, where U is the on-site charging energy and V includes the effect of the long-range Coulomb interaction. By changing the overlap of the wave functions of the two electrons, we can change t and therefore J. Thus, control of the inter-dot tunnel barrier would allow us to perform operations such as swapping or entangling two spins.

We finally remark on the orbital part of the electron wave function in the dot. The confinement potential of semiconductor quantum dots is to a good approximation a parabolic well. Indeed, experiments on vertical dots have shown excellent agreement between the orbital wave functions in the dots and the single-particle Fock-Darwin states [1]. The Fock-Darwin states can therefore be very helpful in explaining effects that arise from the spatial form of the electron wave function in the dot (e.g. the fact that different orbitals can have a very different tunnel coupling to the reservoir).

2.2   Device fabrication

Fabrication of lateral gated quantum dots starts with a semiconductor heterostructure, a sandwich of different layers of semiconducting material (see Fig. 2.5a). These layers, in our case GaAs and AlGaAs, are grown on top of each other using molecular beam epitaxy (MBE), resulting in very clean crystals. By doping the n-AlGaAs layer with Si, free electrons are introduced. These accumulate at the interface between GaAs and AlGaAs, typically 100 nm below the surface, forming a two-dimensional electron gas (2DEG) – a thin ($\sim$10 nm) sheet of electrons that can only move along the interface. The 2DEG can have a high mobility and relatively low electron density (typically $10^5 - 10^6$ cm^2/Vs and $\sim 3 \times 10^{15}$ m^{-2}, respectively). The low electron density results in a large Fermi wavelength ($\sim$ 40 nm) and a large screening length, which allows us to locally deplete the 2DEG with an electric field. This electric field is created by applying (negative) voltages to metal gate electrodes on top of the heterostructure (Fig. 2.5b).

We fabricate these electrodes using electron-beam lithography. First, we spin a layer of organic resists (typically poly-methyl-methacrylate, PMMA) on the heterostructure surface (Fig. 2.6a). Then the gate pattern is defined by writing with a focused electron beam in the electron-sensitive resist. This locally breaks up the polymer chains, so that the exposed parts can be removed by a developer (solution of methyl isobutyl ketone, MIBK, and iso-propyl alcohol, IPA), see
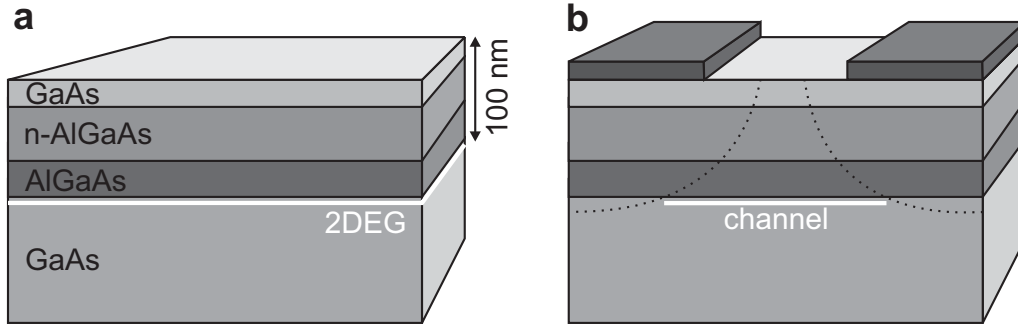
Figure 2.5: Confining electrons in a semiconductor. **(a)** Semiconductor heterostructure containing a 2DEG (indicated in white) approximately 100 nm below the surface, at the interface between GaAs and AlGaAs. The electrons in the 2DEG result from Si donors in the n-AlGaAs layer. (The thickness of the different layers is not to scale.) **(b)** By applying negative voltages to the metal electrodes on the surface of the heterostructure, the underlying 2DEG can be locally depleted. In this way, electrons can be confined to one or even zero dimensions.

Fig. 2.6b. Note that there is some undercut of the PMMA layer. This undercut is caused by the significant electron scattering at the interface between GaAs and PMMA during the electron beam exposure.

In the next step (Fig. 2.6c), metal is evaporated, which only makes contact to the heterostructure at the places where the resist has been exposed and removed. In our devices, the metal gates consist of a thin (5 nm) 'sticking' layer of titanium, with a 30 nm layer of gold on top. The last step is the removal of the remaining resist by acetone (Fig. 2.6d). In this process, the metal on top of the resist is removed as well, the so-called 'lift-off'. The lift-off process is facilitated by the undercut in the resist layer. Now metal electrodes are left at the places that were
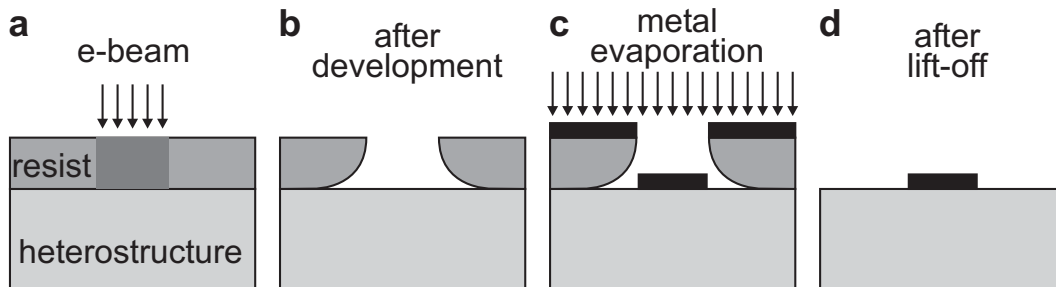
Figure 2.6: Fabrication of metal electrodes on the surface of the heterostructure. **(a)** Writing a pattern in the resist layer with an electron beam. **(b)** After developing, the resist has been locally removed. **(c)** Evaporating metal. **(d)** After lift-off, a metal electrode remains.

a

b
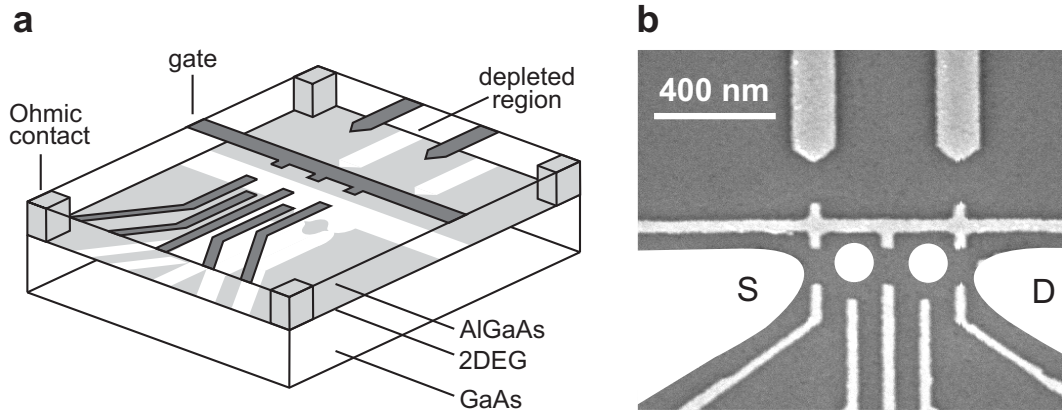
Figure 2.7: Lateral quantum dot device defined by metal surface electrodes. **(a)** Schematic view of a device. Negative voltages applied to metal gate electrodes (dark gray) lead to depleted regions (white) in the 2DEG (light gray). Ohmic contacts (light gray columns) enable bonding wires (not shown) to make electrical contact to the 2DEG reservoirs. **(b)** Scanning electron microscope image of an actual device, showing the gate electrodes (light gray) on top of the surface (dark gray). The two white dots indicate two quantum dots, connected via tunable tunnel barriers to a source (S) and drain (D) reservoir, indicated in white. The two upper gates can be used to create two quantum point contacts, in order to detect changes in the number of electrons on the dot, as will be explained in chapter 3 (Device fabricated by Laurens Willems van Beveren and Ronald Hanson at NTT Basic Research Labs.)

exposed to the electron beam. The electron beam can accurately write with a resolution of about 5 nm, but in practice the minimal width of a gate electrode is about 40 nm, limited by the development and the lift-off step.

Electron-beam lithography allows very complicated gate structures to be made (Fig. 2.7). By applying negative voltages to the gates, the 2DEG is locally depleted, creating one or more small islands that are isolated from the large 2DEG reservoirs. These islands are the quantum dots. In order to probe them, we need to make electrical contact to the reservoirs. For this, we evaporate AuGeNi on the contact pads and anneal at ~ 400 degrees Celsius for 60 seconds. This forms ohmic contacts with a resistance of about 1 kOhm that connect the 2DEG source and drain reservoirs electrically to metal bonding pads on the surface. Metal wires bonded to these pads run toward the current or voltage probes, enabling us to perform transport measurements.

2.3   Measurement setup

Dilution refrigerator

To resolve small energies such as the Zeeman splitting, the sample has to be cooled down to temperatures well below a Kelvin. We use an Oxford Kelvinox 300 dilution refrigerator, which has a base temperature of about 10 mK, and a cooling power in excess of 300 μW (at 100 mK). The sample holder is connected to a cold finger and placed in a copper can (36 mm inner diameter) in the bore of a superconducting magnet that can apply a magnetic field up to 16 T.

Measurement electronics

A typical measurement involves applying a source-drain voltage over (a part of) the device, and measuring the resulting current as a function of the voltages applied to the gates. The electrical circuits for the voltage-biased current measurement and for applying the gate voltages are shown in Fig. 2.8 and Fig. 2.9, respectively. The most important parts of the measurement electronics – i.e. the current-to-voltage (*I-V*) converter, isolation amplifier, voltage source and digital-to-analog convertors (DACs) – were all built by Raymond Schouten at Delft University. The underlying principle of the setup is to isolate the sample electrically from the measurement electronics. This is achieved via optical isolation at both sides of the measurement chain, i.e. in the voltage source, the isolation amplifier, as well as the DACs. In all these units, the electrical signal passes through analog optocouplers, which first convert it to an optical signal using an LED, and then convert the optical signal back using a photodiode. In this way, there is no galvanic connection between the two sides. In addition, all circuitry at the sample side is analog (even the DACs have no clock circuits or microprocessors), battery-powered, and uses a single clean ground (connected to the metal parts of the fridge) which is separated from the ground used by the 'dirty' electronics. All these features help to eliminate ground loops and reduce interference on the measurement signal.

Measurements are controlled by a computer running LabView. It sends commands via a fiber link to two DAC-boxes, each containing 8 digital-to-analog convertors, and powered by a specially shielded transformer. Most of the DACs are used to generate the voltages applied to the gate electrodes (typically between 0 and -5 V). One of the DACs controls the source-drain voltage for the device. The output voltage of this DAC (typically between +5 and -5V) is sent to a voltage source, which attenuates the signal by a factor 10, 10^2, 10^3 or 10^4 and provides optical isolation. The attenuated voltage is then applied to one of the ohmic contacts connected to the source reservoir of the device.
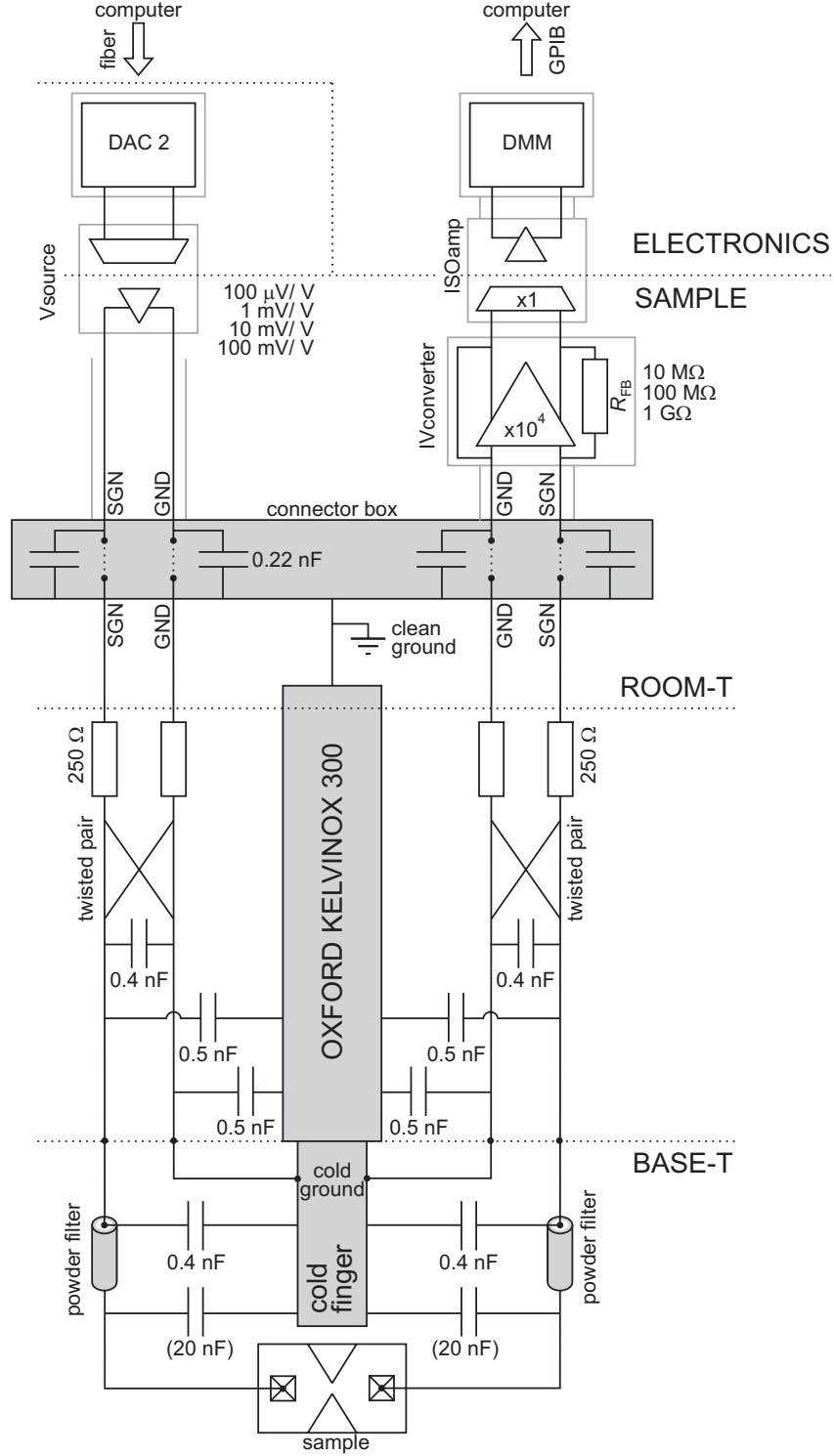
Figure 2.8: Electrical circuit for performing a voltage-biased current measurement. Elements shown in gray are connected to ground. Gray lines indicate the shielding of the measurement electronics and wires.
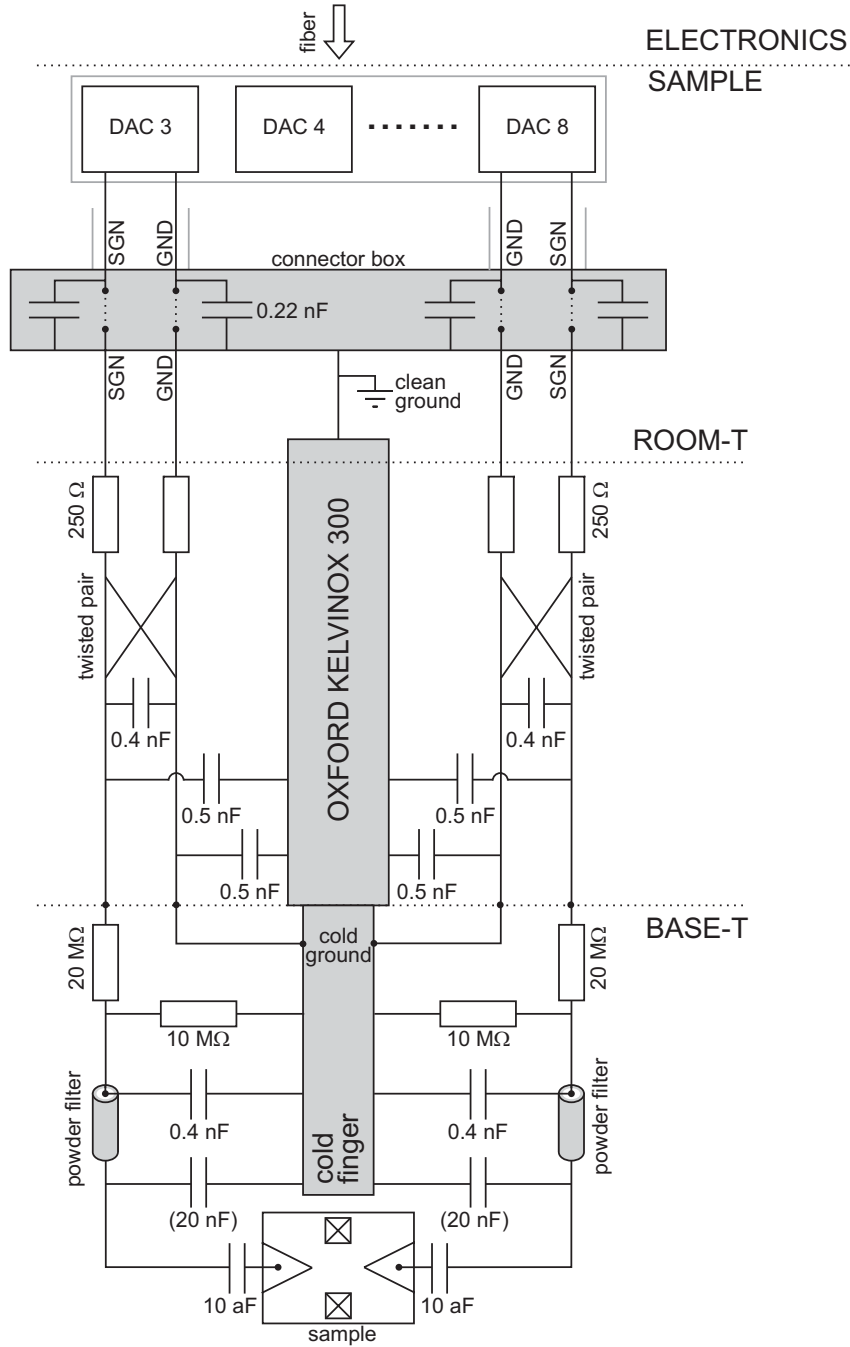
Figure 2.9: Electrical circuit for applying voltages to the gate electrodes. Elements shown in gray are connected to ground. Gray lines indicate the shielding of the measurement electronics and wires.

The resulting current coming from the drain reservoir is fed to a low-noise *I-V* converter. In this thesis we use two types, depending on the desired bandwidth. The first one (used in chapters 3, 4 and 5), is designed for low-frequency measurements. It has a bandwidth of about 1 kHz, and a noise floor of ~ 5 fA/Hz$^{1/2}$. The feedback resistance can be set to 10 MΩ, 100 MΩ or 1GΩ, with an input resistance that is a factor 10^3 or 10^4 smaller (for the 'low noise' or 'low input resistance' setting, respectively). The faster *I-V* converter, used in chapters 3 (section 3.7), 6, 7 and 8 has a bandwidth of about 150 kHz, and a current noise of ~ 1 pA/Hz$^{1/2}$ at 100 kHz. The feedback resistance is 10 MΩ, corresponding to an input resistance of 1.3 kΩ.

The signal from the *I-V* converter is then sent to an isolation amplifier, to provide optical isolation and possibly gain. Again we can choose a low-frequency version (up to ~ 1 kHz) or a high-frequency one (up to ~ 300 kHz). The voltage from the isolation amplifier is finally measured by a digital multimeter (Keithley 2700) and sent to the computer via GPIB interface. Alternatively, we can use a lock-in amplifier (Stanford EG&G 5210) if the signal to be measured is periodic, or an ADwin Gold module for very fast measurements (up to 2.2×10^6 14-bit samples per second).

Measurement wires

To make contact to the sample, 2×12 twisted pairs of wires run from two connector boxes at room temperature all the way down to the 'cold finger' at base temperature. The diameter and material of these wires is chosen to minimize the heat load on the mixing chamber. From room temperature to 1 Kelvin, 2×9 pairs consist of manganine wires (100 μm diameter), and 2×3 pairs of copper wires (90 μm diameter). From 1 Kelvin to the mixing chamber, superconducting 'Niomax' wires (50 μm diameter) are used. From the mixing chamber to the bottom of the cold finger, where thermal conductivity is no longer a constraint, we have standard copper wires. At base temperature, one wire of each twisted pair is connected to 'cold ground' (i.e. the cold finger), which is electrically connected to clean ground via the metal parts of the fridge.

All wires are thermally anchored to the fridge, by carefully wrapping them around copper posts, at several temperature stages (4 K, 1 K, ~ 100 mK and ~ 10 mK). At room temperature, the resistance of the wires is about 250 Ω or 150 Ω for the manganine or copper wires, respectively. At low temperature it is about 50 Ω. The wires have various parasitic capacitances to their twisted partner and to ground, as indicated in Fig. 2.8 and Fig. 2.9.

Filtering

The wires connect the device to the measurement electronics at room temperature, so they have to be carefully filtered to avoid that the electrons in the sample heat up due to spurious noise and interference. Several filtering stages are required for different frequency ranges (see Fig. 2.8 and Fig. 2.9). In the connector box at room temperature, all wires are connected to ground via 0.22 nF 'feedthrough capacitors'. At base temperature, all signal wires run through 'copper powder filters' [9]. These are copper tubes filled with copper powder, in which 4 signal wires with a length of about 2 meters each are wound. The powder absorbs the high-frequency noise very effectively, leading to an attenuation of more than -60 dB from a few 100 MHz up to more than 50 GHz [10].

To remove the remaining low-frequency noise, we solder a 20 nF capacitor between each signal wire and the cold finger ground. In combination with the $\sim 100 \ \Omega$ resistance of the wires, this forms a low-pass RC filter with a cut-off frequency of about 100 kHz (even 10 kHz for the wire connected to the *I-V* converter, due to its input resistance of about 1.3 kΩ). These filters are used for the wires connecting to ohmic contacts (although they were taken out to perform some of the high-bandwidth measurements described in this thesis). For the wires connecting to gate electrodes, a 1:3 voltage divider is present (consisting of a 20 MΩ resistance in the signal line and a 10 MΩ resistance to ground). In this way, the gate voltages are filtered by a low-pass RC filter with a cut-off frequency of about 1 Hz. By combining all these filters, the electrons in the sample can be cooled to an effective temperature below 100 mK (if no extra heat loads such as coaxial cables are present).

High-frequency signals

High-frequency signals can be applied to gate electrodes via two coaxial cables. They consist of three parts, connected via standard 2.4 mm Hewlett Packard connectors (specified up to 50 GHz). From room temperature to 1 Kelvin, a 0.085 inch semi-rigid Be-Cu (inner and outer conductor) coaxial cable is used. From 1 Kelvin to the mixing chamber, we use 0.085 inch semi-rigid superconducting Nb. From the mixing chamber to the sample holder, flexible tin plated Cu coaxial cables are present. The coaxes are thermally anchored at 4 K, 1 K, ~ 800 mK, ~ 100 mK and base temperature, by clamping each cable firmly between two copper parts. To thermalize also the inner conductor of the coax, we use Hewlett Packard 8490D attenuators (typically -20 dB) at 1 K. These attenuators cannot be used at the mixing chamber, as they tend to become superconducting below about 100 mK. We have also tried using Inmet 50EH attenuators at the mixing chamber, but these showed the same problem.

To generate the high-frequency signals, we use a microwave source (Hewlett Packard 83650A) that goes up to 50 GHz; a pulse generator (Hewlett Packard 8133A), which generates simple 10 ns to 1 μs pulses with a rise time of 60 ps; and an arbitrary waveform generator (Sony Tektronix AWS520), which can generate more complicated pulses with a rise time of about 1 ns. With the cables described above, the fastest pulse flank we can transmit to the sample is about 200 ps. Microwave signals are transmitted with about 10 dB loss at 30 GHz.

Special care needs to be given to the connection from the coaxial cable to the chip, in order to minimize reflections. The sample holder we use, has an SMA connector that can be connected to the 2.4 mm coaxial cable. At the other end, the pin of the SMA connector sticks through a small hole in the chip carrier. This allows it to be soldered to a metal pad on the chip carrier, from which we can then bond to the chip. This sample holder is used to apply pulses or microwave signals to a gate electrode.

2.4   Device stability

A severe experimental difficulty that is not related to the measurement setup, but to the device itself, is the problem of 'charge switching'. It shows up in measurements as fluctuations in the position of a Coulomb peak, or as sudden jumps in the QPC-current that are not related to charging or discharging of a nearby quantum dot. Generally, these switching events are attributed to (deep) traps in the donor layer that capture or release an electron close to the quantum dot [11]. This well-known but poorly understood phenomenon causes fluctuations in the electrostatic potential landscape in the 2DEG.

The strength of the fluctuations can differ enormously. In some samples, switching occurs on a time scale of seconds, making only the most trivial measurements possible, whereas in other samples no major switching is visible on a time scale of hours. It is not clear what exactly determines the stability. It certainly depends on the heterostructure, as some wafers are clearly better than others. A number of growth parameters could be important, such as the Al concentration in the AlGaAs, the doping density and method, the thickness of the spacer layer between the n-AlGaAs and GaAs, the depth of the 2DEG below the surface, and many more. Recently, we have started a collaboration with the group of Professor Wegscheider in Regensburg to grow and characterize heterostructures in which some of these parameters are systematically varied, hoping to gain insight in the factors that determine device stability.

Even for the same heterostructure, some devices show less charge switching
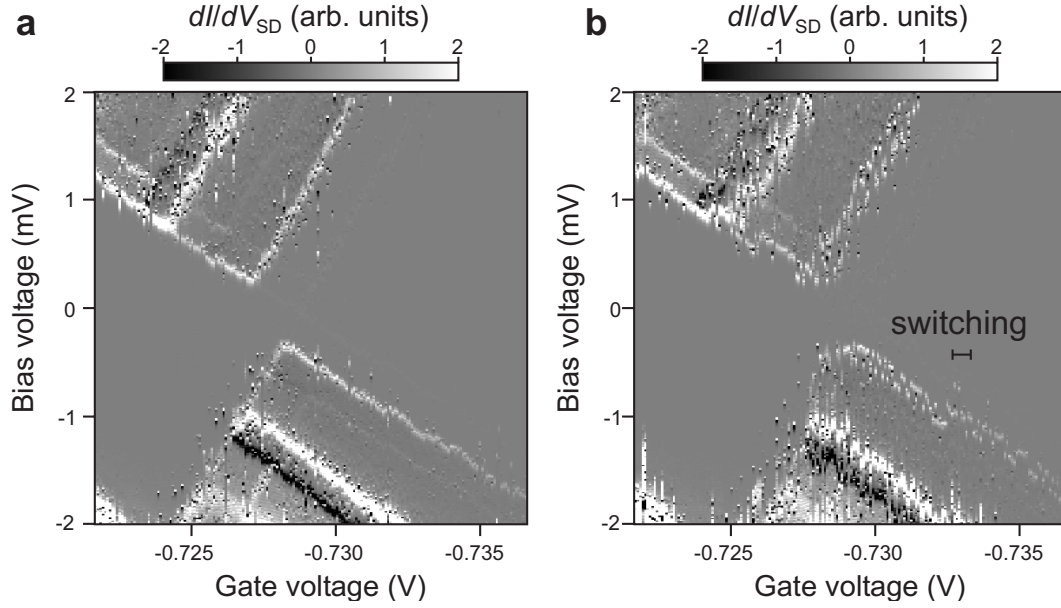
Figure 2.10: Charge switching in a large-bias measurement in the few-electron regime, for $B = 12$ T. **(a)** Differential conductance, dI/dV_{SD} (in grayscale), as a function of bias voltage and gate voltage. This measurement is considered reasonably stable. **(b)** Identical measurement, taken immediately after (a). A single two-level fluctuator has become active, causing the effective gate voltage to fluctuate between two values at any position in the figure, and leading to an apparent splitting of all the lines. This is considered a measurement of poor stability.

than others. The reasons for this are not clear. There are reports that stability is improved if the sample is cooled down slowly, while applying a positive voltage on all gates that are going to be used in the experiment. This procedure effectively 'freezes in' a negative charge around the gates, such that less negative gate voltages are sufficient to define the quantum dot at low temperatures. Most samples described in this thesis have been cooled down from room temperature to 4 K slowly (in one to two days) with all gates grounded. Others have been cooled down faster, or with +280 mV on the gates. No clear trend as a function of these parameters was observed.

As long as we can not suppress the charge fluctuations, finding a stable device will involve an element of luck: Fig. 2.10 shows two Coulomb diamonds that were measured during one night, immediately after each other, under identical conditions. The measurement in Fig. 2.10a shows reasonably stable behavior, but in Fig. 2.10b the effects of an individual two-level fluctuator are visible. This particular fluctuator remained active for a week, until the sample was warmed up.

Switching has made all experiments we performed more difficult, and has made some experiments that we wanted to perform impossible. Better control over heterostructure stability might become essential for the increasingly difficult steps towards creating quantum dot spin qubits.

References

[1] L.P. Kouwenhoven, D.G. Austing, and S. Tarucha, Rep. Prog. Phys. **64** (6), 701 (2001).

[2] L.P. Kouwenhoven, C.M. Marcus, P.L. McEuen, S. Tarucha, R.M. Westervelt, and N.S. Wingreen, in *Mesoscopic Electron Transport*, edited by L.L. Sohn, L.P. Kouwenhoven and G. Schön, (Kluwer, Series E **345**, 1997), p.105-214.

[3] See e.g. R. Hanson, I. T. Vink, D. P. DiVincenzo, L. M. K. Vandersypen, J. M. Elzerman, L. H. Willems van Beveren, and L.P. Kouwenhoven, to be published in the Proceedings of the XXXIXth Rencontres de Moriond (La Thuile, 2004) "Quantum information and decoherence in nanosystems"; cond-mat/0407793.

[4] N.W. Ashcroft and N.D. Mermin, *Solid state physics* (Brooks/Cole 1976).

[5] S. Tarucha, D.G. Austing, Y. Tokura, W.G. van der Wiel and L.P. Kouwenhoven, Phys. Rev. Lett. **84**, 2485 (2000).

[6] S. Tarucha, D.G. Austing, T. Honda, R.J. van der Hage and L.P. Kouwenhoven, Phys. Rev. Lett. **77**, 3613 (1996) .

[7] V.N. Golovach and D. Loss, Europhys. Lett. **62**, 83 (2003).

[8] G. Burkard, D. Loss, and D. P. DiVincenzo, Phys. Rev. B **59**, 2070 (1999).

[9] J.M. Martinis, M.H. Devoret and J. Clarke, Phys. Rev. B **35**, 4682 (1987).

[10] K. Bladh *et al.*, Rev. Sci. Instr. **74**,1323 (2003).

[11] J.H. Davies, *The physics of low-dimensional semiconductors* (Cambridge University Press, 1998).

Chapter 3

Few-electron quantum dot circuit with integrated charge read-out

R. Hanson, J. M. Elzerman, L. M. K. Vandersypen,
L. H. Willems van Beveren, J. S. Greidanus, R. N. Schouten,
S. De Franceschi, S. Tarucha and L. P. Kouwenhoven

In this chapter, we report measurements on a fully tunable double quantum dot circuit, integrated with two quantum point contacts that serve as charge detectors. The circuit is defined in a two-dimensional electron gas by means of surface gates on top of a GaAs/AlGaAs heterostructure. Full control over the electron number (down to zero), the dot-lead coupling and the inter-dot tunnel coupling is experimentally demonstrated. In addition, we use microwave radiation to pump an electron from one dot to the other by absorption of a single photon. Finally, using charge detection we observe single-electron tunneling in and out of a single dot in real-time. These experiments demonstrate that this quantum dot circuit can serve as a good starting point for a scalable spin-qubit system.

3.1   Gate design of few-electron quantum dots

The proposal by Loss and DiVincenzo [1] to use single electron spins in quantum dots as quantum bits, describes an optimal combination of the single-electron charge degree of freedom (for convenient manipulation using electrical voltages) and the spin degree of freedom (which is believed to have a long coherence time, essential for encoding quantum information). For the control of one-electron quantum states by electrical voltages, the first requirement is to realize an appropriate quantum dot circuit containing just a single conduction electron.

Single-electron quantum dots have been created in self-assembled structures [2] and in small vertical pillars defined by etching [3]. Recently, realization of few-electron dots in semiconductor nanowires [4] and carbon nanotubes [5] has also been reported. The disadvantage of these types of quantum dots is that they are hard to integrate into circuits with a controllable coupling between the elements, although integration of vertical quantum dot structures is currently being pursued [6, 7]. Alternatively, we can use a system of lateral quantum dots defined in a two-dimensional electron gas (2DEG) by surface gates on top of a semiconductor heterostructure [8]. Here, integration of multiple dots is straightforward, by simply increasing the number of gate electrodes. In addition, the tunnel coupling between the dots can be tuned *in situ*, since it is controlled by the gate voltages. The challenge is to reduce the number of electrons to one per quantum dot. This has long been impossible, since reducing the electron number tends to be accompanied by a decrease in the tunnel coupling, resulting in a current too small to be measured. However, by proper design of the surface gate geometry the decrease of the tunnel coupling can be compensated for.

In 2000, Ciorga *et al.* reported measurements on the first lateral few-electron quantum dot [9]. Their device made use of two types of gates specifically designed to have different functionalities [10]. The gates of one type were big and largely enclosed the quantum dot. The voltages on these gates determine the dot potential. The other type of gate was thin and just reached up to the barrier region. The voltage on this gate has a very small effect on the dot potential, and it can be used almost independently to set the tunnel barrier. The combination of the two gate types allows the dot potential (and thereby electron number) to be changed over a wide range while keeping the tunnel rates high enough for measuring electron transport through the dot.

Since 2001, we have fabricated and measured several few-electron single and double quantum dots, of four different designs A-D, shown in Fig. 3.1a-d. These designs share the different gate functionalities explained above. The first two types, A and B (Fig. 3.1a-b), have only been used once as few-electron *single* dots.
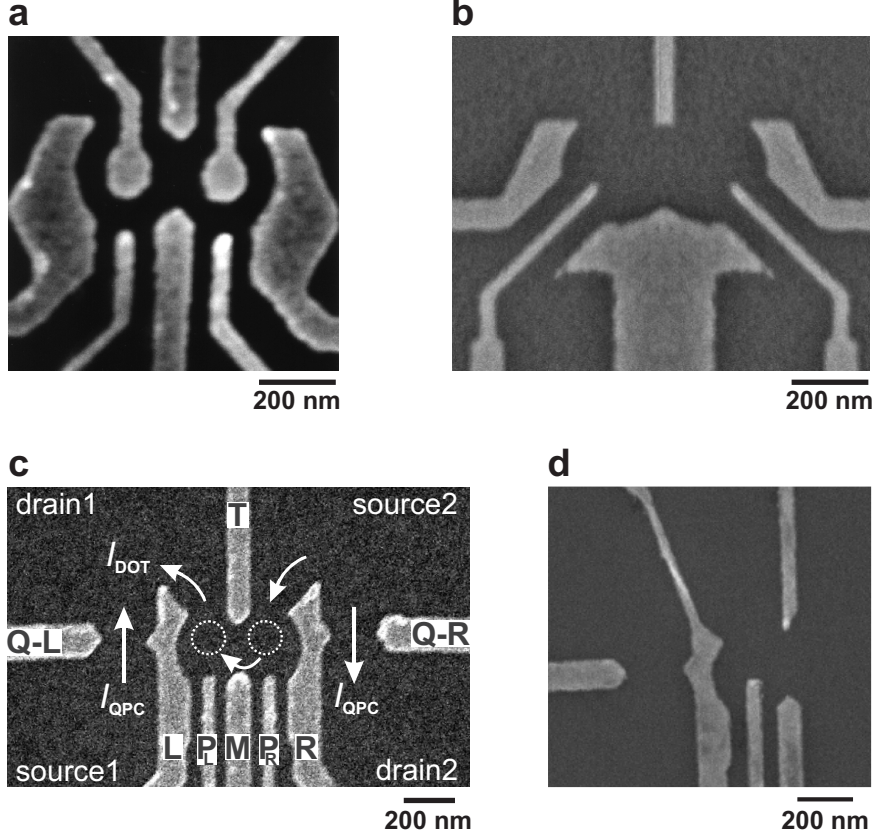
Figure 3.1: Scanning electron microscope images of few-electron quantum dot devices measured in Delft, showing the metal gate electrodes (light) on top of a GaAs/AlGaAs heterostructure (dark). **(a)** Design A. This device was used only as a few-electron *single* dot. Due to the similarity of the image to characters from the Japanese 'Gundam' animation, this has become known as the Gundam design. (The device was fabricated by Wilfred van der Wiel at NTT Basic Research Laboratories.) **(b)** Design B. This design was used only once as a few-electron *single* dot. (This device was fabricated by Wilfred van der Wiel and Ronald Hanson at NTT Basic Research Laboratories.) **(c)** Design C, with two extra side gates to form two quantum point contacts (QPCs). Devices having this design were operated many times as a single dot, and twice as a few-electron *double* dot. White dotted circles indicate the two quantum dots, white arrows show the possible current paths. A bias voltage, V_{DOT}, can be applied between source 2 and drain 1, leading to current through the dot(s), I_{DOT}. A bias voltage, V_{SD1} (V_{SD2}), between source 1 (source 2) and drain 1 (drain 2), yields a current, I_{QPC}, through the left (right) QPC. (This device was fabricated by Ronald Hanson and Laurens Willems van Beveren at NTT Basic Research Laboratories.) **(d)** Design D. In this design the lead for the QPC is separated from the dot lead by extending one of the gates. Devices of this type were operated many times as a single dot. (This device was fabricated by Wouter Naber and Laurens Willems van Beveren in DIMES in Delft.)

In both cases, one of the gate electrodes was not functioning, which prevented us from testing if these devices also function as few-electron *double* dots. In design A (Fig. 3.1a), two gates coming from the top end in small circles (the 'eyes'). These gates were meant to make the dot confinement potential steeper, by applying a positive voltage to them (up to ∼ 0.5 V). The gates were not effective, and were left out in later designs.

To verify that the device of design A can be operated as a few-electron single quantum dot, we performed a large-bias measurement of the differential conductance through the dot. Going towards more negative gate voltage, a series of 'Coulomb diamonds' is revealed (Fig. 3.2a), in which the number of electrons on the dot, N, is constant. This is followed by a region in which the 'diamond' does not close, even up to a source-drain voltage of 10 mV, i.e. several times larger than the typical charging energy for a small dot (∼ 2 meV). Therefore, in this region $N = 0$.
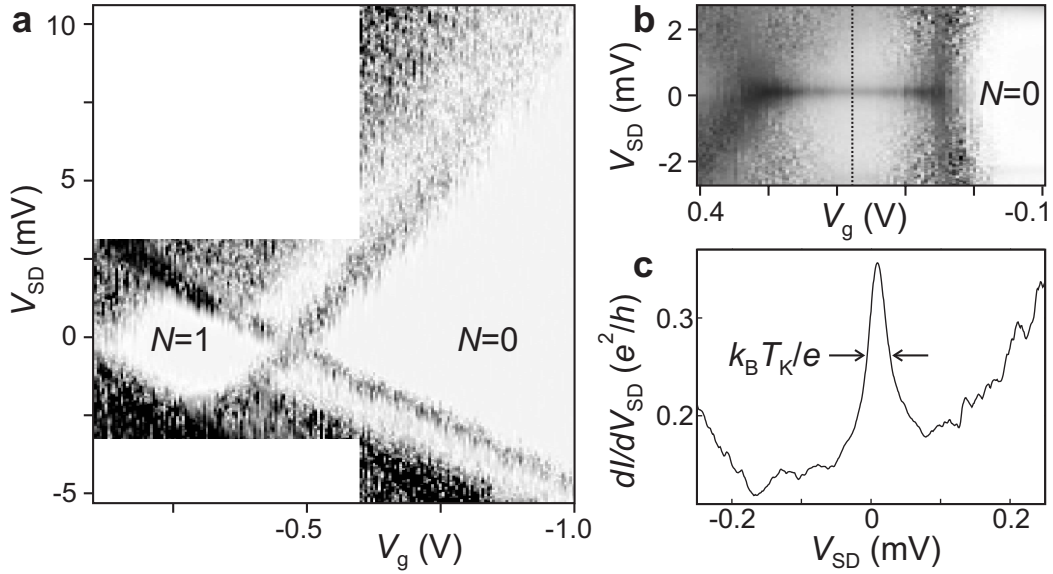
Figure 3.2: Kondo effect in a one-electron lateral quantum dot of the type shown in Fig. 3.1a. **(a)** Differential conductance (in grayscale) versus source-drain voltage, V_{SD}, and plunger gate voltage, V_g. In the white diamond and the white region to the right (indicated by $N = 1$ and $N = 0$, respectively), no current flows due to Coulomb blockade. The $N = 0$ region opens up to more than 10 mV, indicating that the dot is really empty here. **(b)** Close-up of the $N = 1$ diamond for stronger coupling to the reservoirs. A sharp Kondo resonance is visible at zero source-drain voltage. Although charge switching is severe in this sample, the position of the Kondo resonance is very stable, as it is pinned to the Fermi energy of the reservoirs. **(c)** Kondo zero-bias peak in differential conductance, taken at the position indicated by the dotted line in (b).

The tunnel coupling between the dot and the source and drain reservoirs could be changed by simply readjusting the gate voltages. For strong coupling, a zero-bias peak – hallmark of the Kondo effect [11] – became visible throughout the one-electron diamond (Fig. 3.2b). From the width of the zero-bias peak (Fig. 3.2c) we found a Kondo temperature of about 0.4 K. The appearance of a one-electron Kondo effect (unpublished) implies that this quantum dot design allows the tunnel coupling to be tuned over a wide range, even in the few-electron regime. In addition, it is striking evidence that we can confine a single *spin* in a lateral quantum dot.

In the second quantum dot design (Fig. 3.1b), the narrow 'plunger' gates approach the dot more from the sides, rather than from below, making the dots more symmetric. In this way, they are further away from the central tunnel barrier, reducing the effect they have on the tunnel rate. Also, the gate coming from the top of the picture was made thinner, in order to make the tunnel barriers more easily controllable [9]. This device was easily tunable.

In design C (Fig. 3.1c) quantum point contacts (QPCs) were added to serve as charge detectors. The QPCs were placed close to the dots, thus ensuring a good charge sensitivity. To create space for the QPCs, the plunger gates were again set as in the first design. Two devices with this gate design have functioned as a few-electron double dot, and several others as few-electron single dots.

In design C, the QPC and the dot share one lead, which makes it inconvenient to perform transport measurements through the dot and at the same time measure the current through the QPC. To solve this problem, we have created separate leads for the dot and the QPC in design D (Fig. 3.1d) by extending the side gate all the way to the edge of the 2DEG mesa. Also, the plunger gates were extended to increase the capacitive coupling to electrons in the dot.

3.2   Device characterization

In the rest of this chapter, we experimentally study devices of design C (see Fig. 3.1c). They are created in a GaAs/AlGaAs heterostructure (grown by T. Saku at NTT Basic Research Laboratories), with a 2DEG 90nm below the surface (electron density $2.9 \cdot 10^{15}$ m^{-2}). The double dot is defined by applying negative voltages to the 6 central gates. Gate T in combination with the left (right) gate, L (R), controls the tunnel barrier from the left (right) dot to drain 1 (source 2). Gate T in combination with the middle gate, M, controls the tunnel barrier between the two dots. The narrow 'plunger' gates, P_L and P_R, are used to change the electrostatic potential of the left and right dot, respectively. The left plunger

gate is connected to a coaxial cable, so that we can apply high-frequency signals. In the present experiments we do not apply dc voltages to P_L. In order to control the number of electrons on the double dot, we use gate L for the left dot and P_R or R for the right dot. All measurements are performed with the sample cooled to a base temperature of about 10 mK inside a dilution refrigerator.

We first characterize the individual dots using standard Coulomb blockade experiments [8], i.e. by measuring I_{DOT}. We find that the energy cost for adding a second electron to a one-electron dot is 3.7 meV. The one-electron excitation energy (i.e. the difference between the ground state and the first orbital excited state) is 1.8 meV at zero magnetic field. For a two-electron dot the energy difference between the spin singlet ground state and the spin triplet excited state is 1.0 meV at zero magnetic field. Increasing the field (perpendicular to the 2DEG) leads to a transition from a singlet to a triplet ground state [3] at about 1.7 Tesla, as can be seen from the large-bias measurement in Fig. 3.3a. From this measurement, we can extract the energy difference between the singlet and triplet states, E_{ST}, as a function of the magnetic field (plotted in Fig.3.3b).
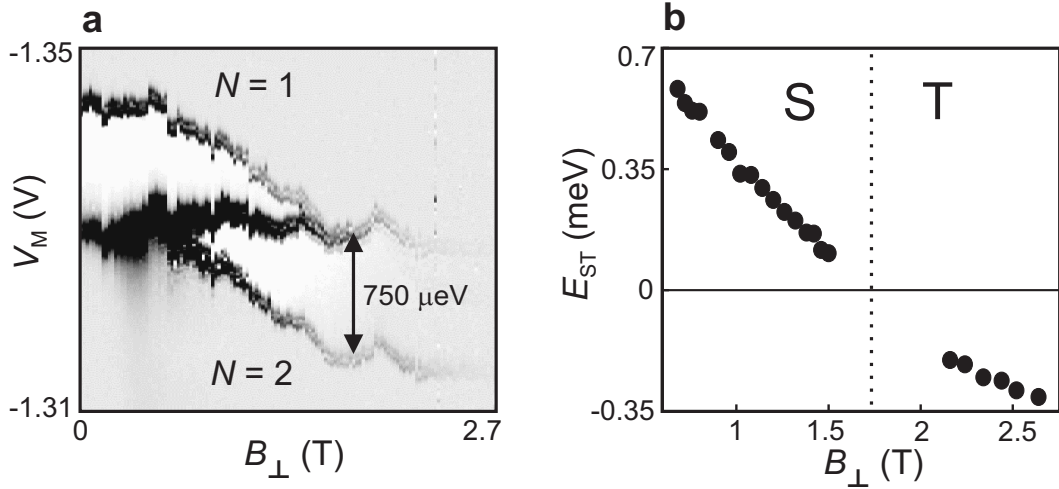
Figure 3.3: Single-triplet ground state transition in a two-electron quantum dot. **(a)** Differential conductance dI_{DOT}/dV_{SD} versus gate voltage, V_M, and perpendicular magnetic field, $B_\perp$. Dark (light) corresponds to high (low) value for dI_{DOT}/dV_{SD}. Within the stripe of finite conductance, set by the source-drain bias voltage of 750 μeV, the evolution of the energy difference between the singlet state (ground state at zero field) and the triplet state is visible [8]. At around 1.7 T the singlet and triplet states cross and the ground state becomes a spin triplet. **(b)** Energy difference between the singlet and the triplet states, E_{ST}, as a function of $B_\perp$, extracted from (a). The ground state is indicated by S (for singlet) and T (for triplet). Near the ground state transition, overlapping peaks prevent a reliable estimate for E_{ST}.

3.3 Quantum Point Contact as charge detector

As an alternative to measuring the current through the quantum dot, we can also measure the charge on the dot using one of the QPCs [12, 13]. To demonstrate this functionality, we first define only the left dot (by grounding gates R and P_R), and use the left QPC as a charge detector. The QPC is formed by applying negative voltages to $Q - L$ and L. This creates a narrow constriction in the 2DEG, with a conductance, G, that is quantized when sweeping the gate voltage V_{Q-L}. The last plateau (at $G = 2e^2/h$) and the transition to complete pinch-off (i.e. $G = 0$) are shown in Fig. 3.4a. We tune the QPC to the steepest point ($G \approx e^2/h$), where the QPC-conductance has a maximum sensitivity to changes in the electrostatic environment, including changes in the charge of the nearby quantum dot.

To change the number of electrons in the left dot, we make gate voltage V_M more negative (see Fig. 3.4b). This reduces the QPC current, due to the capacitive coupling from gate M to the QPC constriction. In addition, the changing gate voltage periodically pushes an electron out of the dot. The associated sudden change in charge lifts the electrostatic potential at the QPC constriction, resulting in a step-like feature in I_{QPC} (see the expansion in Fig. 3.4b, where the linear background is subtracted). This step indicates a change in the electron number. So, even without passing current through the dot, I_{QPC} provides information about the charge on the dot.

To enhance the charge sensitivity we apply a small modulation (0.3 mV at 17.7 Hz) to V_M and use lock-in detection to measure dI_{QPC}/dV_M [13]. The steps in I_{QPC} now appear as dips in dI_{QPC}/dV_M. Figure 3.4c shows the resulting dips, as well as the corresponding Coulomb peaks measured in the current through the dot. The coincidence of the Coulomb peaks and dips demonstrates that the QPC indeed functions as a charge detector. The height of the current step induced by a change in electron occupation, $\Delta I_{QPC,e}$, is ~ 50 pA in Fig. 3.4b. We typically find $\Delta I_{QPC,e}$ to be 1-2% of the total current. The unique advantage of QPC charge detection is that it provides a signal even when the tunnel barriers of the dot are so opaque that I_{DOT} is too small to be measured [12, 13]. This allows us to study quantum dots even when they are virtually isolated from the reservoirs. This is demonstrated in Fig. 3.4d, where the tunnel coupling between the dot and the leads is so weak that the Coulomb peaks are not resolved anymore. Even in this regime, the QPC can track the transitions in electron number. We will explore this functionality in more detail in chapter 6.
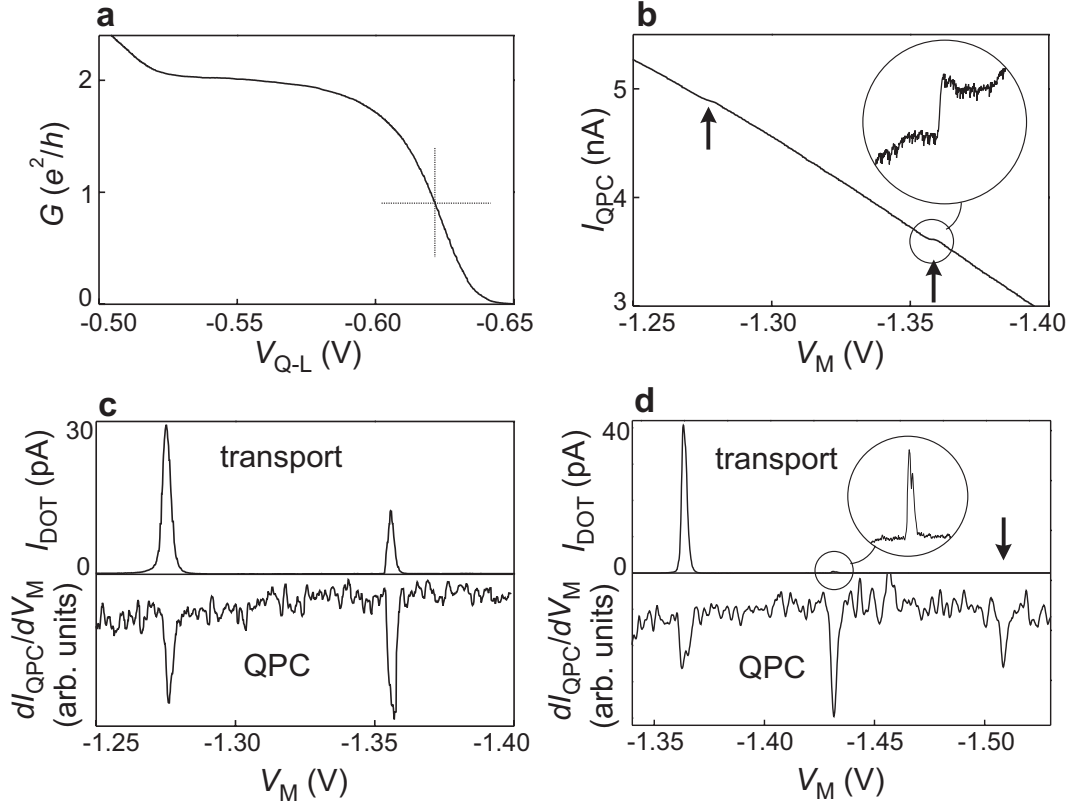
Figure 3.4: Operating the QPC as a charge detector of a single dot. **(a)** Conductance, G, of the left QPC versus gate voltage, V_{Q-L}, showing the last quantized plateau (at $G = 2e^2/h$) and the transition to complete pinch-off ($G = 0$). The QPC is set to the point of highest charge sensitivity, at $G \approx e^2/h$ (indicated by the dashed cross). **(b)** Current through the left QPC, I_{QPC}, versus left-dot gate voltage, V_M, with $V_{SD1} = 250$ μV and $V_{SD2} = V_{DOT} = 0$. Steps indicated by arrows correspond to changes in the number of electrons on the left dot. Encircled inset: the last step (~ 50 pA high), with the linear background subtracted. **(c)** Comparison between transport and charge detection measurements. Upper panel: Coulomb peaks measured in transport current through the left dot, with $V_{DOT} = 100$ μV and $V_{SD1} = V_{SD2} = 0$. Lower panel: changes in the number of electrons on the left dot measured with the left QPC, with $V_{SD1} = 250$ μV and $V_{SD2} = V_{DOT} = 0$). **(d)** Measurements as in (c), but in the regime of very weak dot-lead coupling. In the lower panel, charge detection shows an electron transition around -1.5 V, indicated by the arrow, whereas the Coulomb peak is not resolved in the transport measurement (upper panel). (Because the signal in (d) is a numerical derivate of I_{QPC} some dips show a much worse signal-to-noise ratio than in (c), where the signal is obtained using a lock-in technique.)

3.4   Double dot charge stability diagram

The QPC can also detect changes in the charge configuration of the *double* dot. To demonstrate this, we use the QPC on the right to measure dI_{QPC}/dV_L versus V_L and V_{P_R} (Fig. 3.5a), where V_L controls (mainly) the number of electrons on the left dot, and V_{P_R} (mainly) that on the right. Dark lines in the figure signify a dip in dI_{QPC}/dV_L, corresponding to a change in the total number of electrons on the double dot. Together these lines form the so-called 'honeycomb diagram' [14, 15]. The almost-horizontal lines correspond to a change in the number of electrons on the left dot, whereas almost-vertical lines indicate a change in the electron number on the right.

In the upper left region the 'horizontal' lines are not present, even though the QPC can still detect changes in the charge, as demonstrated by the presence of the 'vertical' lines. We conclude that in this region the *left* dot contains zero electrons. Similarly, a disappearance of the 'vertical' lines occurs in the lower right region, showing that here the *right* dot is empty. In the upper right region, the absence of lines shows that here the *double* dot is completely empty. This is indicated by the electron occupation numbers '00'.

We are now able to identify the exact charge configuration of the double dot in every honeycomb cell, by simply counting the number of 'horizontal' and 'vertical' lines that separate it from the '00' region. In Fig. 3.5b the first few honeycomb cells are labelled according to their charge configuration, with e.g. the label '21' meaning 2 electrons in the left dot and 1 on the right.

Besides the dark lines, also short bright lines are visible, signifying a peak in dI_{QPC}/dV_L. These bright lines correspond to an electron being transferred from one dot to the other, with the total electron number remaining the same. (The fact that some charge transitions result in a dip in dI_{QPC}/dV_L and others in a peak, derives from the fact that we use the QPC on the *right* and apply the modulation to the gate on the *left*. When an electron is pushed out of the double dot by making V_L more negative, the QPC opens up and dI_{QPC}/dV_L displays a dip. When V_L pushes an electron from the left to the right dot, the QPC is closed slightly, resulting in a peak.)

The visibility of all lines in the honeycomb pattern demonstrates that the QPC is sufficiently sensitive to detect *all* charge transitions in the double quantum dot. Generally, we find the QPC on the right side to be about a factor of 2 more sensitive to changes in the electron number on the right dot than to changes in the electron number on the left dot.
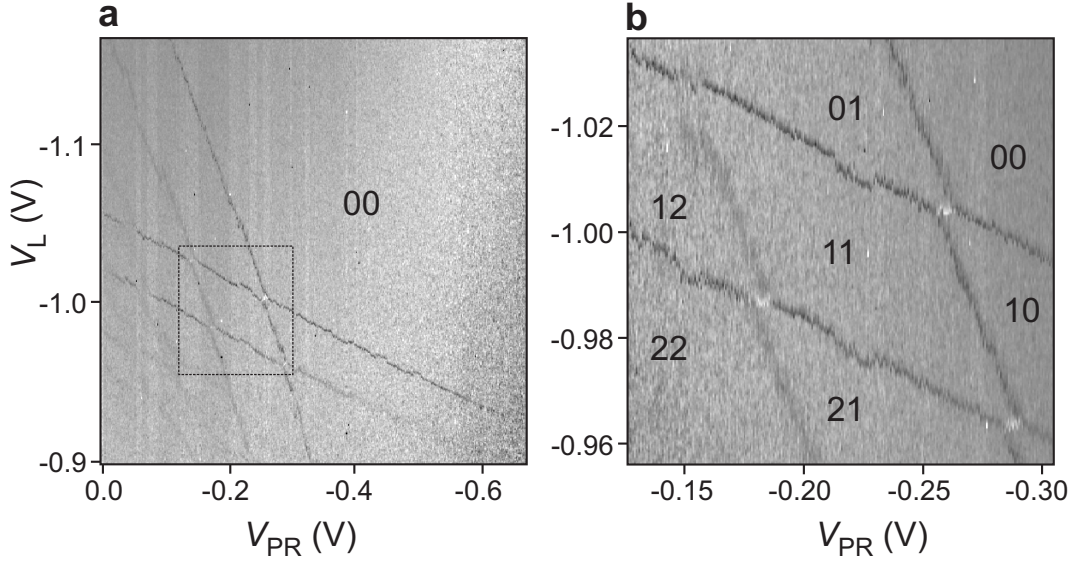
Figure 3.5: Using the QPC to measure the charge configuration of a double quantum dot in the few-electron regime. **(a)** dI_{QPC}/dV_L (in grayscale) versus V_L and V_{P_R}, with $V_{SD2} = 100~\mu$V and $V_{SD1} = V_{DOT} = 0$. A small modulation (0.3 mV at 17.77 Hz) is applied to V_L, and the resulting modulation in I_{QPC} is measured with a lock-in amplifier to give dI_{QPC}/dV_L directly. The label '00' indicates the region where the double dot is completely empty. In the bottom left corner the dark lines are poorly visible. Here the tunnel rates to the reservoirs are quite large, leading to smearing of the steps in the QPC current, and therefore to smaller dips in dI_{QPC}/dV_L. **(b)** Zoom-in of Fig. 3.5a, showing the 'honeycomb' diagram for the first few electrons in the double dot. The black labels indicate the charge configuration, with '21' meaning 2 electrons in the left dot and 1 on the right.

3.5 Tunable tunnel barriers in the few-electron regime

In measurements of transport through lateral double quantum dots, the few-electron regime has never been reached [15]. The problem is that the gates that are used to deplete the dots also strongly influence the tunnel barriers. Reducing the electron number would therefore always lead to the Coulomb peaks becoming unmeasurably small, but not necessarily due to an empty double dot. The QPC detectors now permit us to compare charge and transport measurements.

Figure 3.6a shows the current through the double dot in the same region as shown in Fig. 3.5b. In the bottom left region the gates are not very negative, hence the tunnel barriers are quite open. Here the resonant current at the charge transition points is quite high (~ 100 pA, dark gray), and lines due to cotunneling
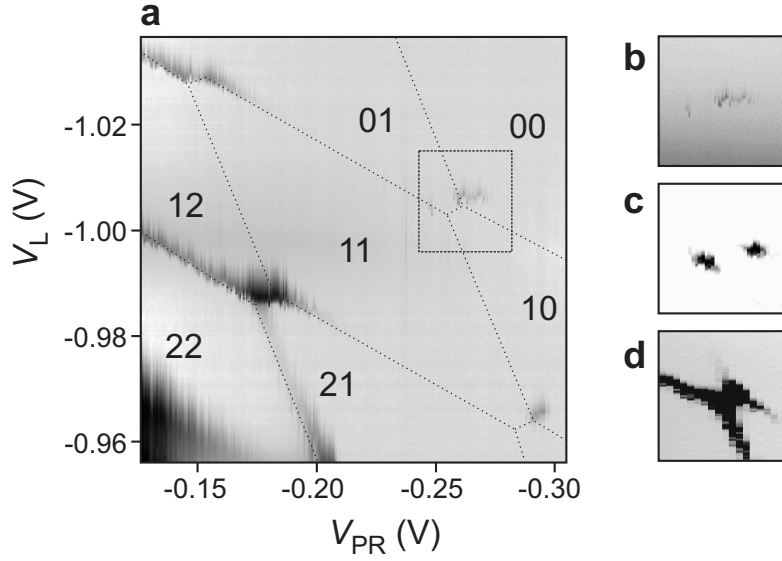
Figure 3.6: Current through the double quantum dot in the few-electron regime. **(a)** I_{DOT} (in logarithmic grayscale) versus V_L and V_{P_R} in the same region as shown in Fig. 3.5b, with $V_{DOT} = 100 \ \mu$V and $V_{SD1} = V_{SD2} = 0$. Dotted lines are extracted from Fig.3.5b. Dark gray indicates a current flowing, with the darkest regions (in the bottom left corner) corresponding to ~ 100 pA. In the light gray regions current is zero due to Coulomb blockade. Inside the dashed square, the last triple points are faintly visible (~ 1 pA). (A smoothly varying background current due to a small leakage current from a gate to the 2DEG has been subtracted from all traces.) **(b)** Close-up of the region inside the dashed square in (a), showing the last two triple points before the double dot is completely empty. The current at these triple points is very small (< 1 pA) since the tunnel barriers are very opaque. **(c)** Same two triple points for different values of the voltage applied to the gates defining the tunnel barriers. For these settings, the two individual triple points are well resolved, with a height of about 5 pA. The cotunneling current is not visible. **(d)** Same two triple points, but now with the gate voltages such that the tunnel barriers are very transparent. The current at the triple points is about 70 pA, and the cotunneling current is clearly visible.

are also visible [15]. Towards the top right corner the gate voltages become more negative, thereby closing off the barriers and reducing the current peaks (lighter gray). The last 'triple points' [15] that are visible (< 1 pA) are shown in the dashed square. Using the dotted lines, extracted from the measured charge transition lines in Fig. 3.5b, we label the various regions in the figure according to the charge configuration of the double dot. Apart from a small shift, the dotted lines correspond nicely to the regions where a transport current is visible. This allows us to be confident that the triple points in the dashed square are really the last ones before the double quantum dot is empty. We are thus able to measure
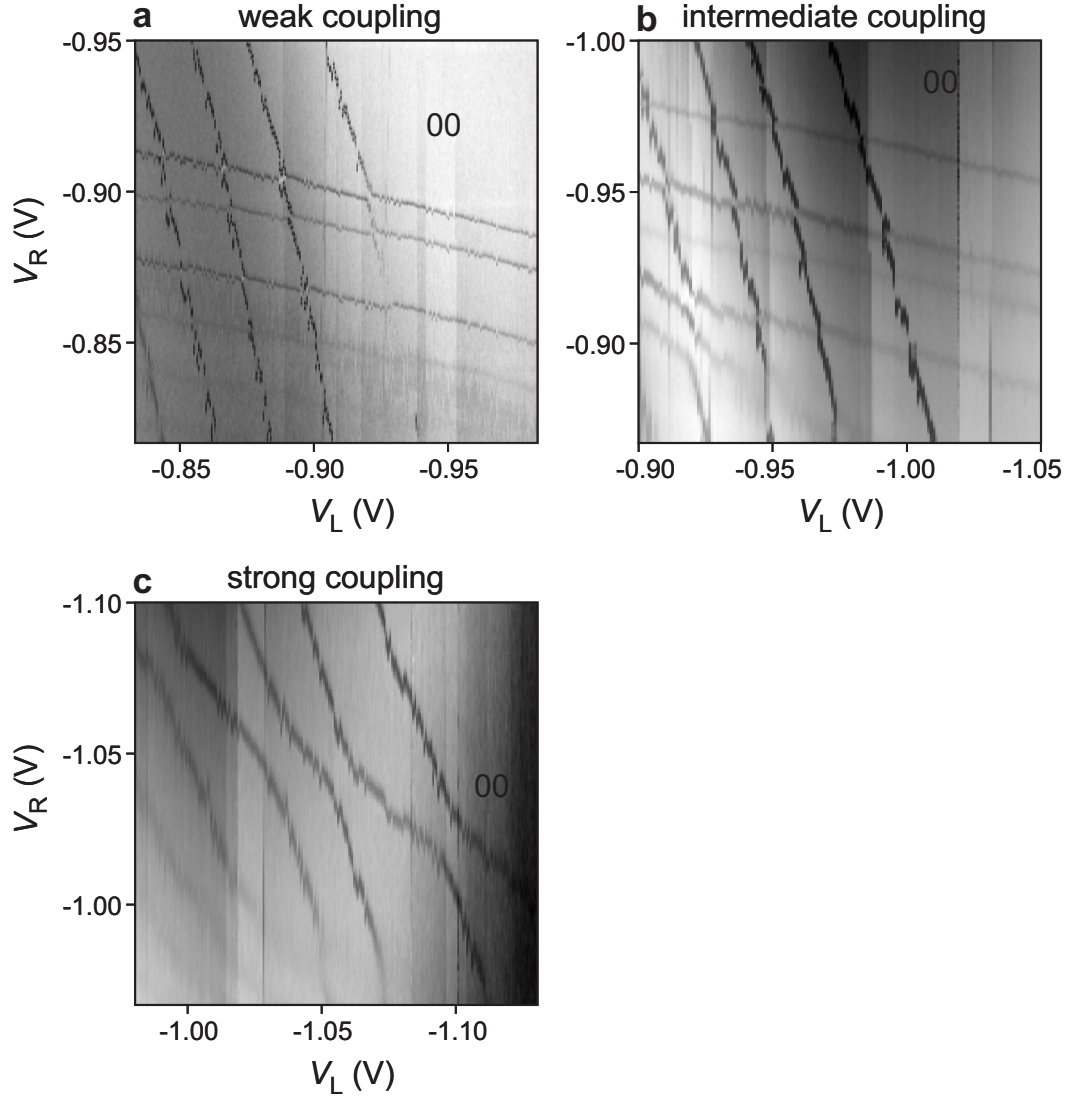
Figure 3.7: Controlling the inter-dot coupling with V_M. These charge stability diagrams of the double quantum dot are measured using the QPC on the left. A small modulation (3 mV at 235 Hz) is applied to gate P_R, and dI_{QPC}/dV_{P_R} is measured with a lock-in amplifier and plotted in grayscale versus V_L and V_R. A magnetic field of 6 Tesla is applied in the plane of the 2DEG. **(a)** Weak-coupling regime. V_M is such that all dark lines indicating charge transitions are straight. The tunnel-coupling between the two dots is therefore negligible compared to the capacitive coupling. **(b)** Intermediate-coupling regime. V_M is 0.07 V less negative than in (a), such that lines in the bottom left corner are slightly curved. This signifies that here the inter-dot tunnel-coupling is comparable to the capacitive coupling. **(c)** Strong-coupling regime. V_M is 0.1 V less negative than in (b), such that all lines are very curved. This implies that the tunnel-coupling is dominating over the capacitive coupling and the double dot behaves as a single dot.

transport through a one-electron double quantum dot.

Even in the few-electron regime, the double dot remains fully tunable. By changing the voltage applied to gate T, we can make the tunnel barriers more transparent, leading to a larger current through the device. We use this procedure to increase the current at the last set of triple points. For the gate voltages used in Fig. 3.6b, the resonant current is very small (< 1 pA), and the triple points are only faintly visible. By making V_T less negative, the resonant current peaks grow to about 5 pA (Fig. 3.6c). The two triple points are clearly resolved and the cotunneling current is not visible. By changing V_T even more, the current at the last triple points can be increased to ~ 70 pA (Fig. 3.6d). For these settings, the triple points have turned into lines, due to the increased cotunneling current. This sequence demonstrates that we can tune the few-electron double dot from being nearly isolated from the reservoirs, to being very transparent.

We can also control the inter-dot coupling, by changing the voltage applied to gate M. This is demonstrated with a QPC charge measurement. We apply a square wave modulation of 3 mV at 235 Hz to the rightmost plunger gate, P_R, and measure dI_{QPC}/dV_{P_R} using a lock-in amplifier. Fig. 3.7a shows the familiar honeycomb diagram in the few-electron regime. All lines indicating charge transitions are very straight, implying that for the gate settings used, the tunnel-coupling between the two dots is negligible compared to the capacitive coupling. This is the so-called weak-coupling regime. (We note that the regular shape of the honeycomb pattern demonstrates that the double dot as a whole is still quite well-coupled to the leads, so that the total number of electrons can always find its lowest-energy value, unlike in Ref. [16].) By making V_M less negative, the tunnel barrier between the two dots is made more transparent, and the intermediate-coupling regime is reached (Fig. 3.7b). Most lines are still straight, except in the bottom left corner, where they are slightly curved. This signifies that here the inter-dot tunnel-coupling is comparable to the capacitive coupling. If we make V_M even less negative, we reach the strong-coupling regime (Fig. 3.7c). In this case, all lines are very curved, implying that the tunnel-coupling is dominating over the capacitive coupling. In this regime the double dot behaves like a single dot.

3.6 Photon-assisted tunneling

The use of gated quantum dots for quantum state manipulation in time requires the ability to modify the potential at high frequencies. We investigate the high-frequency behavior in the region around the last triple points (Fig. 3.8a), with a
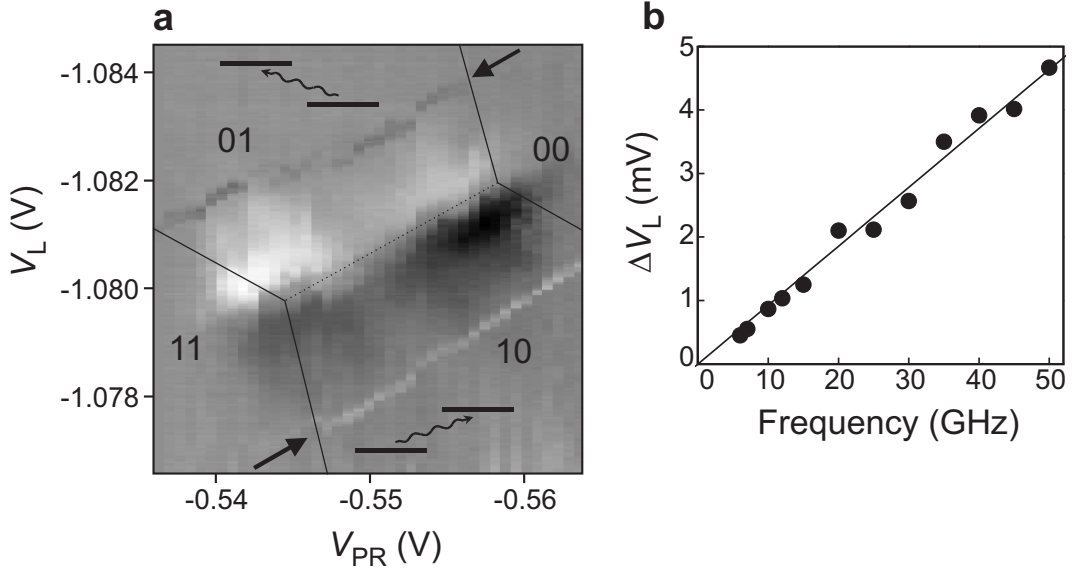
Figure 3.8: Photon-assisted tunneling in a one-electron double quantum dot. **(a)** Current through the double dot at the last set of triple points, with zero bias voltage ($V_{DOT} = V_{SD1} = V_{SD2} = 0$). A microwave signal of 50 GHz is applied to P_L. The microwaves pump a current, I_{DOT}, by absorption of single photons [15]. This photon-assisted current shows up as two lines, indicated by the two arrows. The white line (bottom) corresponds to electrons being pumped from the left to the right reservoir, the dark line (top) corresponds to pumping in the reverse direction. In the middle, around the dotted line separating the 01 from the 10 configuration, a finite current is induced by an unwanted voltage drop over the double dot, due to asymmetric coupling of the ac-signal to the two leads. **(b)** Separation between the two photon-assisted tunneling lines versus microwave frequency. The dependence is linear down to the lowest frequency of about 6 GHz, from which it follows that the inter-dot tunnel coupling (half the energy difference between bonding and anti-bonding state) is smaller than ~ 12 μeV.

50 GHz microwave-signal applied to gate P_L. At the dotted line the 01 and 10 charge states are degenerate in energy, so one electron can tunnel back and forth between the two dots. Away from this line there is an energy difference and only one charge state is stable. However, if the energy difference matches the photon energy, the transition to the other dot is possible by absorption of a single photon. Such photon-assisted tunneling events give rise to the two lines indicated by the arrows. At the lower (higher) line electrons are pumped from the the left (right) dot to the other one, giving rise to a negative (positive) photon-assisted current. We find that the distance (in terms of gate voltage) between the two photon-assisted tunneling lines, ΔV_L, scales linearly with frequency (Fig. 3.8b), as expected in the weak-coupling regime [15]. From the absence of bending of

the line in Fig. 3.8b down to a frequency of 6 GHz, it follows that the inter-dot tunnel coupling is smaller than about 12 μeV.

3.7   Real-time observation of single-electron tunneling

If the time between tunnel events is longer than the time needed to determine the number of electrons on the dot – or equivalently: if the bandwidth of the charge detection exceeds the tunnel rate – electron tunneling can be observed in real-time. In our setup, the measured current noise integrated from dc is comparable to the current step induced by an electron tunneling on or off the dot ($\Delta I_{QPC,e}$) for a bandwidth of 80 kHz, and 2.5 times smaller than $\Delta I_{QPC,e}$ around 40 kHz [17]. These numbers correspond to a QPC voltage bias of 1 mV. A larger voltage bias is found to influence the tunneling statistics, possibly due to photon-assisted tunneling. We set the cut-off frequency of the external low-pass filter at 40 kHz, so we should see clear steps in time traces of the QPC current, corresponding to single electrons tunneling on or off the dot.

We use a one-electron single dot defined by gates T, M and R (see Fig. 3.1c),
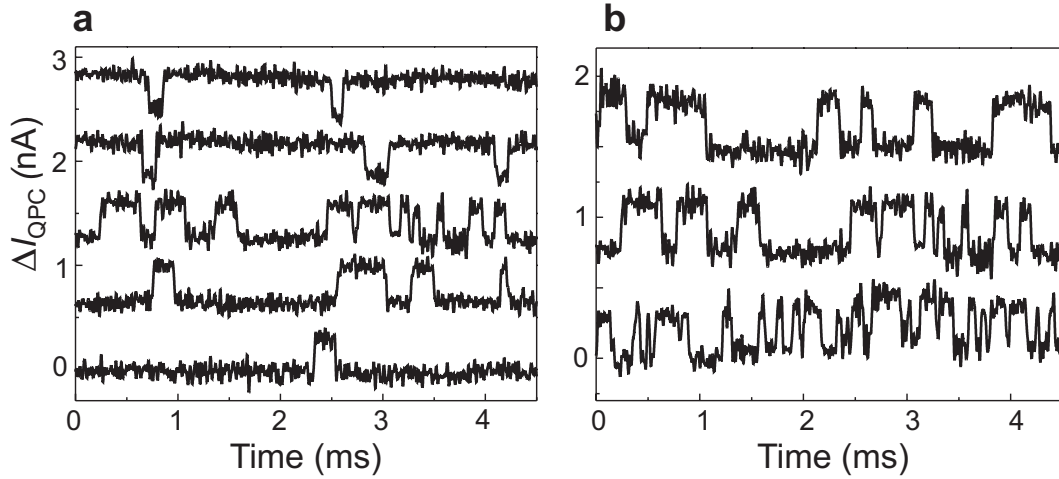
Figure 3.9: Measured changes in the QPC current, ΔI_{QPC}, with the electrochemical potential in the dot and in the reservoir nearly equal. ΔI_{QPC} is 'high' and 'low' for 0 and 1 electrons on the dot respectively (QPC bias $V_{SD2} = 1$ mV; the steps in ΔI_{QPC} are ≈ 300 pA). The small roll of the baseline is at 50 Hz. Traces are offset for clarity. **(a)** The dot potential is lowered from top to bottom. **(b)** The tunnel barrier is lowered from top to bottom.

and tune the tunnel barriers such that the dot is virtually isolated from the lead that is connected to the QPC channel path. In this regime, the dot is operated as a charge box, coupled to only one reservoir. Next, the electrochemical potential in the dot is aligned with the electrochemical potential in the reservoir. Now the electron can *spontaneously* tunnel back and forth between the dot and the lead, and the QPC current should exhibit a random telegraph signal (RTS). This is indeed what we observe experimentally (Fig. 3.9). In order to ascertain that the RTS really originates from electron tunnel events between the dot and the reservoir, we verify that (1) the dot potential relative to the Fermi level determines the fraction of the time an electron resides in the dot (Fig. 3.9a) and (2) the dot-lead tunnel barrier sets the RTS frequency (Fig. 3.9b). The shortest steps that clearly reach above the noise level are about $8\,\mu$s long. This is consistent with the 40 kHz filter frequency, which permits a rise time of $8\,\mu$s.

We can also *induce* tunnel events by pulsing the dot potential using fast voltage pulses on the plunger gate, so N predictably changes from 0 to 1 and back to 0. The response of the QPC current to such a pulse contains two contributions (Fig. 3.10a). First, the shape of the pulse is reflected in ΔI_{QPC}, as the pulse gate couples capacitively to the QPC. Second, some time after the pulse is started, an electron tunnels into the dot and ΔI_{QPC} goes down by about 300 pA. Similarly, ΔI_{QPC} goes up by 300 pA when an electron leaves the dot, some time after the pulse ends. We observe that the time before tunneling takes place is randomly
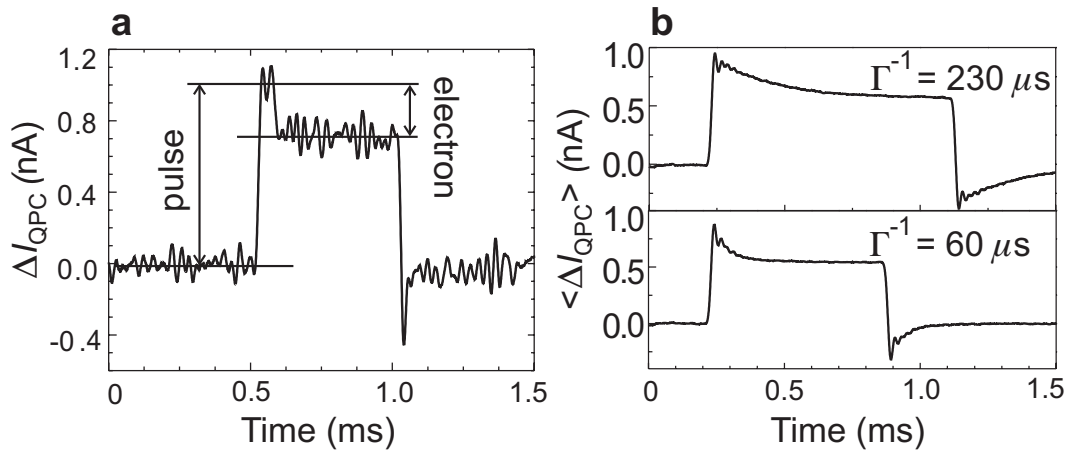
Figure 3.10: (a) Measured changes in the QPC current, ΔI_{QPC}, when a pulse is applied to gate P_R, near the degeneracy point between 0 and 1 electrons on the dot ($V_{SD2} = 1$ mV). (b) Average of 286 traces as in (a). The top and bottom panel are taken with a different setting of gate M. The damped oscillation following the pulse edges is due to the 8th-order 40 kHz filter used.

distributed, and obtain a histogram of this time simply by averaging over many single-shot traces (Fig. 3.10b). The measured distribution decays exponentially with the tunnel time, characteristic of a Poisson process. The average time before tunneling corresponds to Γ^{-1}, and can be tuned by adjusting the tunnel barrier.

3.8 Conclusions

The realization of a controllable few-electron quantum dot circuit represents a significant step towards controlling the coherent properties of single electron spins in quantum dots [1]. Integration with the QPCs permits charge read-out of closed quantum dots. The real-time detection of electron tunneling opens the way to read-out of electron spins by utilizing spin-to-charge conversion. We note that charge read-out only affects the spin state indirectly, via the spin-orbit interaction. The back-action on the spin should therefore be small (until spin-to-charge conversion is initiated), and can be further suppressed by switching on the charge detector only during the read-out stage. In the following chapters, we will use the quantum dot circuit presented here to study the spin states of a few-electron dot.

References

[1] D. Loss and D. P. DiVincenzo, Phys. Rev. A **57**, 120 (1998).

[2] P. M. Petroff, A. Lorke, and A. Imamoglu, Phys. Today, 46 (May 2001).

[3] L. P. Kouwenhoven, D. G. Austing, and S. Tarucha, Rep. Prog. Phys. **64** (6), 701 (2001).

[4] M.T. Bjork *et al.*, Nano Lett. 4 (9), 1621 (2004).

[5] P. Jarillo-Herrero *et al.*, Nature **429**, 389 (2004).

[6] K. Ono, D. G. Austing, Y. Tokura, and S. Tarucha, Science **297**, 1313 (2002).

[7] T. Hatano, M. Stopa, T. Yamaguchi, T. Ota, K. Yamada, and S. Tarucha, Phys. Rev. Lett. **93**, 066806 (2004).

 [8] L. P. Kouwenhoven, C. M. Marcus, P. L. McEuen, S. Tarucha, R. M. Wester-velt, and N. S. Wingreen, in *Mesoscopic Electron Transport*, edited by L. L. Sohn, L. P. Kouwenhoven, and G. Schön, NATO Advanced Study Institutes, Ser. E, Vol. **345** (Kluwer, Dordrecht, Boston, 1997), pp. 105-214.

 [9] M. Ciorga, A. S. Sachrajda, P. Hawrylak, C. Gould, P. Zawadzki, S. Jullian, Y. Feng, and Z. Wasilewski, Phys. Rev. B **61**, R16315 (2000).

[10] A. Sachrajda, private communication (2001).

[11] L.P. Kouwenhoven and L.I. Glazman, Physics World **14**, 33 (2001).

[12] M. Field, C. G. Smith, M. Pepper, D. A. Ritchie, J. E. F. Frost, G. A. C. Jones, and D. G. Hasko, Phys. Rev. Lett. **70**, 1311 (1993).

[13] D. Sprinzak, Y. Ji, M. Heiblum, D. Mahalu, and H. Shtrikman, Phys. Rev. Lett. **88**, 176805 (2002).

[14] H. Pothier, P. Lafarge, C. Urbina, D. Estève, and M. H. Devoret, Europhys. Lett. **17**, 249 (1992).

[15] W. G. van der Wiel, S. De Franceschi, J. M. Elzerman, T. Fujisawa, S. Tarucha, and L. P. Kouwenhoven, Rev. Mod. Phys. **75**, 1 (2003), see also cond-mat/0205350v2.

[16] A. W. Rushforth, C. G. Smith, M. D. Godfrey, H. E. Beere, D. A. Ritchie, and M. Pepper, Phys. Rev. B **69**, 113309 (2004).

[17] L. M. K. Vandersypen, J. M. Elzerman, R. N. Schouten, L. H. Willems van Beveren, R. Hanson and L. P. Kouwenhoven, Appl. Phys. Lett. **85**, 4394 (2004).

Chapter 4

Zeeman energy and spin relaxation
of a single electron

R. Hanson, B. Witkamp, L. M. K. Vandersypen,
L. H. Willems van Beveren, J.M. Elzerman
and L. P. Kouwenhoven

In this chapter, we study the spin states of a single electron confined in a quantum dot. In a magnetic field, applied parallel to the two-dimensional electron gas in which the quantum dot is defined, Zeeman splitting of the orbital states is directly observed by measurements of electron transport through the dot. By applying short voltage pulses, we can populate the excited spin state with one electron and monitor relaxation of the spin. We find a lower bound on T_1 of 50 μs at 7.5 T, only limited by our signal-to-noise ratio. A continuous measurement of the charge on the dot has no observable effect on the spin relaxation.

4.1   Introduction

The electron spin states in quantum dots (QDs) are expected to be very stable, because the zero-dimensionality of the electron states in QDs leads to a significant suppression of the most effective 2D spin-flip mechanisms [1]. Relaxation between Zeeman sublevels in closed GaAs QDs is expected to be dominated by hyperfine interaction with the nuclei at magnetic fields below 0.5 T [3] and by spin-orbit interaction at higher fields [4]. At 1 T, theory predicts a T_1 of 1 ms in GaAs [4].

For comparison, in n-doped self-assembled InAs QDs containing one resident electron, pump-probe photoluminescence measurements gave a single-electron spin relaxation time of 15 ns (at B=0 T, T= 10 K) [5]. In undoped self-assembled InAs QDs, the exciton polarization is frozen throughout the exciton lifetime, giving a relaxation time >20 ns [6].

Electrical measurements of the single-electron spin relaxation time have up to now remained elusive. In vertical QDs, where electrical measurements on a single electron were reported almost a decade ago [7], it has been difficult to directly resolve the Zeeman splitting of orbitals [8]. As demonstrated in chapter 3, the one-electron regime was also reached in single [9] and double lateral GaAs QDs [10], which are formed electrostatically within a two-dimensional electron gas (2DEG) by means of surface gates.

In this chapter we study the spin states of a one-electron lateral QD directly, by performing energy spectroscopy and relaxation measurements. We observe a clear Zeeman splitting of the orbital states in electron transport measurements through the QD, and find no signature of spin relaxation in our experimental time window, leading to a lower bound on T_1 of 50 μs. This lower bound is two to three orders of magnitude longer than spin relaxation times observed in bulk n-type GaAs [11], GaAs quantum wells [12] and InAs QDs [5].

4.2   Zeeman energy

The quantum dot is defined in a GaAs/Al$_{0.3}$Ga$_{0.7}$As heterostructure, containing a 2DEG 90 nm below the surface with an electron density $n_s = 2.9 \times 10^{11}$ cm^{-2} (Fig. 4.1a). A magnetic field (0-14 T) is applied parallel to the 2DEG. All measurements are performed in a dilution refrigerator at base temperature $T = 20$ mK.

We tune the device to the few-electron regime and identify the 0↔1 electron transition by the absence of further transitions under applied source-drain voltage up to 10 mV. The electron number is confirmed by using the nearby QPC as a charge detector [14, 10, 15]. We find a charging energy of 2.4 meV and an orbital
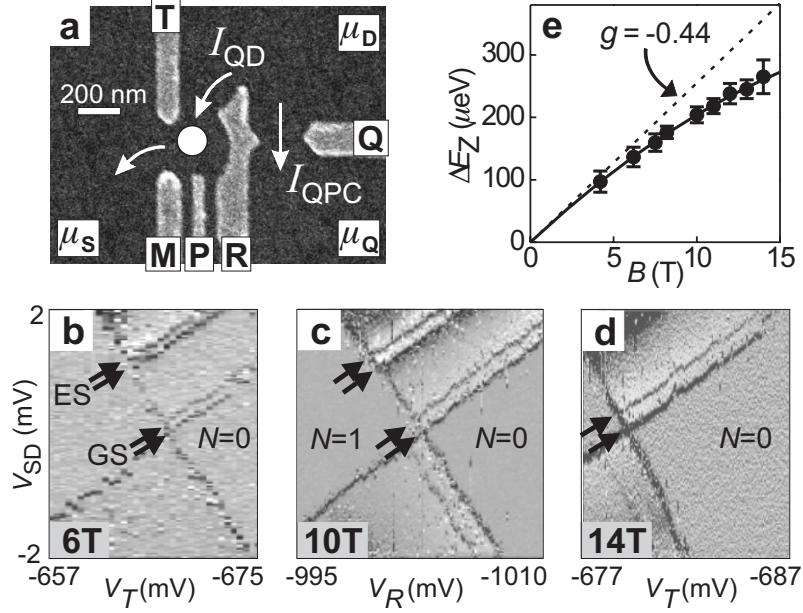
Figure 4.1: **(a)** Scanning Electron Micrograph of the metallic surface gates [13]. Gates M, R and T are used to form the quantum dot indicated by a white circle. Additionally, gate Q can be used to form a quantum point contact (QPC). To apply high-frequency signals, gate P is connected to a coaxial cable. Currents through the dot, I_{QD}, and through the QPC, I_{QPC}, are measured as a function of applied bias voltage, $V_{SD} = (\mu_S - \mu_D)/e$ and $V_{QD} = (\mu_Q - \mu_D)/e$ respectively. **(b)-(d)** Differential conductance dI_{QD}/dV_{SD} as a function of V_{SD} and gate voltage near the 0↔1 electron transition, at parallel magnetic fields of 6, 10 and 14 T. Darker corresponds to larger dI_{QD}/dV_{SD}. The zero-field spin degeneracy of both the ground state (GS) and the first orbital excited state (ES) is lifted by the Zeeman energy as indicated by arrows. **(e)** Extracted Zeeman splitting ΔE_Z as a function of B. At high fields a clear deviation from the bulk GaAs g-factor of -0.44 (dashed line) is observed.

level spacing of 1.1 meV at $B = 0$ T.

In a parallel magnetic field, the electron states acquire a Zeeman energy shift, which causes the orbital levels to split by $\Delta E_Z = g\mu_B B$ [16]. Figs. 4.1b-d show stability diagrams [7] around the 0↔1 electron transition, measured at $B = 6$ T, 10 T and 14 T. A clear Zeeman splitting of both ground and first orbital excited state is seen directly in this spectroscopy measurement [17]. (Because of the large asymmetry in the tunnel barriers, the visibility of the Zeeman splitting is very different for positive and for negative bias [18].) Using this measurement technique, we can extract the value of the Zeeman splitting ΔE_Z. In Fig. 4.1e, ΔE_Z is plotted as a function of B. At high fields a clear deviation from the bulk GaAs g-factor of -0.44 (dashed line) is observed.
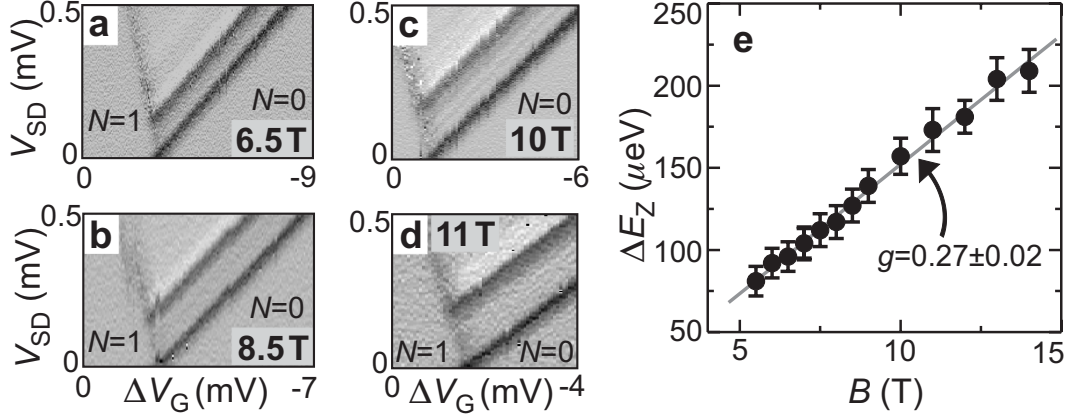
Figure 4.2: (a)-(d) High source-drain bias measurements similar to Fig. 4.1(b)-(d) on a different heterestructure, with a 2DEG 60 nm below the surface, for in-plane magnetic fields of (a) 6.5 T, (b) 8.5 T, (c) 10 T, and (d) 11 T. **(e)** Extracted Zeeman splitting ΔE_Z as a function of B. The value of $|g|$ is 0.27 for all fields.

A least-squares fit of the data to a second-order polynomial, which extrapolates with negligible deviation to the origin, gives

$$|g| = (0.43 \pm 0.04) - (0.0077 \pm 0.0020)\, B\ (T)\ , \tag{4.1}$$

similar to early measurements on 2DEGs [19]. If we force the fit to be linear in B, we get $|g| = 0.29 \pm 0.01$, with a zero-field splitting $\Delta E_{Z,B=0} = (34 \pm 6)\mu\text{eV}$.

For comparison, we present similar measurements on a different heterostructure, where the 2DEG is 60 nm below the surface. Figure 4.2a-d show high source-drain bias measurements around the 0↔1 electron transition for different in-plane magnetic fields. The extracted B-dependence of ΔE_Z is given in Fig. 4.2e. The value of the g-factor, $|g| = 0.27 \pm 0.02$, is significantly smaller than the bulk value. Furthermore, in contrast to the data in Fig. 4.1e, there is no dependence on magnetic field.

Factors which can influence the magnetic field dependence of the g-factor include: (1) extension of the electron wave function into the $Al_{0.3}Ga_{0.7}As$ region, where $g = +0.4$ [20, 21], (2) thermal nuclear polarization, which decreases the effective magnetic field through the hyperfine interaction [22], (3) dynamic nuclear polarization due to electron-nuclear flip-flop processes in the dot, which enhances the effective magnetic field [22], (4) the nonparabolicity of the GaAs conduction band [20] and (5) the spin-orbit coupling [23]. Factors 2 and 3 can not explain our data, since they do not depend on the heterostructure. More experiments are needed to separate the other effects, e.g. by measuring the dependence of the g-factor on the orientation of the in-plane magnetic field [23]. However, this is

outside the scope of this research. In the remaining part of the chapter, we will use the device shown in Fig. 4.1a.

4.3   Measuring the spin relaxation time

The two spin states $|\uparrow\rangle$ (lowest energy) and $|\downarrow\rangle$ can be used as the basis states of a quantum bit [24, 25]. In order to perform quantum operations and to allow sufficient time for read-out of the quantum bit, it is necessary that the spin excited state $|\downarrow\rangle$ be stable. We investigate this by measuring the relaxation time from $|\downarrow\rangle$ to $|\uparrow\rangle$. By applying short pulses to gate P, we can modulate the potential of the dot and thus the position of the energy levels relative to the electrochemical potentials of the leads, μ_S and μ_D. This enables us to populate the spin excited state $|\downarrow\rangle$ and monitor relaxation to $|\uparrow\rangle$. The applicability of various pulse methods for measuring the spin relaxation time depends on two timescales. If the relaxation rate W ($=1/T_1$) is at least of the same order as the outgoing tunnel rate Γ_D, i.e. $W \geq \Gamma_D$, we can determine T_1 by applying single-step pulses. This method has previously been used to measure the relaxation time between orbital levels in a QD ($\sim$10 ns) [2]. In the other limit, $W < \Gamma_D$, a more elaborate method using double-step pulses is needed [2]. We proceed as follows. First, we apply single-step pulses to show that $W < \Gamma_D$. Then we apply double-step pulses to measure T_1. All data shown are taken at $B = 7.5$ T, and reproduced at 14 T. At fields below 6 T the Zeeman splitting is too small to be resolved in pulse experiments. The bias voltage is always much smaller than the charging energy, thus allowing at most one electron on the dot.

4.4   Spin relaxation measurement using single-step pulses

The single-step pulses are schematically depicted in Fig. 4.3a. Fig. 4.3b shows current traces for different amplitudes of the pulses. Transport of electrons through the ground state takes place when $|\uparrow\rangle$ lies in the bias window (i.e. $\mu_S > E_\uparrow > \mu_D$). When we apply single-step pulses, this condition is met at two different values of the gate voltage V_T and therefore the Coulomb peak splits in two. Fig. 4.3c shows the positions of the energy levels during the two phases of the pulse for the left peak in Fig. 4.3b. Here, electrons flow from source to drain during the "high" phase of the pulse. Similarly, Fig. 4.3e corresponds to the right peak in Fig. 4.3b, where ground state transport occurs during the "low" phase of the
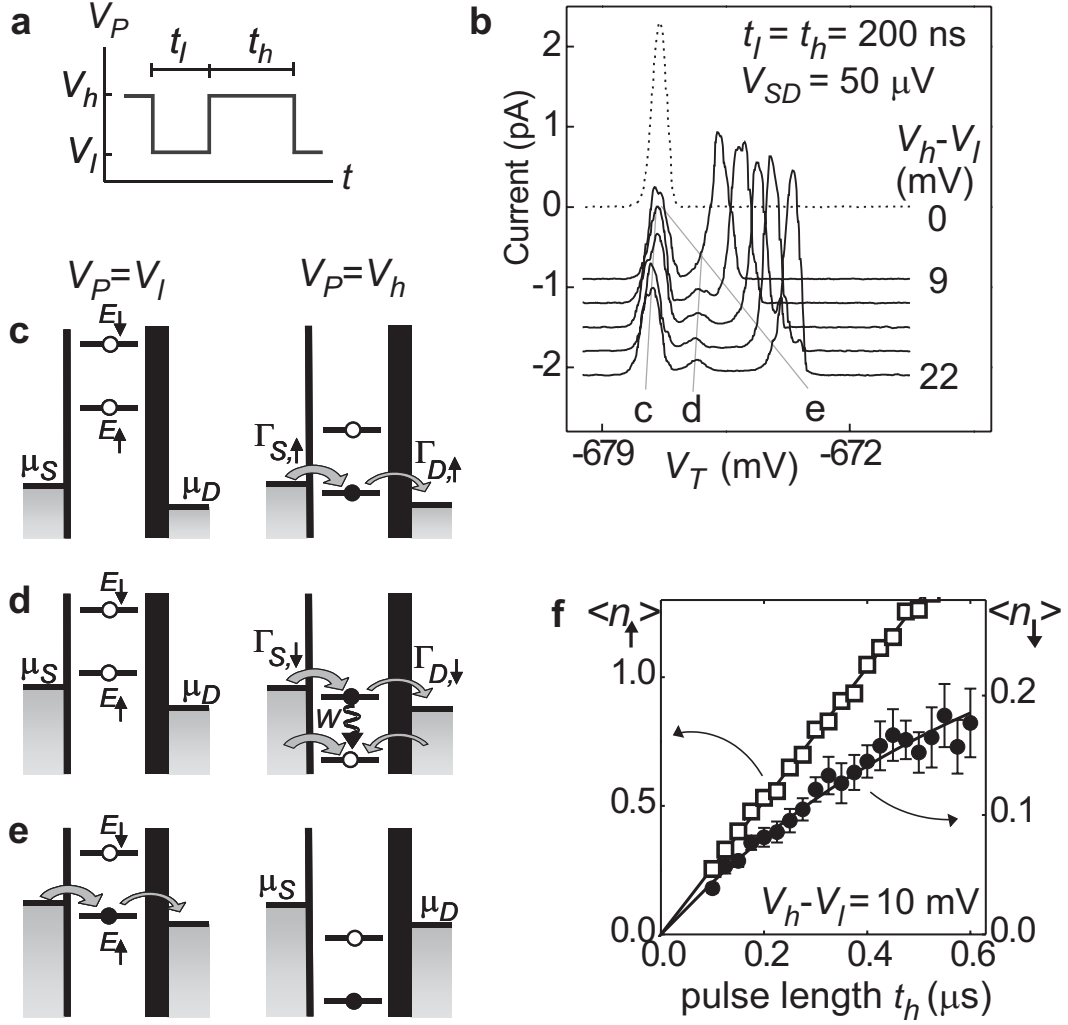
Figure 4.3: One-electron spin relaxation studied using single-step pulses at 7.5T. **(a)** Schematic waveform of the pulse train (rise/fall time of 0.2 ns). **(b)** Current traces under applied pulses, offset for clarity. **(c)**-**(e)** Diagrams showing the position of the energy levels during the two phases of the pulse for threee different gate voltage settings, corresponding to the three peaks in (b). **(f)** Average number of electrons tunneling per cycle $(=I(t_l+t_h)/e)$ through the ground state $<n_\uparrow>$, as in (c), and through the excited state $<n_\downarrow>$, as in (d), vs. pulse length t_h. The $<n_\uparrow>$ shows no decay, as expected for a stable current, whereas $<n_\downarrow>$ saturates. However, this saturation is not due to spin relaxation (see text).

pulse. When the pulse amplitude exceeds the Zeeman splitting ($\approx$160 μeV), an extra current peak becomes clearly visible. This peak is due to transient transport via the spin-down state $|\downarrow\rangle$ during the "high" phase of the pulse (Fig. 4.3d). The transient current flows until $|\uparrow\rangle$ becomes occupied and Coulomb blockade

prohibits other electrons to enter the dot. Occupation of $|\uparrow\rangle$ can happen either via tunneling of an electron from the leads into $|\uparrow\rangle$ when the dot is empty, or by spin relaxation from $|\downarrow\rangle$ to $|\uparrow\rangle$. For both these processes, the probability to have occurred increases with time. Therefore, the number of electrons tunneling via $|\downarrow\rangle$ per cycle, $<n_\downarrow>$, saturates with increasing pulse length t_h. In particular, if the tunnel rate Γ_S through the incoming barrier is much larger than the tunnel rate Γ_D through the outgoing barrier, i.e. $\Gamma_S \gg \Gamma_D$ [26], it can be shown that [18, 27]

$$<n_\downarrow> \simeq A\Gamma_{D,\downarrow}(1 - e^{-Dt_h})/D \ , \tag{4.2}$$

where $A \simeq \Gamma_{S,\downarrow}/(\Gamma_{S,\uparrow} + \Gamma_{S,\downarrow})$ is the injection efficiency into $|\downarrow\rangle$, and $\Gamma_{D,\downarrow}$ is the tunnel rate from $|\downarrow\rangle$ to the drain (see Fig. 4.3c-d). The saturation rate D is the sum of W, the spin relaxation rate from $|\downarrow\rangle$ to $|\uparrow\rangle$, and $(1-A)\Gamma_{D,\downarrow}$, which accounts for direct tunneling into $|\uparrow\rangle$:

$$D = W + (1-A)\Gamma_{D,\downarrow} \ . \tag{4.3}$$

By measuring $<n_\downarrow>$ for different pulse widths t_h, we can find D and $A\Gamma_{D,\downarrow}$ using Eq. (4.2). Together with the value of A, which can be extracted from large-bias measurements without pulses, we can determine the spin-relaxation rate $W=1/T_1$ via Eq. (4.3).

In Fig. 4.3f we show the average number of tunneling electrons per cycle for the stable current, $<n_\uparrow>$, and for the transient current, $<n_\downarrow>$. Clearly, $<n_\uparrow>$ increases linearly with pulse length, whereas $<n_\downarrow>$ saturates, as expected. From fitting $<n_\downarrow>$ to Eq. (4.2) we find $D=(1.5 \pm 0.2)$ MHz and $A\Gamma_{D,\downarrow}=(0.47 \pm 0.09)$ MHz. Furthermore, $A=(0.28 \pm 0.05)$, leading to $(1-A)\Gamma_{D,\downarrow}=(1.2 \pm 0.3)$ MHz and $W=(0.30 \pm 0.35)$ MHz. Averaging over similar measurements, using different tunnel rates and t_l, leads to $W=(0.20 \pm 0.25)$ MHz.

We conclude that the spin relaxation rate ($W<0.5$ MHz) is much smaller than the tunnel rates ($\Gamma_S \gg \Gamma_D \approx 1.6$ MHz). This means that the decay of the transient current is dominated by direct injection into $|\uparrow\rangle$, and therefore the single-step pulse method can only provide a weak lower bound on T_1. To circumvent this, we decouple the read-out stage from the relaxation stage by inserting an extra pulse step. This way, an electron can only tunnel out of the dot *after* the waiting time, enabling us to directly measure the relaxation probabilities as a function of waiting time [2], as explained below.

4.5   Spin relaxation measurement using double-step pulses

The schematic waveform of the double-step pulses is shown in Fig. 4.4a. Applying these pulses results in current traces as in Fig. 4.4b. Figs. 4.4c-e depict the energy levels for the $|\downarrow\rangle$ current peak indicated in Fig. 4.4b at the three different stages of the pulse cycle. First the dot is emptied (Fig. 4.4c). In the second stage (Fig. 4.4d), an electron tunnels into either $|\downarrow\rangle$ or $|\uparrow\rangle$. Again, due to the charging energy only one electron can occupy the dot. The probability that it enters $|\downarrow\rangle$, A, does not depend on the pulse lengths, which are the only parameters we change. If the electron entered $|\downarrow\rangle$, the probability that it has *not* relaxed to $|\uparrow\rangle$ after t_h is $\exp(-t_h/T_1)$ (we assume exponential decay). Finally (Fig. 4.4e), if the electron is in $|\downarrow\rangle$, it can tunnel out, but only to the drain. In contrast, if the electron is in $|\uparrow\rangle$, it can tunnel out to either the source or the drain when the cycle is restarted (Fig. 4.4c). Similarly, electrons entering the dot originate from the source or the drain (Fig. 4.4d). Assuming that Γ_S/Γ_D is constant throughout the cycle, the average current generated by electrons leaving the dot during the "low" phase of the pulse train (Fig. 4.4c) is zero. Therefore the current only consists of electrons that entered $|\downarrow\rangle$ and have not relaxed during t_h:

$$I = e f_{rep} <n_\downarrow> = e f_{rep} C A \, e^{(-t_h/T_1)}, \tag{4.4}$$

where f_{rep} is the pulse repetition frequency and C a constant accounting for the tunnel probability in the read-out stage. We determine $<n_\downarrow>$ for different t_h. Normalized to the value for $t_h=0$, it is a direct measure of spin relaxation:

$$\frac{<n_\downarrow>_{t_h=t}}{<n_\downarrow>_{t_h=0}} = \frac{C A \, e^{(-t/T_1)}}{C A \, e^{(-0/T_1)}} = \frac{P_\downarrow(t)}{P_\downarrow(0)} = e^{(-t/T_1)} \; . \tag{4.5}$$

To be able to extract reliable peak heights from the very small currents, we average over many traces. Examples of averaged curves are shown in Fig. 4.4f for $t_h=1$, 2.5 and 4 μs. In Fig. 4.4g, data extracted from these and similar curves are plotted as a function of t_h, up to 7.5 μs. Longer waiting times result in unmeasurably small currents ($I \propto 1/t_h$). The two data sets shown were taken with different gate settings (and thus different tunnel rates) and different t_m. As a guide to the eye, lines corresponding to an exponential decay with decay times $\tau = 10\,\mu$s, $\tau = 30\,\mu$s and $\tau = \infty$ are included. There is no clear decay visible. We fit the data in Fig. 4.4g and similar data, and average the resulting relaxation rates. From an error analysis we find a lower bound of $T_1 > 50\,\mu$s. We emphasize
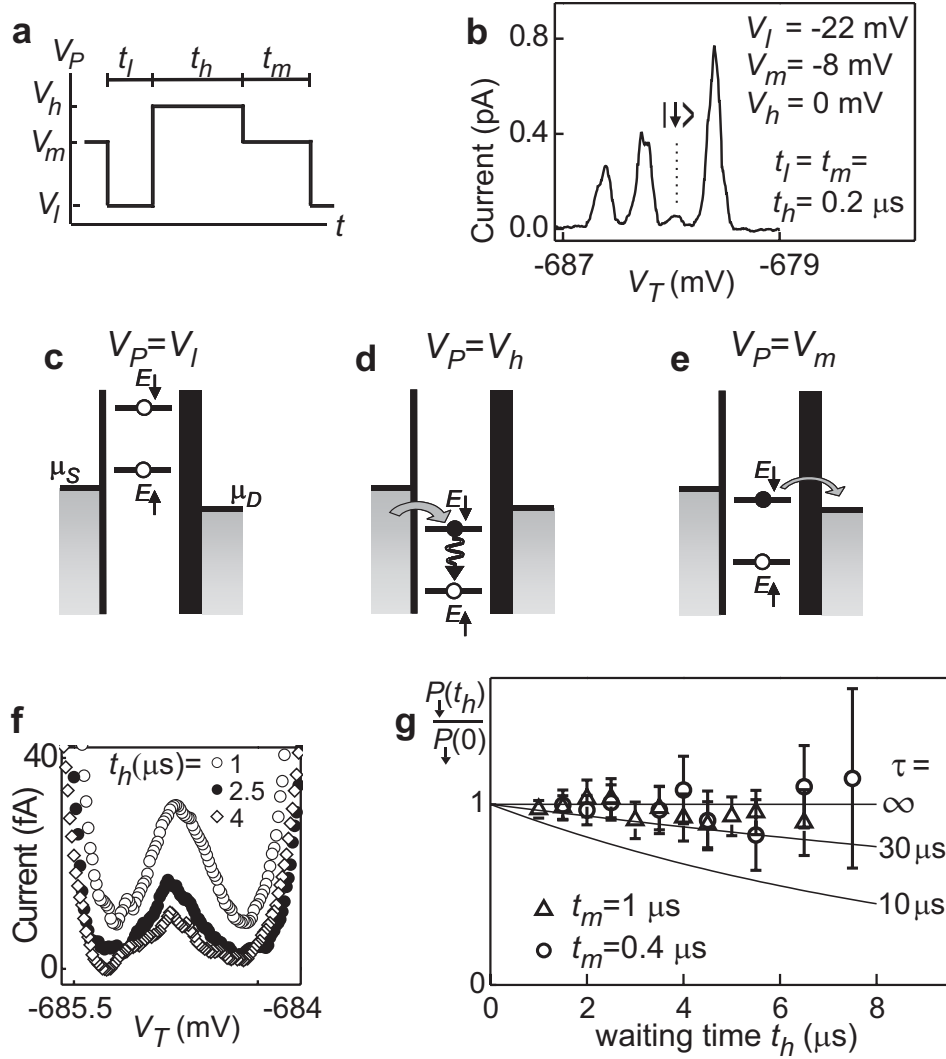
Figure 4.4: One-electron spin relaxation studied using double-step pulses at 7.5T. **(a)** Schematic waveform of the pulse train (rise/fall time of 1.5 ns). **(b)** Typical pulse-excited current trace. The three main peaks correspond to a stable current flowing via $|\uparrow\rangle$ when $|\uparrow\rangle$ is in the bias window during one of the three stages of the waveform. The small peak is due to transient current via $|\downarrow\rangle$ for $V_P = V_m$ [28]. **(c)**-**(e)** Diagrams depicting the energy levels during the three stages of the pulse for the $|\downarrow\rangle$-peak shown in (b). **(c)** The dot is emptied during a time t_l. **(d)** Both $|\uparrow\rangle$ and $|\downarrow\rangle$ lie below the electrochemical potentials of the leads and an electron can tunnel into the $|\downarrow\rangle$; other possible tunnel processes are not indicated since they do not contribute to the current (see text). We allow the electron to relax for a time t_h. **(e)** Now $|\downarrow\rangle$ lies in the bias window. Only if the electron has spin-down it can tunnel out and contribute to current. **(f)** Averaged $|\downarrow\rangle$ current peaks for t_h=1, 2.5 and 4 μs with t_m=0.4 μs (for data in (f) and (g) t_l=t_h). **(g)** The probability $P_\downarrow(t_h)/P_\downarrow(0)$ that the spin did *not* decay during the waiting time t_h.

that, since we do not observe a clear signature of relaxation in our experimental time window, T_1 might actually be much longer.

4.6   Back-action of the QPC

The lower bound we find for T_1 is much longer than the time needed for read-out of the quantum bit using proposed spin-to-charge conversion schemes [25]. In these schemes, spin-dependent tunneling events correlate the charge on the dot to the initial spin state. A subsequent charge measurement thus reveals information on the spin. This can de done in our device using the QPC located next to the QD (see Fig. 4.1a) [10].

An interesting question is how much the stability of the spin states is affected by such charge measurements. We have studied this by sending a large current through the QPC, set at maximum charge sensitivity, and repeating the T_1 measurements. The drain lead is shared by the QPC- and the QD-current, which causes some peak broadening and limits the experimental window. However, even for a very large current of $\sim$20 nA through the QPC ($\mu_Q - \mu_D = 500\,\mu eV$), we still do not find a measurable decay of the spin. For comparison, we can measure the charge on the QD within 50 μs using a QPC current of only 10 nA [29]. Taking these measurements together shows that, by using spin-to-charge conversion, it should be possible to perform single-shot spin readout in this device. In chapter 7 we will proceed on this path.

References

[1] A.V. Khaetskii and Y.V. Nazarov, Phys. Rev. B **61**, 12639 (2000).

[2] T. Fujisawa *et al.*, Nature (London) **419**, 278 (2002).

[3] S.I. Erlingsson and Y.V. Nazarov, Phys. Rev. B **66**, 155327 (2002).

[4] A.V. Khaetskii and Y.V. Nazarov, Phys. Rev. B **64**, 125316 (2001).

[5] S. Cortez *et al.*, Phys. Rev. Lett. **89**, 207401 (2002).

[6] M. Paillard *et al.*, Phys. Rev. Lett. **86**, 1634 (2001).

[7] For a review on few-electron vertical QDs, see L.P. Kouwenhoven, D.G. Austing, and S. Tarucha, Rep. Prog. Phys. **64** (6), 701 (2001).

[8] S. Sasaki, D.G. Austing and S. Tarucha, Physica B **256**, 157-160 (1998); J.Könemann, P.König, R.J.Haug, Physica E **13**, 675 (2002).

[9] M. Ciorga *et al.* , Phys. Rev. B **61**, R16315 (2000).

[10] J.M. Elzerman *et al.*, Phys. Rev. B. **67**, 161308(R) (2003).

[11] J.M. Kikkawa and D.D. Awschalom, Phys. Rev. Lett. **80**, 4313 (1998).

[12] Y. Ohno *et al.*, Phys. Rev. Lett. **83**, 4196 (1999).

[13] For clarity, we have hidden the surface gates that are not used in the experiments. The complete gate structure can be found in Ref. [10].

[14] M. Field *et al.*, Phys. Rev. Lett. **70**, 1311 (1993).

[15] D. Sprinzak, Y. Ji, M. Heiblum, D. Mahalu, and H. Shtrikman, Phys. Rev. Lett. **88**, 176805 (2002).

[16] J. Weis *et al.*, Surface Science 305, 664 (1994).

[17] Similar values for $|g|$ below 9 T are reported by R.M. Potok *et al.*, Phys. Rev. Lett. **91**, 016802 (2003).

[18] T. Fujisawa, Y. Tokura and Y. Hirayama, Physica B **298**, 573-579 (2001).

[19] M. Dobers, K. v. Klitzing and G. Weimann, Phys. Rev. B **38**, 5453 (1988).

[20] M.J. Snelling *et al.*, Phys. Rev. B **44**, 11345 (1991).

[21] G. Salis *et al.*, Nature (London) **414**, 619 (2001).

[22] See, e.g., *Optical Orientation*, edited by F. Meier and B.P. Zakharchenya (North-Holland, 1984).

[23] V. I. Fal'ko, B. L. Altschuler and O. Tsyplyatev, cond-mat/0501046 (2005).

[24] D. Loss and D.P. DiVincenzo, Phys. Rev. A **57**, 120 (1998).

[25] L.M.K. Vandersypen *et al.*, in *Quantum Computing and Quantum Bits in Mesoscopic Systems* (Kluwer Academic, New York, 2003); quant-ph/0207059.

[26] The condition $\Gamma_S \gg \Gamma_D$ is easily achieved by tuning the different gate voltages.

[27] T. Fujisawa, Y. Tokura and Y. Hirayama, Phys. Rev. B **63**, R081304 (2001).

[28] The $|\downarrow\rangle$ peak for V_h appears at the same voltage on T as the $|\uparrow\rangle$ peak belonging to V_m.

[29] L.M.K. Vandersypen *et al.*, Appl. Phys. Lett. **85**, 4394 (2004).

Chapter 5

Few-electron quantum dot operated as a bipolar spin filter

R. Hanson, L.M.K. Vandersypen, L.H. Willems van Beveren,
J.M. Elzerman, I.T. Vink, L.P. Kouwenhoven

In this chapter, we demonstrate spin filtering in a few-electron quantum dot. In a large in-plane magnetic field, we observe the Zeeman splitting of the two-electron spin triplet states. Also, the one-electron Zeeman splitting is clearly resolved at both the zero-to-one and the one-to-two electron transition. Since the spin of the electrons transmitted through the dot is opposite at these two transitions, this device can be employed as an electrically tunable, bipolar spin filter. Calculations and measurements show that higher-order tunnel processes and spin-orbit interaction have a negligible effect on the polarization.

5.1   Quantum dot as a bipolar spin filter

The spin degree of freedom of electrons has great potential as a carrier of classical information (spintronics) [1] and quantum information (spin quantum bits) [2]. Spintronics requires a device that can filter electrons by their spin orientation, i.e. a spin filter. As for quantum information, spin filters can be used for initialization and read-out of spin quantum bits [2, 3]. Moreover, they are an important ingredient of recent proposals to measure Bell's inequalities with entangled electron spins [4].

Much experimental progress has been made using magnetic semiconductors as spin filters [5]. However, many recent proposals focus on spin filtering in a two-dimensional electron gas (2DEG) [6, 7], since this allows easy integration with other devices such as electron spin entanglers [4]. Spin-dependent electron transport through a 2DEG with giant Zeeman splitting of the lowest 2D subband was recently measured [8]. Also, quantum dots formed within 2DEGs have been shown to act as spin filters, by utilizing universal conductance fluctuations controlled by gate voltages [9], and via spin-dependent coupling to the leads in a perpendicular magnetic field [10]. In the former case, the filtering efficiency (up to 70% in Ref. [9]) and polarity rely on the chaotic character of the dot. In the latter case, the formation of edge channels in the leads yields reproducible spin-selectivity with a high efficiency, but the polarization always corresponds to the ground state spin-orientation in the leads, and therefore the filter cannot be bipolar. The same is true for quantum point contacts, which have been used as unipolar spin filters [9, 11]. For most purposes, however, a filter is required which is both bipolar and has a very high efficiency.

Recher *et al.* [6] proposed to employ the discrete spin-resolved energy levels of a quantum dot for spin filtering in a 2DEG. The low-bias electron transport through such a dot will be almost completely polarized if the Zeeman energy is much larger than the thermal energy. Furthermore, for simple pair-wise spin filling of orbital states, the polarization is opposite at any two transitions with successive electron number. The filter polarity can thus easily be reversed by changing gate voltages.

This spin filter has not been realized experimentally. The challenge is to demonstrate spin-splitting of orbital levels in a quantum dot for successive electron transitions, and to show that electrons transported at these transitions carry opposite spin. Direct measurement of the Zeeman splitting of the orbital states at the 0↔1 electron transition was reported by two groups recently [12, 13]. In dots containing more than one electron, Zeeman energy has, up to now, only been observed indirectly, by comparing the energy shifts of the ground state induced

by a magnetic field for successive electron numbers [14].

In this work, we study the spin states of a one- and two-electron quantum dot directly, by applying a large magnetic field in the plane of the 2DEG. This field induces a large Zeeman splitting, but has a negligible effect on the orbitals in the dot. Due to the small size of the dot, the exact number of electrons is known and the orbital energy levels are well separated. Thus, we can unambiguously identify both the orbital and the spin part of the electron wave functions. Our measurements clearly show Zeeman splitting of the two-electron triplet states. Furthermore, we observe the single-electron Zeeman splitting at the 0↔1 electron transition as well as at the 1↔2 transition. Since the two-electron ground state is a spin-singlet, this implies that the spin orientation of transmitted electrons is opposite at these two transitions. Thus, our measurements constitute the demonstration of the spin filter proposed by Recher *et al.* The influence of higher-order tunneling and spin-orbit interaction on the filter efficiency is discussed and estimated both from calculations and measurements.

The quantum dot is defined in a GaAs/AlGaAs heterostructure, containing a 2DEG 90 nm below the surface with an electron density $n_s = 2.9 \times 10^{11}$ cm^{-2}. The measurements are performed in a dilution refrigerator at base temperature T = 20 mK with a magnetic field $B_{//}$ applied in the plane of the 2DEG. The same device was used in previous experiments on a one-electron dot [12]. The results presented here were reproduced with a similar device fabricated on a wafer with a 2DEG 60nm below the surface.

5.2   Filtering spin-up electrons

We first consider electron transport through the dot at the 0↔1 electron transition and show that current through the ground state is spin-polarized for $B_{//} \neq 0$. Since the energy separation of the orbital levels ($\Delta E_{orb} \approx 1.1$ meV) in this device is larger than the largest source-drain bias, eV_{SD}, applied in the experiments, the one-electron orbital excited states are ignored. The orbital ground state is spin-degenerate at $B_{//} = 0$. In a finite magnetic field, the two spin states, parallel (↑, or spin-up) and anti-parallel (↓, or spin-down) to the applied field, acquire a different Zeeman energy and the orbital ground state splits: $E_\downarrow = E_\uparrow + \Delta E_Z$, with $\Delta E_Z = g\mu_B B_{//}$.

Electron transport through the dot is governed by the electrochemical potential μ. Consider a transition between two states of the dot, state $|a\rangle$ with N electrons and $|b\rangle$ with N+1 electrons. The corresponding electrochemical potential $\mu_{a \leftrightarrow b}$ is given by the difference between the total energy of the dot in state $|a\rangle$
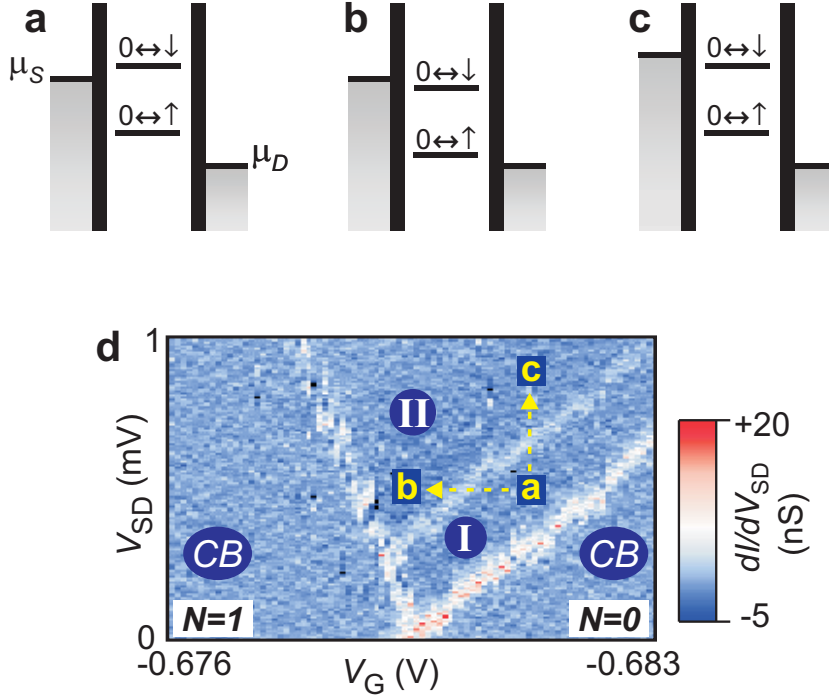
Figure 5.1: **(a)-(c)** Energy diagrams showing **(a)** spin filtering at the $0\leftrightarrow 1$ electron transition, which can be lifted by either **(b)** changing the gate voltage, V_G, or **(c)** increasing the source-drain bias, $V_{SD} = (\mu_S - \mu_D)/e$. **(d)** dI/dV_{SD} as a function of V_G and V_{SD} around the $0\leftrightarrow 1$ electron transition at $B_{//} = 12$ T [16]. In the entire region I the dot acts as a spin filter, allowing only spin-up electrons to flow through the dot. Letters a-c indicate the level positions depicted by the diagrams in (a)-(c).

and in state $|b\rangle$: $\mu_{a\leftrightarrow b} = U(b) - U(a)$. Choosing the zero of energy conveniently, this gives $\mu_{0\leftrightarrow\uparrow} = E_\uparrow$ and $\mu_{0\leftrightarrow\downarrow} = E_\downarrow = E_\uparrow + \Delta E_Z$ for the $0\leftrightarrow 1$ electron transitions.

The ladder of electrochemical potentials in the dot can be shifted relative to the electrochemical potentials of the source (μ_S) and the drain (μ_D), by changing the gate voltage V_G: $\Delta\mu \propto \Delta V_G$ [15]. Since the electrochemical potentials all depend in the same way on V_G, the *relative* positions of the electrochemical potentials are independent of V_G. Thus, by tuning V_G, we can selectively position $\mu_{0\leftrightarrow\uparrow}$ in the bias window (i.e. $\mu_S > \mu_{0\leftrightarrow\uparrow} > \mu_D$), allowing transport of electrons through the dot via the ground state $|\uparrow\rangle$ only. This situation is depicted in Fig. 5.1a. Since only electrons with spin-up can enter the dot, the dot acts here as a spin filter. If the levels are pulled down by a change in V_G (Fig. 5.1b), or if the source-drain bias is increased (Fig. 5.1c), transport through the spin-excited state $|\downarrow\rangle$ becomes possible as well and the current is no longer spin-polarized. Thus, in an energy window set by the Zeeman splitting, the current through the device is carried, to first order, only by spin-up electrons, even though the

leads are not spin-polarized. The influence of higher-order tunnel processes and spin-orbit interaction on the spin polarization is discussed below.

Fig. 5.1d shows the differential conductance dI/dV_{SD} around the 0↔1 electron transition at $B_{//} = 12$ T. The lines of high dI/dV_{SD} define four regions. In the regions indicated by CB, Coulomb blockade prohibits first-order tunneling and the number of electrons on the dot, N, is stable. Coulomb blockade is lifted whenever $\mu_{0\leftrightarrow\uparrow}$ is in the bias window, defining the V-shaped area of transport. The Zeeman splitting between $|\uparrow\rangle$ and $|\downarrow\rangle$ is clearly resolved ($\Delta E_Z \approx 240\ \mu$eV), allowing us to identify the region where only spin-up electrons can enter the dot (region I). In region II both spin-up and spin-down electrons can pass through the dot. Thus, for all combinations of V_G and V_{SD} within region I, the dot acts as a spin filter transmitting, to first order, only spin-up electrons.

5.3 Filtering spin-down electrons

Now we analyze the current at the 1↔2 electron transition and show that in this case the dot filters the *opposite* spin. The ground state of a two-electron dot in zero magnetic field is always a spin-singlet (total spin quantum number $S = 0$) [17], formed by the two electrons occupying the lowest orbital with their spins anti-parallel: $|S\rangle = (|\uparrow\downarrow\rangle - |\downarrow\uparrow\rangle)/\sqrt{2}$. The first excited states are the spin-triplets ($S = 1$), where the antisymmetry of the two-electron wave function requires one electron to occupy a higher orbital. The three triplet states are degenerate at zero magnetic field, but acquire different Zeeman energy shifts E_Z in finite magnetic fields because their spin z-components (quantum number m_S) differ: $m_S = +1$ for $|T_+\rangle = |\uparrow\uparrow\rangle$, $m_S = 0$ for $|T_0\rangle = (|\uparrow\downarrow\rangle + |\downarrow\uparrow\rangle)/\sqrt{2}$ and $m_S = -1$ for $|T_-\rangle = |\downarrow\downarrow\rangle$.

The energies of the states can be expressed in terms of the single-particle energies of the two electrons plus a charging energy E_C which accounts for the Coulomb interactions:

$$\begin{aligned}
E_S &= E_\uparrow + E_\downarrow + E_C = 2E_\uparrow + \Delta E_Z + E_C \\
E_{T_+} &= 2E_\uparrow + E_{ST} + E_C \\
E_{T_0} &= E_\uparrow + E_\downarrow + E_{ST} + E_C = 2E_\uparrow + E_{ST} + \Delta E_Z + E_C \\
E_{T_-} &= 2E_\downarrow + E_{ST} + E_C = 2E_\uparrow + E_{ST} + 2\Delta E_Z + E_C,
\end{aligned}$$

with E_{ST} denoting the singlet-triplet energy difference in the absence of the Zeeman splitting ΔE_Z. E_{ST} is considerably smaller than the single-particle level spacing ΔE_{orb}, because the occupation of different orbitals and exchange interaction reduce the Coulomb energy for the triplet states [15].
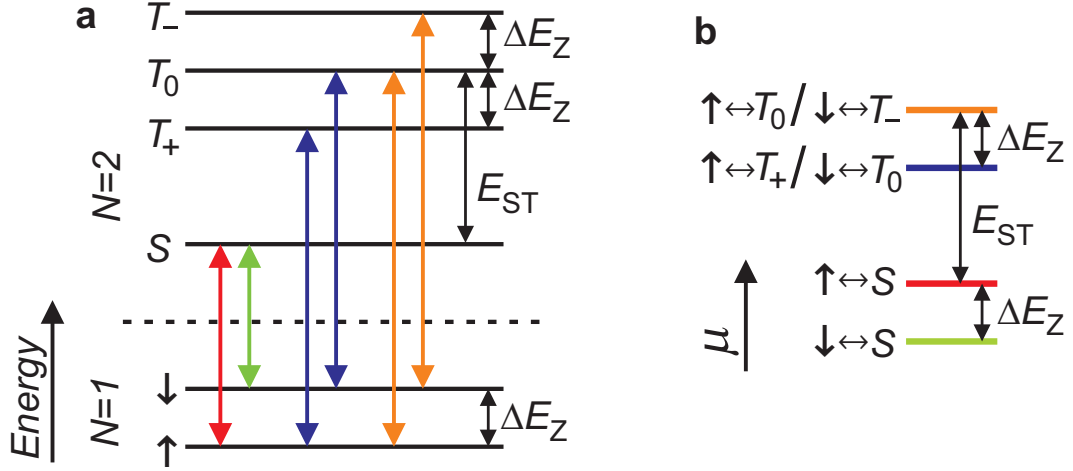
Figure 5.2: (a) Energy diagram schematically showing the energy levels of the one- and two-electron states. The allowed transitions between these levels are indicated by arrows. **(b)** Electrochemical potential ladder corresponding to the transitions shown in (a), using the same color coding. Changing the gate voltage shifts the ladder as a whole. Note that the three triplet states appear at only two values of the electrochemical potential.

Fig. 5.2a shows the possible transitions between the one-electron spin-split orbital ground state and the two-electron states. We have omitted the transitions $\uparrow \leftrightarrow T_-$ and $\downarrow \leftrightarrow T_+$, since these require a change in the spin z-component of more than $\frac{1}{2}$ and are thus spin-blocked [18]. From the energy diagram we can deduce the electrochemical potential ladder, which is shown in Fig. 5.2b. Note that $\mu_{\uparrow \leftrightarrow T_+} = \mu_{\downarrow \leftrightarrow T_0}$ and $\mu_{\uparrow \leftrightarrow T_0} = \mu_{\downarrow \leftrightarrow T_-}$. Consequently, the *three* triplet states change the first-order transport through the dot at only *two* values of V_{SD}. The reason is that the first-order transport probes the energy difference between states with *successive* electron number. In contrast, the onset of second-order (cotunneling) currents is governed by the energy difference between states with the *same* number of electrons. Therefore, the triplet states change the second-order (cotunneling) currents at three values of V_{SD}. In our measurements, these cotunneling currents were too small to detect (see below).

In Fig. 5.3a we map out the positions of the electrochemical potentials as a function of V_G and V_{SD}. For each transition, the two lines originating at $V_{SD} = 0$ span a V-shaped region where the corresponding electrochemical potential is in the bias window [16]. In the region labeled A, only transitions between the one-electron ground state, $|\uparrow\rangle$, and the two-electron ground state, $|S\rangle$, are possible, since only $\mu_{\uparrow \leftrightarrow S}$ is positioned inside the bias window. Since this transition corresponds to transport of spin-down electrons *only*, the dot again acts as a spin
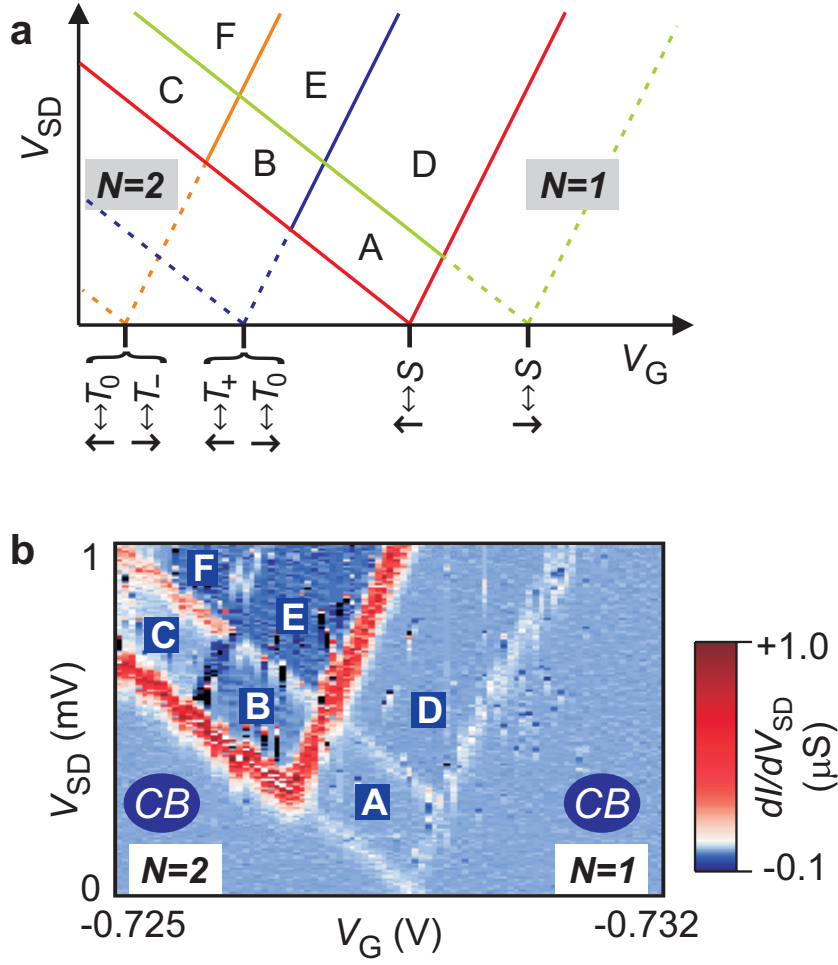
Figure 5.3: (a) Energetically allowed 1↔2 electron transitions as a function of V_{SD} and V_G. The lines corresponding to ↑↔ S outline the region of transport; outside this region, where lines are dashed, the dot is in Coulomb blockade. (b) dI/dV_{SD} as a function of V_G and V_{SD} around the 1↔2 electron transition at $B_{//} = 12$ T. In the region labeled A only spin-down electrons pass through the dot.

filter, but with a polarization opposite to the 0↔1 electron case. The polarization of the current is lost when $\mu_{\downarrow\leftrightarrow S}$ or $\mu_{\uparrow\leftrightarrow T_+}$ enters the bias window (regions D an B respectively). In the regions C, E and F several more transitions are possible which leads to a more complex, but still understandable behavior of the current. Outside the V-shaped region spanned by the ground state transition $\mu_{\uparrow\leftrightarrow S}$, Coulomb blockade prohibits first order electron transport.

The experimental data, shown in Fig. 5.3b, is in excellent agreement with the predictions of Fig. 5.3a. Three important observations can be made. First, we clearly observe the Zeeman splitting of the triplet states. Second, the transitions

between the one-electron states and the two-electron singlet ground state are spin-resolved. Thus, we can easily identify the region where the current is carried by spin-down electrons only, i.e. region A. The size of this region is determined by the Zeeman energy ($\Delta E_Z \approx 240\,\mu$eV) and the singlet-triplet energy difference ($E_{ST} \approx 520\,\mu$eV). The third observation is that the Zeeman energy, and therefore the g-factor, is the same for the one-electron states as for the two-electron states, within measurement accuracy ($\approx 5\%$). We note that the large variation in differential conductance observed in Fig. 5.3b, can be completely explained by a sequential tunneling model with spin- and orbital-dependent tunnel rates [19].

To achieve spin-down filtering at the 1↔2 electron transition, it is crucial that the two-electron ground state is a spin-singlet. Indeed, in case of a triplet ground state, the dot would transmit only spin-up electrons. We made sure that the ground state of the two-electron dot at $B_{//} = 12$ T is still a spin-singlet state by carefully monitoring the energies of the two-electron states from zero field, where the ground state is always a spin-singlet [17]. Additionally, the line of high dI/dV_{SD} separating region A from D would not be present in case the ground state would be a spin triplet. (This can be seen by redrawing the diagram in Fig. 5.3a for the case of a triplet ground state).

The data presented in Figs. 5.1d and 5.3b shows that our device can be operated as a bipolar spin filter, as proposed by Recher *et al.* Switching between the 0↔1 electron transition, where the polarization is spin-up, and the 1↔2 electron transition, where the polarization is spin-down, only requires adjusting the gate voltages, which can already be done on a subnanosecond timescale [12].

5.4   Efficiency of the spin filter

In a sequential tunneling picture, the polarization of the first-order tunnel current is, due to energy conservation, $\approx 100\%$ whenever $\Delta E_Z \gg kT$ (which is easily fulfilled here). We now investigate the influence of tunneling via virtual higher-energy states (second-order tunneling or cotunneling) [20] and of spin-orbit coupling on the filter efficiency.

We first note that the cotunneling current $I_{cot} \propto \Gamma^2$, whereas the first-order tunneling current $\propto \Gamma$ and therefore cotunneling can always be suppressed by making the tunnel rates small. We obtain an upper bound on the cotunneling current by measuring the current in the Coulomb blockade region close to the spin filter region. Here, the parameters for cotunneling are the same as those in the spin filter region, but first-order tunneling is forbidden, allowing a direct measurement of I_{cot}. We find that for both the 0↔1 and the 1↔2 electron

transition, I_{cot} is smaller than the noise floor of our measurement (10^{-14} A).

Using values for the tunnel rates obtained from first-order tunneling, we can also calculate I_{cot} in the spin filter regions. For $V_{SD} < \Delta E_Z$, only elastic cotunneling is possible [20]. At the 0↔1 electron transition, we find that I_{cot} is $\sim 10^{-19}$A in the middle of region I, whereas the sequential spin-up current is $\sim 10^{-13}$A. At the 1↔2 electron transition, $I_{cot} \sim 10^{-15}$A in the middle of region A. With $\mu_{\uparrow \leftrightarrow T_+}$ far above μ_S, this reduces to 10^{-16}A, which is more than three orders of magnitude smaller than the sequential spin-down current ($\approx 3 \cdot 10^{-13}$A). Thus, both the measurements and the calculations show that second-order tunneling processes are negligible.

Due to spin-orbit coupling the eigenstates in the dot are not the pure spin states $|\uparrow\rangle$ and $|\downarrow\rangle$, but each contains a small admixture of the opposite spin, which limits the efficiency of the spin filter in the ($\uparrow,\downarrow$) basis. An upper bound on the spin-orbit coupling can be derived from the spin-orbit mediated spin relaxation. The very low spin relaxation rates measured in our device, 2 MHz at 10 T and 9 MHz at 14 T [12, 21], indicate that the reduction in efficiency is less than 10^{-4} [22]. We further note that the tunnel barriers are purely electrostatically defined and should therefore not induce extra spin relaxation.

Future experiments will focus on measurement of the spin-polarization of the current flowing out of the dot by an external analyzer. This can be done for instance by focussing the current onto a quantum point contact [9], although this technique has only allowed polarizations up to 70% to be measured. Alternatively, we plan to investigate the filter properties by placing two dots in series [23], such that the polarization configuration can be switched controllably between parallel and antiparallel.

References

[1] S.A. Wolf, D.D. Awschalom, R.A. Buhrman, J.M. Daughton, S. von Molnr, M. L. Roukes, A.Y. Chtchelkanova and D.M. Treger, Science **294**, 1488 (2001).

[2] D. Loss and D.P. DiVincenzo, Phys. Rev. A **57**, 120 (1998).

[3] L.M.K. Vandersypen, R. Hanson, L.H. Willems van Beveren, J.M. Elzerman, J.S. Greidanus, S. De Franceschi and L.P. Kouwenhoven, in *Quantum*

Computing and Quantum Bits in Mesoscopic Systems (Kluwer Academic, New York, 2003), quant-ph/0207059.

[4] See e.g. D.S. Saraga and D. Loss, Phys. Rev. Lett. **90**, 166803 (2003), and references therein.

[5] R. Fiederling, M. Keim, G. Reuscher, W. Ossau, G. Schmidt, A. Waag and L. W. Molenkamp, Nature (London) **402**, 787 (1999); Y. Ohno, D. K. Young, B. Beschoten, F. Matsukura, H. Ohno and D. D. Awschalom, *ibid.* **402**, 790 (1999).

[6] P. Recher, E.V. Sukhorukov and D. Loss, Phys. Rev. Lett. **85**, 1962 (2000).

[7] E.R. Mucciolo, C. Chamon and C.M. Marcus, Phys. Rev. Lett. **89**, 146802 (2002); Q. Sun, H. Guo and J. Wang, *ibid.* **90**, 258301 (2003); P. Zhang, Q.-K. Xue and X.C. Xie, *ibid.* **91**, 196602 (2003).

[8] A. Slobodskyy, C. Gould, T. Slobodskyy, C. R. Becker, G. Schmidt and L. W. Molenkamp , Phys. Rev. Lett. **90**, 246601 (2003).

[9] J.A. Folk, R. M. Potok, C. M. Marcus and V. Umansky, Science **299**, 679 (2003).

[10] M. Ciorga, M. Pioro-Ladriere, P. Zawadzki, P. Hawrylak and A. S. Sachrajda , Appl. Phys. Lett. **80**, 2177 (2002).

[11] R.M. Potok, J.A. Folk, C.M. Marcus and V.Umansky, Phys. Rev. Lett. **89**, 266602 (2002).

[12] R. Hanson, B. Witkamp, L. M. K. Vandersypen, L. H. Willems van Beveren, J. M. Elzerman and L. P. Kouwenhoven, Phys. Rev. Lett. **91**, 196802 (2003).

[13] R.M. Potok, J.A. Folk, C.M. Marcus, V. Umansky, M. Hanson and A. C. Gossard, Phys. Rev. Lett. **91**, 016802 (2003).

[14] J. Weis, R.J. Haug, K. v. Klitzing and K. Ploog, Phys. Rev. Lett. **71**, 4019 (1993); S. Sasaki, D.G. Austing and S. Tarucha, Physica B **256**, 157-160 (1998).

[15] L.P. Kouwenhoven, D.G. Austing, and S. Tarucha, Rep. Prog. Phys. **64** (6), 701 (2001).

[16] We apply the source-drain bias asymmetrically; the drain is connected to ground in the *I-V* converter. The skewness of the V-shaped transport region is determined by the ratio of the capacitances of the dot to the source, C_S, and to the drain, C_D. For $C_S = C_D$, the V-shape is symmetric.

[17] *Solid State Physics*, N.W. Ashcroft and N.D. Mermin (Saunders, New York, 1974).

[18] D. Weinmann, W. Häusler and B. Kramer, Phys. Rev. Lett. **74**, 984 (1995).

[19] R. Hanson, I.T. Vink, D.P. DiVincenzo, L.M.K. Vandersypen, J.M. Elzer-man, L.H. Willems van Beveren and L.P. Kouwenhoven., to be published in the Proceedings of the XXXIXth Rencontres de Moriond (La Thuile, 2004) "Quantum information and decoherence in nanosystems"; cond-mat/0407793.

[20] D.V. Averin and Y.V. Nazarov, Phys. Rev. Lett. **65**, 2446 (1990).

[21] J.M. Elzerman, R. Hanson, L.H. Willems van Beveren, B. Witkamp, L.M.K. Vandersypen and L.P. Kouwenhoven, Nature **430**, 431 (2004).

[22] V.N. Golovach, A. Khaetskii and D. Loss, Phys. Rev. Lett. **93**, 016601 (2004).

[23] K. Ono, D. G. Austing, Y. Tokura and S. Tarucha, Science **297**, 1313 (2002).

Chapter 6

Excited-state spectroscopy on a nearly closed quantum dot via charge detection

J. M. Elzerman, R. Hanson, L. H. Willems van Beveren,
L. M. K. Vandersypen and L. P. Kouwenhoven

In this chapter, we demonstrate a method for measuring the discrete energy spectrum of a quantum dot connected very weakly to a single lead. A train of voltage pulses applied to a metal gate induces tunneling of electrons between the quantum dot and a reservoir. The effective tunnel rate depends on the number and nature of the energy levels in the dot made accessible by the pulse. Measurement of the charge dynamics thus reveals the energy spectrum of the dot, as demonstrated for a dot in the few-electron regime.

6.1   Introduction

Few-electron quantum dots are considered as qubits for quantum circuits, where the quantum bit is stored in the spin or orbital state of an electron in a single or double dot. The elements in such a device must have functionalities such as initialization, one- and two-qubit operations and read-out [1]. For all these functions it is necessary to have precise knowledge of the qubit energy levels. Standard spectroscopy experiments involve electron transport through the quantum dot while varying both a gate voltage and the source-drain voltage [2]. This requires that the quantum dot be connected to two leads with a tunnel coupling large enough to obtain a measurable current [3].

Coupling to the leads unavoidably introduces decoherence of the qubit: even if the number of electrons on the dot is fixed due to Coulomb blockade, an electron can tunnel out of the dot and be replaced by another electron through a second-order tunneling process, causing the quantum information to be irretrievably lost. Therefore, to optimally store qubits in quantum dots, higher-order tunneling has to be suppressed, i.e. the coupling to the leads must be made as small as possible. Furthermore, real-time observation of electron tunneling, important for single-shot read-out of spin qubits via spin-to-charge conversion, also requires a small coupling of the dot to the leads. In this regime, current through the dot would be very hard or even impossible to measure. Therefore an alternative spectroscopic technique is needed, which does not rely on electron transport through the quantum dot.

Here we present spectroscopy measurements using charge detection. Our method resembles experiments on superconducting Cooper-pair boxes and semiconductor disks which have only one tunnel junction so that no net current can flow. Information on the energy spectrum can then be obtained by measuring the energy for adding an electron or Cooper-pair to the box, using a single-electron transistor (SET) operated as a charge detector [4, 5, 6]. We are interested in the excitation spectrum for a given number of electrons on the box, rather than the addition spectra. We use a quantum point contact (QPC) as an electrometer [7] and excitation pulses with repetition rates comparable to the tunnel rates to the lead, to measure the discrete energy spectrum of a nearly isolated one- and two-electron quantum dot.

6.2   Tuning the tunnel barriers

The quantum dot and QPC are defined in the two-dimensional electron gas (2DEG) in a $GaAs/Al_{0.27}Ga_{0.73}As$ heterostructure by dc voltages on gates T, M, R
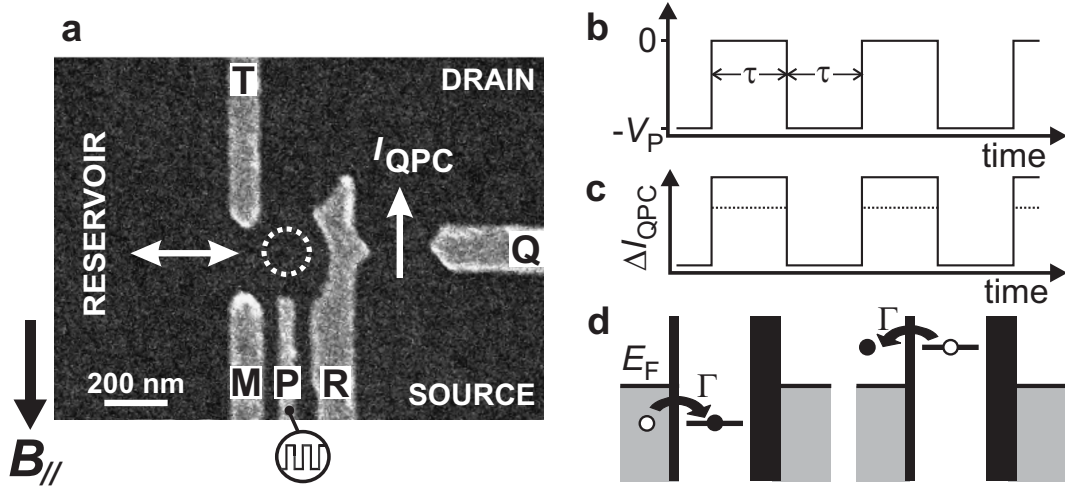
Figure 6.1: QPC response to a pulse train applied to the plunger gate. **(a)** Scanning electron micrograph of a quantum dot and quantum point contact, showing only the gates used in the present experiment (the complete device is described in ref. [11]) and chapter 2. **(b)** Pulse train applied to gate P. **(c)** Schematic response in QPC current, ΔI_{QPC}, when the charge on the dot is unchanged by the pulse (solid line) or increased by one electron charge during the 'high' stage of the pulse (dashed). **(d)** Schematic electrochemical potential diagrams during the high (left) and low (right) pulse stage, when the ground state is pulsed across the Fermi level in the reservoir, E_F.

and Q (Fig. 6.1a). The dot's plunger gate, P, is connected to a coaxial cable, to which we can apply voltage pulses (rise time 1.5 ns). The QPC charge detector is operated at a conductance of about e^2/h with source-drain voltage $V_{SD} = 0.2$ mV. All data are taken with a magnetic field $B_{//} = 10$ T applied in the plane of the 2DEG, at an effective electron temperature of about 300 mK.

We first describe the procedure for setting the gate voltages such that tunneling in and out of the dot take place through one barrier only (i.e. the other is completely closed), and the remaining tunnel rate be well controlled. For gate voltages far away from a charge transition in the quantum dot, a pulse applied to gate P (Fig. 6.1b) modulates the QPC current via the cross-capacitance only (solid trace in Fig. 6.1c). Near a charge transition, the dot can become occupied with an extra electron during the high stage of the pulse (Fig. 6.1d). The extra electron on the dot reduces the current through the QPC. The QPC response to the pulse is thus smaller when tunneling takes place (dotted trace in Fig. 6.1c). We denote the amplitude of the difference between solid and dotted traces as the 'electron response'.

Now, even when tunneling is allowed energetically, the electron response is only non-zero when an electron has sufficient time to actually tunnel into the dot
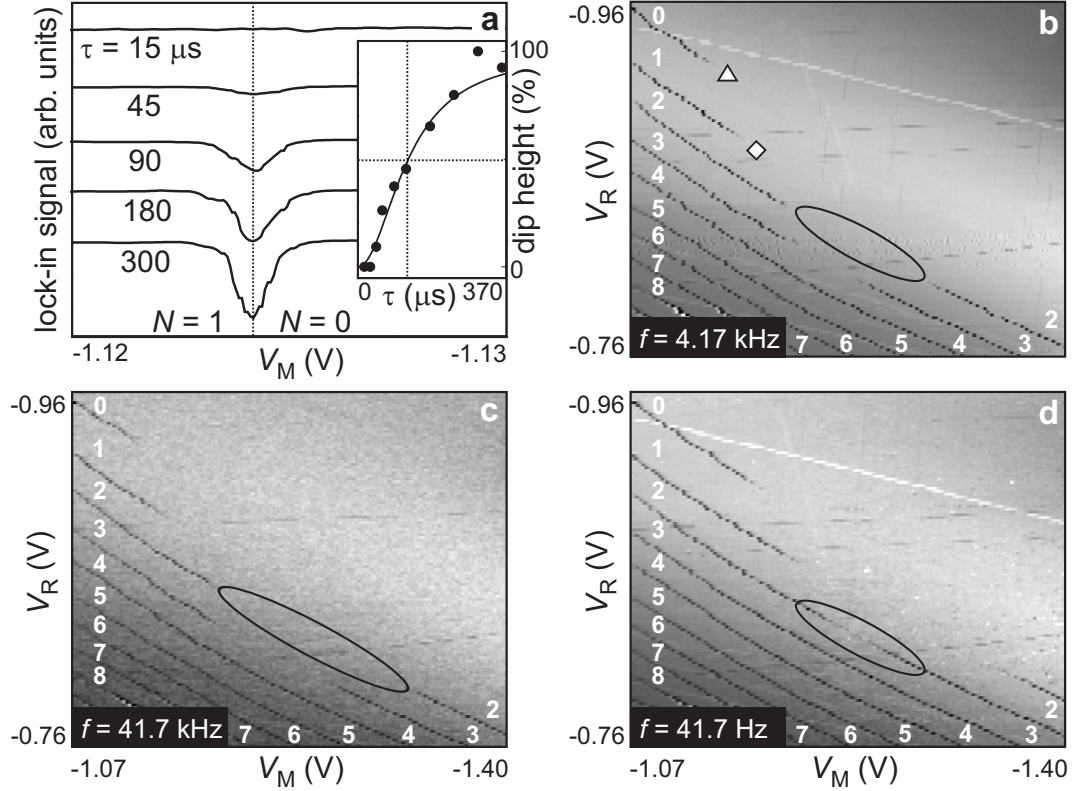
Figure 6.2: Lock-in detection of electron tunneling. **(a)** Lock-in signal at $f = 1/(2\tau)$ versus V_M for different pulse times, τ, with $V_P = 1$ mV. The dip due to the electron response disappears for shorter pulses. (Individual traces have been lined up horizontally to compensate for a fluctuating offset charge, and have been given a vertical offset for clarity.) (Inset) Height of the dip versus τ, as a percentage of the maximum height (obtained at long τ). Circles: experimental data. Dashed lines indicate the pulse time ($\tau \approx 120$ µs) for which the dip size is half its maximum value. Solid line: calculated dip height using $\Gamma = (40 \ \mu s)^{-1}$. **(b)** Lock-in signal in grayscale versus V_M and V_R for $V_P = 1$ mV and $f = 4.17$ kHz. Dark lines correspond to dips as in (a), indicating that the electron number changes by one. White labels indicate the absolute number of electrons on the dot. **(c)** Same plot as in (b), but with larger pulse repetition frequency ($f = 41.7$ kHz). **(d)** Same plot as in (b), but with smaller pulse repetition frequency ($f = 41.7$ Hz).

during the pulse time, τ. By measuring the electron response as a function of τ, we can extract the tunnel rate, Γ, as demonstrated in Fig. 6.2a. We apply a pulse train to gate P with equal up and down times, so the repetition rate is $f = 1/(2\tau)$ (Fig. 6.1b). The QPC response is measured using lock-in detection at frequency f [8], and is plotted versus the dc voltage on gate M. For long pulses (lowest curves) the traces show a dip, which is due to the electron response when crossing

the zero-to-one electron transition. Here, $f \ll \Gamma$ and tunneling occurs quickly on the scale of the pulse duration. For shorter pulses the dip gradually disappears. We find analytically (see Appendix A) that the dip height is proportional to $1 - \pi^2/(\Gamma^2 \tau^2 + \pi^2)$, so the dip height should equal half its maximum value when $\Gamma \tau = \pi$. From the data (inset to Fig. 6.2a), we find that this happens for $\tau \approx 120$ μs, giving $\Gamma \approx (40 \ \mu\text{s})^{-1}$. Using this value for Γ in the analytical expression given above, we obtain the solid line in the inset to Fig. 6.2a, which nicely matches the measured data points.

We explore several charge transitions in Fig. 6.2b, which shows the lock-in signal in grayscale for $\tau = 120$ μs, i.e. $f = 4.17$ kHz. The slanted dark lines correspond to dips as in Fig. 6.2a. From the absence of further charge transitions past the topmost dark line, we obtain the absolute electron number starting from zero. In the top left region of Fig. 6.2b, the right tunnel barrier (between gates R and T) is much more opaque than the left tunnel barrier (between M and T). Here, charge exchange occurs only with the left reservoir (indicated as 'reservoir' in Fig. 6.1a). Conversely, in the lower right region charge is exchanged only with the drain reservoir. In the middle region, indicated for the two-to-three electron transition by an ellipse, both barriers are too opaque and no charge can flow into or out of the dot during the 120 μs pulse; consequently the electron response becomes zero and thus the dark line disappears. For shorter pulses, i.e. larger pulse repetition frequency, the region where the dark line disappears becomes wider (ellipse in Fig. 6.2c). For longer pulses the dark line reappears (Fig. 6.2d). By varying the voltages on gates M and R, we can thus precisely set the tunnel rate to the left or right reservoir for each charge transition.

6.3 Excited-state spectroscopy for $N = 1$

For spectroscopy measurements on a one-electron dot, we set the gate voltages near the zero-to-one electron transition at the point indicated as $\triangle$ in Fig. 6.2b. At this point, the dot is operated as a charge box, with all tunnel events occurring through just a single barrier. The pulse repetition rate is set to 385 Hz, so that the dip height is half its maximum value. The electron response is then very sensitive to changes in the tunnel rate, which occur when an excited state becomes accessible for tunneling.

Fig. 6.3a shows the electron response for a pulse amplitude larger than was used for the data in Fig. 6.2. The dip now exhibits a shoulder on the right side (indicated by 'b'), which we can understand as follows. Starting from the right ($N = 0$), the dip develops as soon as the ground state (GS) is pulsed across the
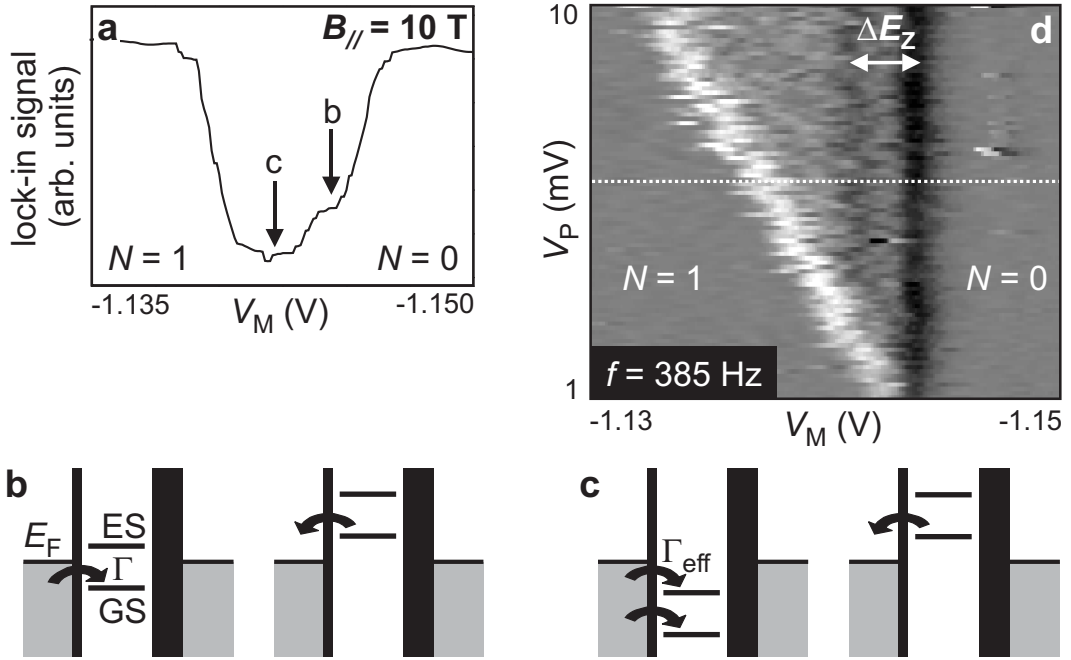
Figure 6.3: Excited-state spectroscopy in a one-electron dot. **(a)** Lock-in signal at $f = 385$ Hz versus V_M, with $V_P = 6$ mV. The dip is half the maximum value (obtained at low f and small V_P) from which we conclude that $\Gamma \approx 2.4$ kHz. **(b)** Schematic electrochemical potential diagrams for the case that only the GS is pulsed across E_F. **(c)** Idem when both the GS and an ES are pulsed across E_F. **(d)** Derivative of the lock-in signal with respect to V_M, plotted as a function of V_M and V_P (individual traces have been lined up to compensate for a fluctuating offset charge). The curve in (a) is taken at the dotted line. The Zeeman energy splitting between the one-electron GS (spin-up) and first ES (spin-down) is indicated by ΔE_Z.

Fermi level E_F and an electron can tunnel into the dot (Fig. 6.3b). As V_M is made less negative, we reach the point where both the GS and an excited state (ES) are pulsed across E_F (Fig. 6.3c). The effective rate for tunneling on the box is now the sum of the rate for tunneling in the GS and for tunneling in the ES, and as a result the dip becomes deeper (the electron response increases). When V_M is made even less negative, the one-electron GS lies below E_F during both stages of the pulse, so there is always one electron on the dot. The electron response is now zero and the dip ends.

The derivative of a set of curves as in Fig. 6.3a is plotted in Fig. 6.3d. Three lines are observed. The right vertical, dark line corresponds to the right flank of the dip in Fig. 6.3a, the onset of tunneling to the GS. The slanted bright line corresponds to the left flank of the dip in Fig. 6.3a (with opposite sign in the derivative) and reflects the pulse amplitude. The second, weaker, but clearly

visible dark vertical line represents an ES. The distance between the two vertical lines is proportional to the energy difference between GS and ES.

We identify the ground and first excited state observed in this spectroscopy experiment as the spin-up and spin-down state of a single electron on the quantum dot. For $B_{//} = 10$ T, the Zeeman energy is about 0.21 meV [9], while the excitation energy of the first orbital excited state is of order 1 meV. The distance between the two vertical lines can, in principle, be converted to energy and directly provide the spin excitation energy. However, it is difficult to determine independently the conversion factor between gate voltage and energy in this regime of a nearly closed quantum dot. Instead we take the measured Zeeman splitting from an earlier transport measurement [9] and deduce the conversion factor from gate voltage to energy, $\alpha = 105$ meV/V. This value will be used below, to convert the two-electron data to energy.

6.4   Excited-state spectroscopy for $N = 2$

Fig. 6.4a shows pulse spectroscopy data for the one-to-two electron transition, taken with the gate settings indicated by $\diamond$ in Fig. 6.2b. The rightmost vertical line corresponds to transitions between the one-electron GS (spin-up) and the two-electron GS (spin singlet) only. As V_P is increased above 5 mV, the two-electron ES (spin triplet) also becomes accessible, leading to an enhanced tunnel rate [10]. This gives rise to the left vertical line, and the distance between the two vertical lines corresponds to the singlet-triplet energy splitting ΔE_{ST}. Converted to energy, we obtain $\Delta E_{ST} = 0.49$ meV.

Excitations of the one-electron dot can be made visible at the one-to-two electron transition as well, by changing the pulse frequency to 1.538 kHz (Fig. 6.4b). This is too fast for electrons to tunnel if only the GS is accessible, so the rightmost line almost vanishes. However, a second slanted line becomes visible (indicated by the arrow in Fig. 6.4b), corresponding not to an increased tunnel rate into the dot (due to an $N = 2$ ES), but to an increased tunnel rate out of the dot (due to an $N = 1$ ES). Specifically, if the pulse amplitude is sufficiently large, either the spin-up or the spin-down electron can tunnel out of the two-electron dot. This is explained schematically in Fig. 6.4c and d.

Similar experiments at the transition between two and three electrons, and for tunnel rates to the reservoir ranging from 12 Hz to 12 kHz, yield similar excitation spectra.

This work demonstrates that an electrometer such as a QPC can reveal not only the charge state of a quantum dot, but also its tunnel coupling to the outside
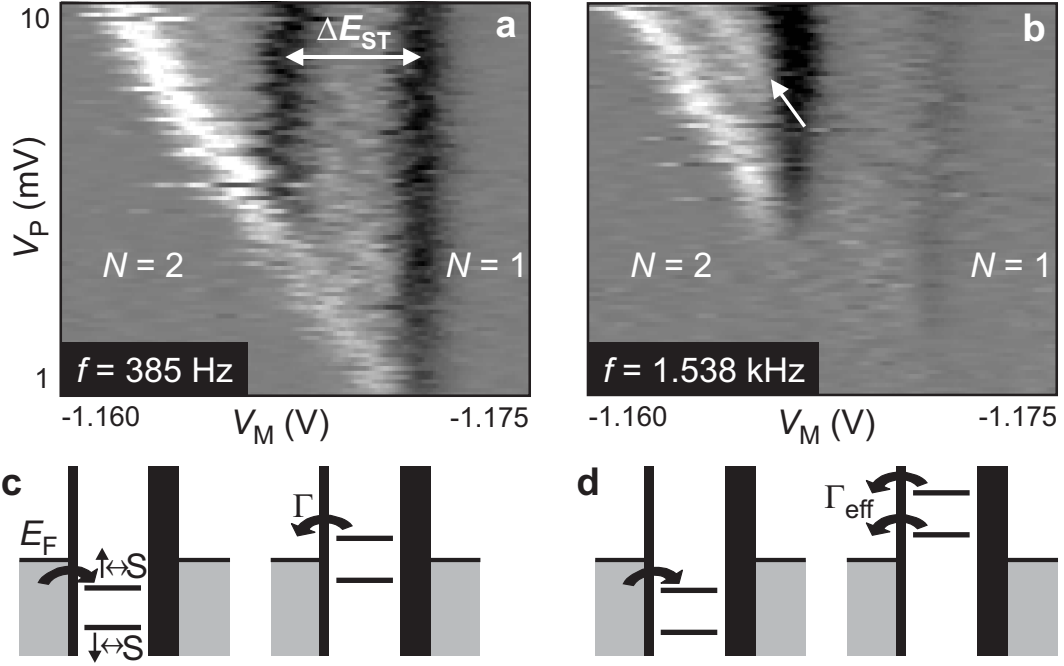
Figure 6.4: Excited state spectroscopy in a two-electron dot. **(a)** Similar to Fig. 6.3d, but for the one-to-two electron transition. Again, $f = 385$ Hz. We clearly observe the singlet-triplet splitting ΔE_{ST} (individual traces in (a) and (b) have been lined up). **(b)** Same experiment but with $f = 1.538$ kHz, which increases the contrast for excited states. An extra slanted line appears (arrow), corresponding to the $N = 1$ ES, spin-down. **(c)** Schematic electrochemical potential diagram for the case that only the spin-down electron can leave from the two-electron GS (spin singlet). This occurs to the left of the bright line indicated by the arrow in (b). **(d)** Idem when either the spin-up or the spin-down electron can leave from the spin singlet. This occurs to the right of the arrow in (b), and leads to a larger effective tunnel rate.

world and the energy level spectrum of its internal states. We can thus access all the relevant properties of a quantum dot, even when it is almost completely isolated from the leads.

References

[1] D. Loss and D.P. DiVincenzo, Phys. Rev. A **57**, 120 (1998).

[2] L.P. Kouwenhoven, C.M. Marcus, P.L. McEuen, S. Tarucha, R.M. Westervelt, and N.S. Wingreen, in Mesoscopic Electron Transport, v. 345 of NATO Advanced Study Institutes, Ser. E: Applied Sciences, L. L. Sohn, L. P. Kouwenhoven, G. Schön, Eds. (Kluwer Academic, Dordrecht, 1997).

[3] M. Ciorga, A. S. Sachrajda, P. Hawrylak, C. Gould, P. Zawadzki, S. Jullian, Y. Feng, and Z. Wasilewski1, Phys. Rev. B **61**, R16315 (2000).

[4] P. Lafarge, H. Pothier, E.R. Williams, D. Esteve, C. Urbina, and M.H. Devoret, Zeitschrift für Physik B, **85**, 327 (1991).

[5] R.C. Ashoori, H. L. Stormer, J. S. Weiner, L. N. Pfeiffer, S. J. Pearton, K. W. Baldwin, and K. W. West, Phys. Rev. Lett. **68**, 3088 (1992).

[6] K.W. Lehnert, K. Bladh, L. F. Spietz, D. Gunnarsson, D. I. Schuster, P. Delsing, and R. J. Schoelkopf, Phys. Rev. Lett. **90**, 027002 (2003).

[7] M. Field, C. G. Smith, M. Pepper, D. A. Ritchie, J. E. F. Frost, G. A. C. Jones, and D. G. Hasko, Phys. Rev. Lett. **70**, 1311 (1993).

[8] D. Sprinzak, Y. Ji, M. Heiblum, D. Mahalu, and H. Shtrikman, Phys. Rev. Lett. **88**, 176805 (2002).

[9] R. Hanson, B. Witkamp, L. M. K. Vandersypen, L. H. Willems van Beveren, J. M. Elzerman, and L. P. Kouwenhoven, Phys. Rev. Lett. **91**, 196802 (2003).

[10] The expected Zeeman splitting of the triplet state is not resolved here.

[11] J. M. Elzerman, R. Hanson, J. S. Greidanus, L. H. Willems van Beveren, S. De Franceschi, L. M. K. Vandersypen, S. Tarucha, and L. P. Kouwenhoven, Phys. Rev. B **67**, R161308 (2003).

Chapter 7

Single-shot read-out of a single electron spin using a difference in energy

J. M. Elzerman, R. Hanson, L. H. Willems van Beveren,
B. Witkamp, L. M. K. Vandersypen and L. P. Kouwenhoven

Spin is a fundamental property of all elementary particles. Classically it can be viewed as a tiny magnetic moment, but a measurement of an electron spin along the direction of an external magnetic field can have only two outcomes [1]: parallel or anti-parallel to the field. This discreteness reflects the quantum mechanical nature of spin. Ensembles of many spins have found diverse applications ranging from magnetic resonance imaging [2] to magneto-electronic devices [3], while individual spins are considered as carriers for quantum information. Read-out of single spin states has been achieved using optical techniques [4], and is within reach of magnetic resonance force microscopy [5]. However, electrical read-out of single spins [6, 7, 8, 9, 10, 11, 12, 13] has so far remained elusive. Here, we demonstrate electrical single-shot measurement of the state of an individual electron spin in a semiconductor quantum dot [14]. We use spin-to-charge conversion of a single electron confined in the dot, and detect the single-electron charge using a quantum point contact; the spin measurement visibility is $\sim 65\%$. Furthermore, we observe very long single-spin energy relaxation times (up to ~ 0.85 ms at a magnetic field of 8 Tesla), which are encouraging for the use of electron spins as carriers of quantum information.

7.1   Measuring electron spin in quantum dots

In quantum dot devices, single electron charges are easily measured. Spin states in quantum dots, however, have only been studied by measuring the average signal from a large ensemble of electron spins [17, 18, 19, 20, 21, 22]. In contrast, the experiment presented here aims at a single-shot measurement of the spin orientation (parallel or antiparallel to the field, denoted as spin-↑ and spin-↓, respectively) of a particular electron; only one copy of the electron is available, so no averaging is possible. The spin measurement relies on spin-to-charge conversion [20, 21] followed by charge measurement in a single-shot mode [15, 16]. Fig. 7.1a schematically shows a single electron spin confined in a quantum dot (circle). A magnetic field is applied to split the spin-↑ and spin-↓ states by the Zeeman energy. The dot potential is then tuned such that if the electron has spin-↓ it will leave, whereas it will stay on the dot if it has spin-↑. The spin state has now been correlated with the charge state, and measurement of the charge on the dot will reveal the original spin state.

This concept is implemented using a structure [23] (Fig. 7.1b) consisting of a quantum dot in close proximity to a quantum point contact (QPC). The quantum dot is used as a box to trap a single electron, and the QPC is operated as a charge detector in order to determine whether the dot contains an electron or not. The quantum dot is formed in the two-dimensional electron gas (2DEG) of a GaAs/AlGaAs heterostructure by applying negative voltages to the metal surface gates M, R, and T. This depletes the 2DEG below the gates and creates a potential minimum in the centre, that is, the dot (indicated by a dotted white circle). We tune the gate voltages such that the dot contains either zero or one electron (which we can control by the voltage applied to gate P). Furthermore, we make the tunnel barrier between gates R and T sufficiently opaque that the dot is completely isolated from the drain contact on the right. The barrier to the reservoir on the left is set [24] to a tunnel rate $\Gamma \approx (0.05 \text{ ms})^{-1}$. When an electron tunnels on or off the dot, it changes the electrostatic potential in its vicinity, including the region of the nearby QPC (defined by R and Q). The QPC is set in the tunnelling regime, so that the current, I_{QPC}, is very sensitive to electrostatic changes [25]. Recording changes in I_{QPC} thus permits us to measure on a timescale of about 8 μs whether an electron resides on the dot or not [26]. In this way the QPC is used as a charge detector with a resolution much better than a single electron charge and a measurement timescale almost ten times shorter than $1/\Gamma$.

The device is placed inside a dilution refrigerator, and is subject to a magnetic field of 10 T (unless noted otherwise) in the plane of the 2DEG. The measured
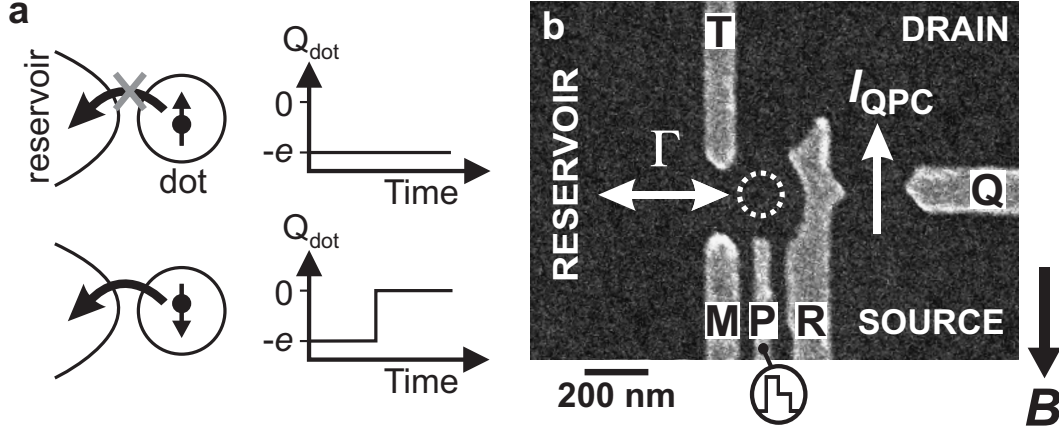
Figure 7.1: Spin-to-charge conversion in a quantum dot coupled to a quantum point contact. **(a)** Principle of spin-to-charge conversion. The charge on the quantum dot, Q_{dot}, remains constant if the electron spin is $\uparrow$, whereas a spin-$\downarrow$ electron can escape, thereby changing Q_{dot}. **(b)** Scanning electron micrograph of the metallic gates on the surface of a $GaAs/Al_{0.27}Ga_{0.73}As$ heterostructure containing a two-dimensional electron gas (2DEG) 90 nm below the surface. The electron density is 2.9×10^{15} m^{-2}. (Only the gates used in the present experiment are shown, the complete device is described in Ref. [23].) Electrical contact is made to the QPC source and drain and to the reservoir via Ohmic contacts. With a source-drain bias voltage of 1 mV, I_{QPC} is about 30 nA, and an individual electron tunnelling on or off the dot changes I_{QPC} by $\sim$ 0.3 nA. The QPC-current is sent to a room temperature current-to-voltage convertor, followed by a gain 1 isolation amplifier, an AC-coupled 40 kHz SRS650 low-pass filter, and is digitized at a rate of 2.2×10^6 samples/s. With this arrangement, the step in I_{QPC} resulting from an electron tunnelling is clearly larger than the rms noise level, provided it lasts at least 8 μs. A magnetic field, B, is applied in the plane of the 2DEG.

Zeeman splitting in the dot [21], $\Delta E_Z \approx 200\mu$eV, is larger than the thermal energy (25 μeV) but smaller than the orbital energy level spacing (1.1 meV) and the charging energy (2.5 meV).

7.2 Two-level pulse technique

To test our single-spin measurement technique, we use an experimental procedure based on three stages: 1) empty the dot, 2) inject one electron with unknown spin, and 3) measure its spin state. The different stages are controlled by voltage pulses on gate P (Fig. 7.2a), which shift the dot's energy levels (Fig. 7.2c). Before the pulse the dot is empty, as both the spin-$\uparrow$ and spin-$\downarrow$ levels are above the Fermi energy of the reservoir, E_F. Then a voltage pulse pulls both levels below
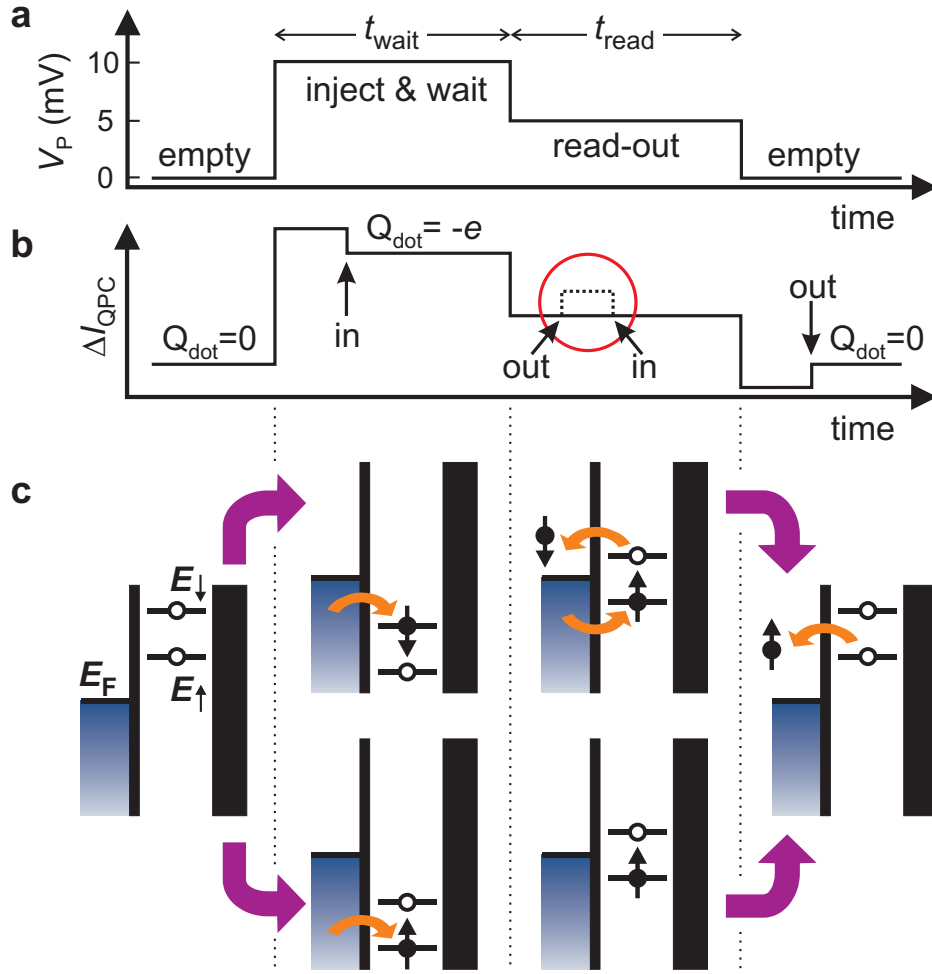
Figure 7.2: Two-level pulse technique used to inject a single electron and measure its spin orientation. **(a)** Shape of the voltage pulse applied to gate P. The pulse level is 10 mV during t_{wait} and 5 mV during t_{read} (which is 0.5 ms for all measurements). **(b)** Schematic QPC pulse-response if the injected electron has spin-↑ (solid line) or spin-↓ (dotted line; the difference with the solid line is only seen during the read-out stage). Arrows indicate the moment an electron tunnels into or out of the quantum dot. **(c)** Schematic energy diagrams for spin-↑ ($E_↑$) and spin-↓ ($E_↓$) during the different stages of the pulse. Black vertical lines indicate the tunnel barriers. The tunnel rate between the dot and the QPC-drain on the right is set to zero. The rate between the dot and the reservoir on the left is tuned to a specific value, Γ. If the spin is ↑ at the start of the read-out stage, no change in the charge on the dot occurs during t_{read}. In contrast, if the spin is ↓, the electron can escape and be replaced by a spin-↑ electron. This charge transition is detected in the QPC-current (dotted line inside red circle in (b)).

E_F. It is now energetically allowed for an electron to tunnel onto the dot, which will happen after a typical time $\sim \Gamma^{-1}$. The particular electron can have spin-$\uparrow$ (shown in the lower diagram) or spin-$\downarrow$ (upper diagram). (The tunnel rate for spin-$\uparrow$ electrons is expected to be larger than that for spin-$\downarrow$ electrons [27], i.e. $\Gamma_\uparrow > \Gamma_\downarrow$, but we do not assume this a priori.) During this stage of the pulse, lasting t_{wait}, the electron is trapped on the dot and Coulomb blockade prevents a second electron to be added. After t_{wait} the pulse is reduced, in order to position the energy levels in the read-out configuration. If the electron spin is $\uparrow$, its energy level is below E_F, so the electron remains on the dot. If the spin is $\downarrow$, its energy level is above E_F, so the electron tunnels to the reservoir after a typical time $\sim \Gamma_\downarrow^{-1}$. Now Coulomb blockade is lifted and an electron with spin-$\uparrow$ can tunnel onto the dot. This occurs on a timescale $\sim \Gamma_\uparrow^{-1}$ (with $\Gamma = \Gamma_\uparrow + \Gamma_\downarrow$). After t_{read}, the pulse ends and the dot is emptied again.

The expected QPC-response, ΔI_{QPC}, to such a two-level pulse is the sum of two contributions (Fig. 7.2b). First, due to a capacitive coupling between pulse-gate and QPC, ΔI_{QPC} will change proportionally to the pulse amplitude. Thus, ΔI_{QPC} versus time resembles a two-level pulse. Second, ΔI_{QPC} tracks the charge on the dot, i.e. it goes up whenever an electron tunnels off the dot, and it goes down by the same amount when an electron tunnels on the dot. Therefore, if the dot contains a spin-$\downarrow$ electron at the start of the read-out stage, ΔI_{QPC} should go up and then down again. We thus expect a characteristic step in ΔI_{QPC} during t_{read} for spin-$\downarrow$ (dotted trace inside red circle). In contrast, ΔI_{QPC} should be flat during t_{read} for a spin-$\uparrow$ electron. Measuring whether a step is present or absent during the read-out stage constitutes our spin measurement.

7.3 Tuning the quantum dot into the read-out configuration

To perform spin read-out, V_M has to be fine-tuned so that the position of the energy levels with respect to E_F is as shown in Fig. 7.2c. To find the correct settings, we apply a two-level voltage pulse and measure the QPC-response for increasingly negative values of V_M (Fig. 7.3a). Four different regions in V_M can be identified (separated by white dotted lines), with qualitatively different QPC-responses. The shape of the typical QPC-response in each of the four regions (Fig. 7.3b) allows us to infer the position of $E_\uparrow$ and $E_\downarrow$ with respect to E_F during all stages of the pulse (Fig. 7.3c).

In the top region, the QPC-response just mimics the applied two-level pulse, indicating that here the charge on the dot remains constant throughout the pulse.
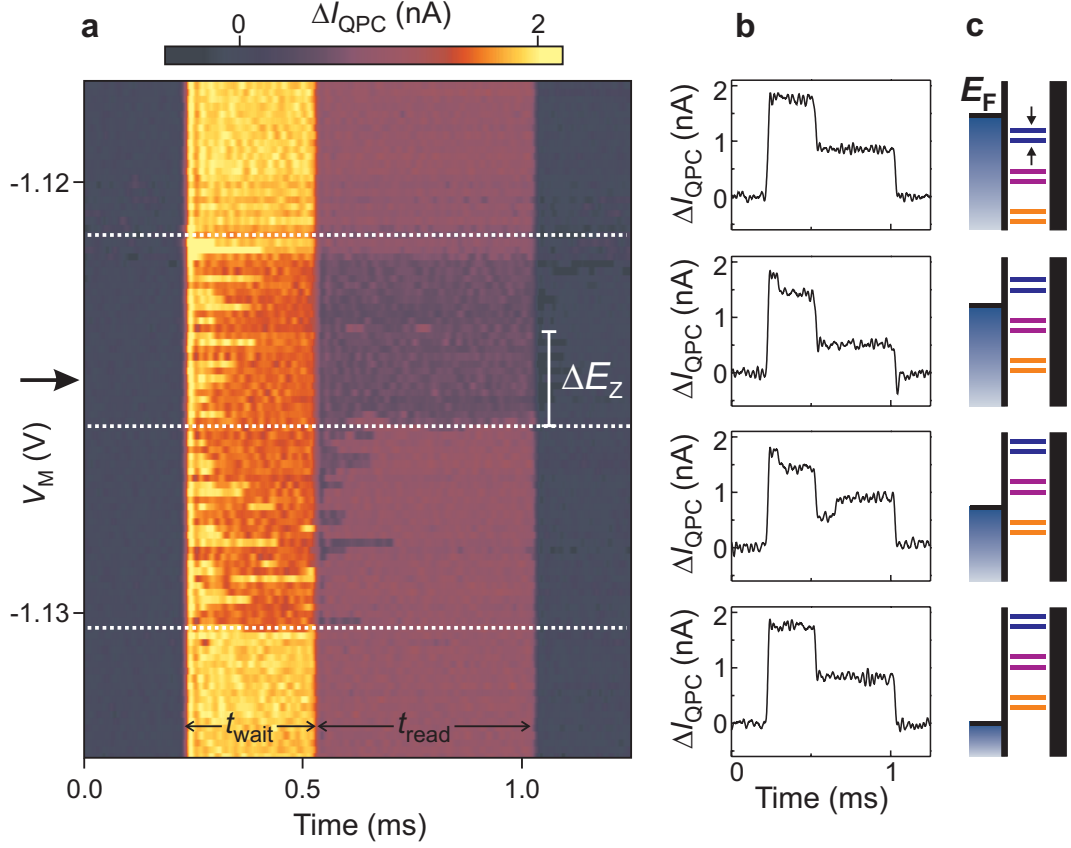
Figure 7.3: Tuning the quantum dot into the spin read-out configuration. We apply a two-stage voltage pulse as in Fig. 7.2a ($t_{wait} = 0.3$ ms, $t_{read} = 0.5$ ms), and measure the QPC-response for increasingly negative values of V_M. **(a)** QPC-response (in colour-scale) versus V_M. Four different regions in V_M can be identified (separated by white dotted lines), with qualitatively different QPC-responses. **(b)** Typical QPC-response in each of the four regions. This behaviour can be understood from the energy levels during all stages of the pulse. **(c)** Schematic energy diagrams showing $E_\uparrow$ and $E_\downarrow$ with respect to E_F before and after the pulse (blue), during t_{wait} (orange) and during t_{read} (purple), for four values of V_M. For the actual spin read-out experiment, V_M is set to the optimum position (indicated by the arrow in a).

This implies that $E_\uparrow$ remains below E_F for all stages of the pulse, thus the dot remains occupied with one electron. In the second region from the top, tunnelling occurs, as seen from the extra steps in ΔI_{QPC}. The dot is empty before the pulse, then an electron is injected during t_{wait}, which escapes after the pulse. This corresponds to an energy level diagram similar to before, but with $E_\uparrow$ and $E_\downarrow$ shifted up due to the more negative value of V_M in this region. In the third region from the top, an electron again tunnels on the dot during t_{wait}, but now it can

escape already during t_{read}, irrespective of its spin. Finally, in the bottom region no electron-tunneling is seen, implying that the dot remains empty throughout the pulse.

Since we know the shift in V_M corresponding to shifting the energy levels by ΔE_Z, we can set V_M to the optimum position for the spin read-out experiment (indicated by the arrow). For this setting, the energy levels are as shown in Fig. 7.2c, i.e. E_F is approximately in the middle between $E_\uparrow$ and $E_\downarrow$ during the read-out stage.

7.4 Single-shot read-out of one electron spin

Fig. 7.4a shows typical experimental traces of the pulse-response recorded after proper tuning of the DC gate voltages (see Fig. 7.3). We emphasize that each trace involves injecting one particular electron on the dot and subsequently measuring its spin state. Each trace is therefore a single-shot measurement. The traces we obtain fall into two different classes; most traces qualitatively resemble the one in the top panel of Fig. 7.4a, some resemble the one in the bottom panel. These two typical traces indeed correspond to the signals expected for a spin-↑ and a spin-↓ electron (Fig. 7.2b), a strong indication that the electron in the top panel of Fig. 7.4a was spin-↑ and in the bottom panel spin-↓. The distinct signature of the two types of responses in ΔI_{QPC} permits a simple criterion for identifying the spin [28]: if ΔI_{QPC} goes above the threshold value (red line in Fig. 7.4a and chosen as explained below), we declare the electron 'spin-down'; otherwise we declare it 'spin-up'. Fig. 7.4b shows the read-out section of twenty more 'spin-down' traces, to illustrate the stochastic nature of the tunnel events.

The random injection of spin-↑ and spin-↓ electrons prevents us from checking the outcome of any individual measurement. Therefore, in order to further establish the correspondence between the actual spin state and the outcome of our spin measurement, we change the probability to have a spin-↓ at the beginning of the read-out stage, and compare this with the fraction of traces in which the electron is declared 'spin-down'. As t_{wait} is increased, the time between injection and read-out, t_{hold}, will vary accordingly ($t_{hold} \approx t_{wait}$). The probability for the spin to be ↓ at the start of t_{read} will thus decay exponentially to zero, since electrons in the excited spin state will relax to the ground state ($k_B T << \Delta E_Z$). For a set of 15 values of t_{wait} we take 625 traces for each t_{wait}, and count the fraction of traces in which the electron is declared 'spin-down' (Fig. 7.4c). The fact that the expected exponential decay is clearly reflected in the data confirms the validity of the spin read-out procedure.
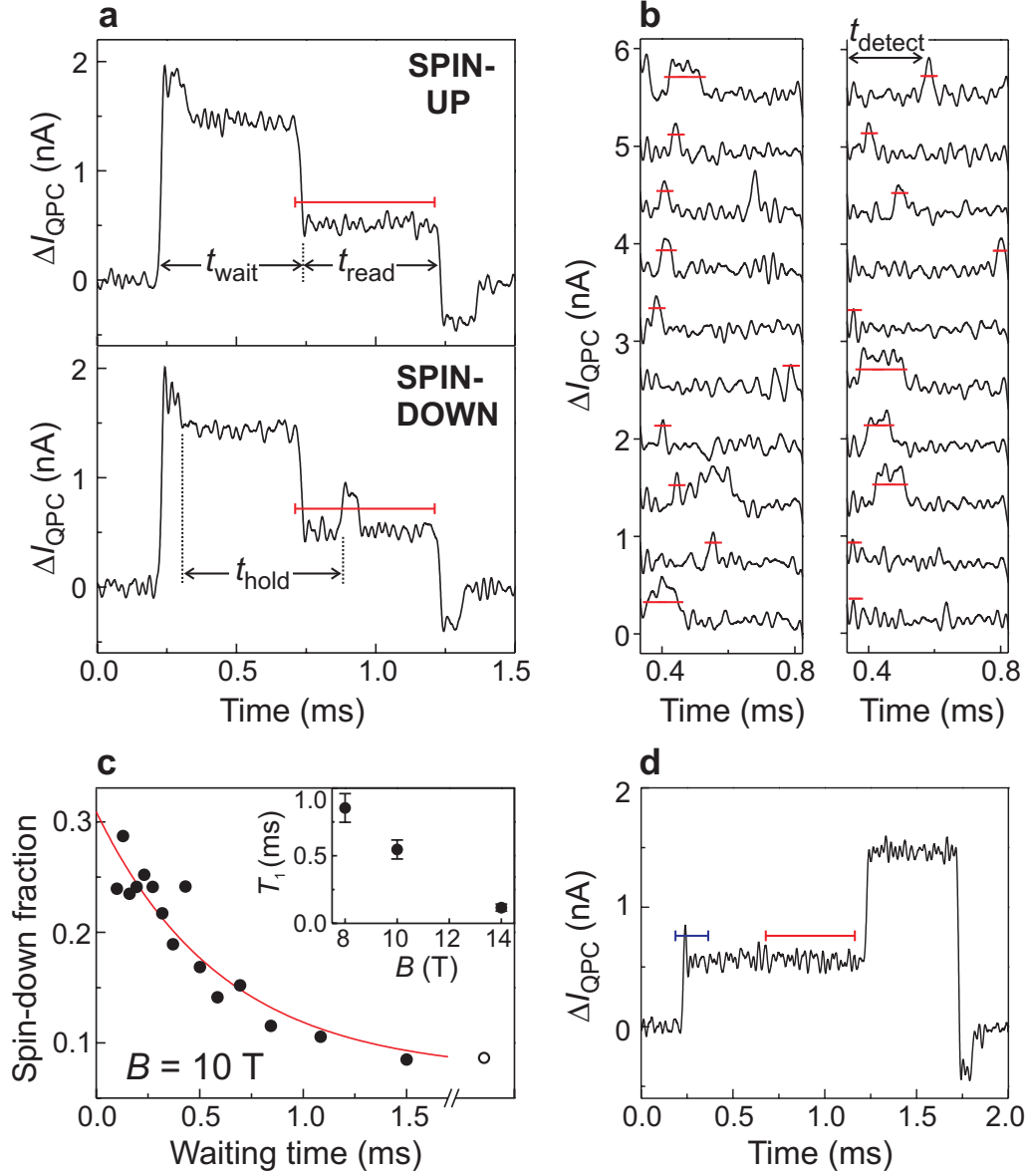
Figure 7.4: Single-shot read-out of one electron spin. **(a)** Time-resolved QPC measurements. Top panel: an electron injected during t_{wait} is declared 'spin-up' during t_{read}. Bottom panel: the electron is declared 'spin-down'. **(b)** Examples of 'spin-down' traces (for $t_{wait} = 0.1$ ms). Only the read-out segment is shown, and traces are offset for clarity. The time when ΔI_{QPC} first crosses the threshold, t_{detect}, is recorded to make the histogram in Fig. 7.7a. **(c)** Fraction of 'spin-down' traces versus t_{wait}, out of 625 traces for each waiting time. Open dot: spin-down fraction using modified pulse shape (d). Red solid line: exponential fit to the data. Inset: T_1 versus B. **(d)** Typical QPC-signal for a 'reversed' pulse, with the same amplitudes as in Fig. 7.2a, but a reversed order of the two stages. The red threshold is used to obtain the open dot in (c), the blue threshold is used in Fig. 7.7b (see text).
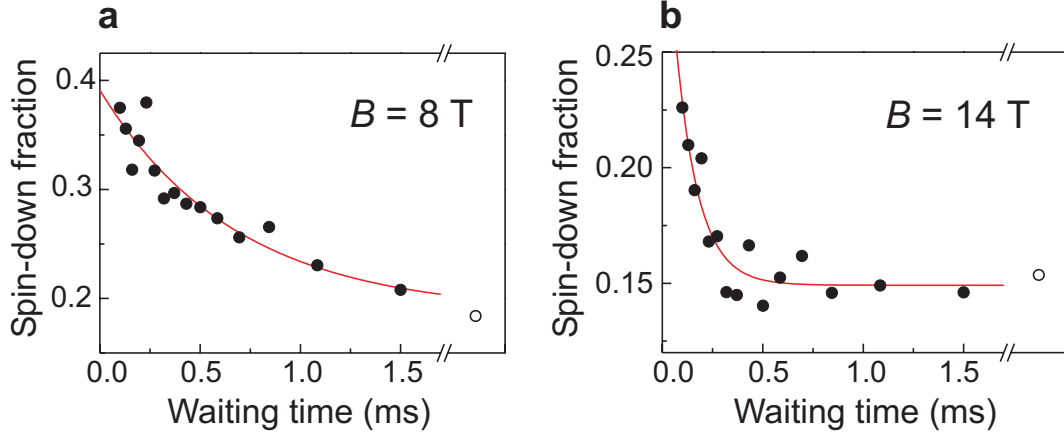
Figure 7.5: Measurement of the spin-relaxation time as in Fig. 7.4c, but at different magnetic fields. Averaging the results of an exponential fit (as shown) over three similar measurements yields **(a)**, $T_1 = (0.85 \pm 0.11)$ ms at 8 T and **(b)**, $T_1 = (0.12 \pm 0.03)$ ms at 14 T.

As an extra check that the observed decay is due to spin relaxation, we apply a pulse waveform where the two pulse stages are reversed (Fig. 7.4d). In this case injection takes place with $E_\uparrow$ below and $E_\downarrow$ above E_F (see Fig. 7.2c, third column), so that always a spin-$\uparrow$ electron is injected. By comparing the signal with a threshold (red line in Fig. 7.4d) as before, we find the fraction of spin-$\uparrow$ electrons that is measured to be 'spin-down', which is nonzero due to measurement inaccuracy (see below). This fraction, indicated by the open dot in Fig. 7.4c, agrees very well with the value found for the longest waiting time (1.5 ms), demonstrating that here the electrons with spin-$\downarrow$ indeed have relaxed to spin-$\uparrow$.

We extract a single-spin energy relaxation time, T_1, from fitting the datapoints in Fig. 7.4c (and two other similar measurements) to $\alpha + C \exp(-t_{wait}/T_1)$, and obtain an average value of $T_1 \approx (0.55 \pm 0.07)$ ms at 10 Tesla. This is an order of magnitude longer than the lower bound on T_1 established earlier [21], and clearly longer than the time needed for the spin measurement (of order $1/\Gamma_\downarrow \approx 0.11$ ms). A similar experiment at 8 Tesla gives $T_1 \approx (0.85 \pm 0.11)$ ms and at 14 Tesla we find $T_1 \approx (0.12 \pm 0.03)$ ms (Fig. 7.5). More experiments are needed in order to test the theoretical prediction that relaxation at high magnetic fields is dominated by spin-orbit interactions [29, 30, 31], with smaller contributions resulting from hyperfine interactions with the nuclear spins [29, 32] (cotunnelling is insignificant given the very small tunnel rates). We note that the obtained values for T_1 refer to our entire device under active operation: i.e. a single spin in a quantum dot subject to continuous charge detection by a QPC.
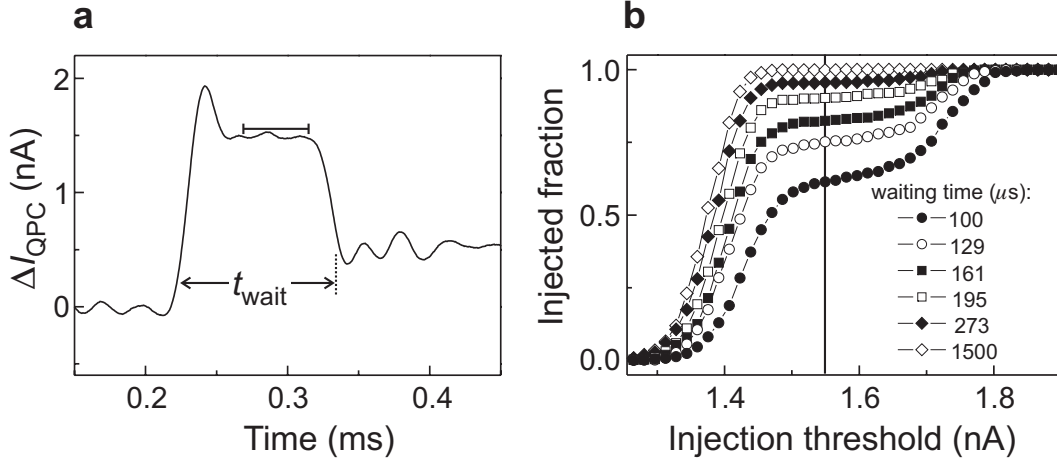
Figure 7.6: Setting the injection threshold. **(a)** Example of QPC-signal for the shortest waiting time used (0.1 ms). The horizontal line indicates the injection threshold. Injection is declared successful if the QPC-signal is below the injection threshold for a part or all of the last 45 μs before the end of the injection stage (t_{wait}). Traces in which injection was not successful, i.e. no electron was injected during t_{wait}, are disregarded. **(b)** Fraction of traces in which injection was successful, out of a total of 625 taken for each waiting time. The threshold chosen for analysing all data is indicated by the vertical line.

7.5   Measurement fidelity

For applications in quantum information processing it is important to know the accuracy, or fidelity, of the single-shot spin read-out. The measurement fidelity is characterised by two parameters, α and β (inset to Fig. 7.7a), which we now determine for the data taken at 10 T.

The parameter α corresponds to the probability that the QPC-current exceeds the threshold even though the electron was actually spin-↑, for instance due to thermally activated tunnelling or electrical noise (similar to 'dark counts' in a photon detector). The combined probability for such processes is given by the saturation value of the exponential fit in Fig. 7.4c, α, which depends on the value of the threshold current. We analyse the data in Fig. 7.4c using different thresholds, and plot α in Fig. 7.7b.

The parameter β corresponds to the probability that the QPC-current stays below the threshold even though the electron was actually spin-↓ at the start of the read-out stage. Unlike α, β cannot be extracted directly from the exponential fit (note that the fit parameter $C = p(1 - \alpha - \beta)$ contains two unknowns: $p = \Gamma_{\downarrow}/(\Gamma_{\uparrow} + \Gamma_{\downarrow})$ and β). We therefore estimate β by analysing the two processes that contribute to it. First, a spin-↓ electron can relax to spin-↑ before spin-to-charge
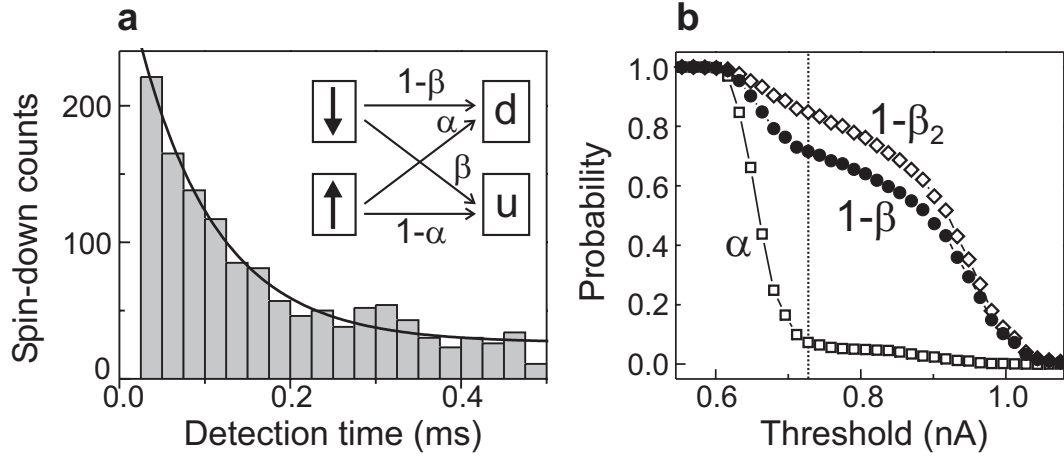
Figure 7.7: Measurement fidelity. **(a)** Histogram showing the distribution of detection times, t_{detect}, in the read-out stage (see Fig. 7.4b for definition t_{detect}). The exponential decay is due to spin-↓ electrons tunnelling out of the dot (rate = $\Gamma_\downarrow$) and due to spin flips during the read-out stage (rate = $1/T_1$). Solid line: exponential fit with a decay time $(\Gamma_\downarrow + 1/T_1)^{-1}$ of 0.09 ms. Given that $T_1 = 0.55$ ms, this yields $\Gamma_\downarrow^{-1} \approx 0.11$ ms. Inset: fidelity parameters. A spin-↓ electron is declared 'down' (d) or 'up' (u) with probability $1 - \beta$ or β, respectively. A spin-↑ electron is declared 'up' or 'down' with probability $1 - \alpha$ or α, respectively. **(b)** Open squares represent α, obtained from the saturation value of exponential fits as in Fig. 7.4c for different values of the read-out threshold. A current of 0.54 nA (0.91 nA) corresponds to the average value of ΔI_{QPC} when the dot is occupied (empty) during t_{read}. Open diamonds: measured fraction of 'reverse-pulse' traces in which ΔI_{QPC} crosses the injection threshold (blue line in Fig. 7.4d). This fraction approximates $1 - \beta_2$, where β_2 is the probability of identifying a spin-↓ electron as 'spin-up' due to the finite bandwidth of the measurement setup. Filled circles: total fidelity for the spin-↓ state, $1 - \beta$, calculated using $\beta_1 = 0.17$. The vertical dotted line indicates the threshold for which the visibility $1 - \alpha - \beta$ (separation between filled circles and open squares) is maximal. This threshold value of 0.73 nA is used in the analysis of Fig. 7.4.

conversion takes place. This occurs with probability $\beta_1 = 1/(1 + T_1\Gamma_\downarrow)$. From a histogram (Fig. 7.7a) of the actual detection time, t_{detect} (see Fig. 7.4b), we find $\Gamma_\downarrow^{-1} \approx 0.11$ ms, yielding $\beta_1 \approx 0.17$. Second, if the spin-↓ electron does tunnel off the dot but is replaced by a spin-↑ electron within about 8 μs, the resulting QPC-step is too small to be detected. The probability that a step is missed, β_2, depends on the value of the threshold. It can be determined by applying a modified ('reversed') pulse (Fig. 7.4d). For such a pulse, we know that in each trace an electron is injected in the dot, so there should always be a step at the start of the pulse. The fraction of traces in which this step is nevertheless missed,

i.e. ΔI_{QPC} stays below the threshold (blue line in Fig. 7.4d), gives β_2. We plot $1-\beta_2$ in Fig. 7.7b (open diamonds). The resulting total fidelity for spin-$\downarrow$ is given by $1 - \beta \approx (1 - \beta_1)(1 - \beta_2) + (\alpha\beta_1)$. The last term accounts for the case when a spin-$\downarrow$ electron is flipped to spin-$\uparrow$, but there is nevertheless a step in ΔI_{QPC} due to the dark-count mechanism [33]. In Fig. 7.7b we also plot the extracted value of $1 - \beta$ as a function of the threshold.

We now choose the optimal value of the threshold as the one for which the visibility $1 - \alpha - \beta$ is maximal (vertical line in Fig. 7.7b). For this setting, $\alpha \approx 0.07$, $\beta_1 \approx 0.17$, $\beta_2 \approx 0.15$, so the measurement fidelity for the spin-$\uparrow$ and the spin-$\downarrow$ state is ~ 0.93 and ~ 0.72 respectively. The measurement visibility in a single-shot measurement is thus at present 65%.

Significant improvements in the spin measurement visibility can be made by lowering the electron temperature (smaller α) and especially by making the charge measurement faster (smaller β). Already, the demonstration of single-shot spin read-out and the observation of T_1 of order 1 ms are encouraging results for the use of electron spins as quantum bits.

References

[1] J. J. Sakurai, Modern Quantum Mechanics. Addison-Wesley (Reading MA, USA, 1994).

[2] F. W. Wehrli, Physics Today **6**, 34 (1992).

[3] S. A. Wolf *et al.*, Science **294**, 1488-1495 (2001).

[4] R. Blatt and P. Zoller, Eur. J. Phys. **9**, 250-279 (1988).

[5] H. J. Mamin, R. Budakian, B. W. Chui and D. Rugar, Phys. Rev. Lett. **91**, 207604 (2003).

[6] D. Loss and D. P. DiVincenzo, Phys. Rev. A **57**, 120-126 (1998).

[7] B. E. Kane, Nature **393**, 133-137 (1998).

[8] L. M. K. Vandersypen *et al.*, in Quantum Computing and Quantum Bits in Mesoscopic Systems, Kluwer Academic/Plenum Publishers (New York, 2003). See also http://xxx.lanl.gov/abs/quant-ph/0207059 (2002).

[9] M. Xiao, I. Martin, and H. W. Jiang, Phys. Rev. Lett. **91**, 078301 (2003).

[10] M. Friesen *et al.*, Phys. Rev. Lett. **92**, 037901 (2004).

[11] H. A. Engel *et al.*, Phys. Rev. Lett. **93**, 106804 (2004).

[12] R. Ionicioiu *et al.*, http://xxx.lanl.gov/abs/quant-ph/0310047 (2003).

[13] A. D. Greentree *et al.*, http://xxx.lanl.gov/abs/cond-mat/0403449 (2004).

[14] L. P. Kouwenhoven, D. G. Austing and S. Tarucha, Rep. Prog. Phys. **64**, 701-736 (2001).

[15] W. Lu *et al.*, Nature **423**, 422 (2003).

[16] T. Fujisawa *et al.*, Appl. Phys. Lett. **84**, 2343 (2004).

[17] J. Weis *et al.*, Surf. Sci. **305**, 664 (1994).

[18] L. P. Kouwenhoven *et al.*, Science **278**, 1788 (1997).

[19] Ciorga, M. *et al.*, Physica E **11**, 35 (2001).

[20] T. Fujisawa *et al.*, Nature **419**, 278-281 (2002).

[21] R. Hanson *et al.*, Phys. Rev. Lett. **91**, 196802 (2003).

[22] J. A. Folk *et al.*, Science **299**, 679 (2003).

[23] J. M. Elzerman *et al.*, Phys. Rev. B **67**, R161308 (2003).

[24] J. M. Elzerman *et al.*, Appl. Phys. Lett. **84**, 4617-4619 (2004).

[25] M. Field *et al.*, Phys. Rev. Lett. **70**, 1311 (1993).

[26] L.M.K. Vandersypen *et al.*, Appl. Phys. Lett. **85**, 4394 (2004).

[27] R. Hanson *et al.*, http://xxx.lanl.gov/abs/cond-mat/011414v1 (2003).

[28] The automated data analysis procedure first corrects for the offset of each trace. This offset, resulting from low-frequency interference signals or charge switches, is found by making a histogram of the QPC current during the read-out stage of a particular trace. The histogram typically displays a peak due to fluctuations around the average value corresponding to an occupied dot. The center of a gaussian fit to the histogram gives the offset. Then each trace is checked to make sure that an electron was injected during the injection stage, by evaluating if the signal goes below the injection threshold (dotted horizontal line in Fig. 7.6a). If not, the trace is disregarded. Finally, to determine if a trace corresponds to 'spin-up' or 'spin-down', we disregard

all points that lie below the previous point (since these could correspond to points on the falling pulse flank at the end of the injection stage), and check if any of the remaining points are above the threshold.

[29] A. V. Khaetskii and Y. V. Nazarov, Phys. Rev. B **64**, 125316 (2001).

[30] V. N. Golovach, A. Khaetskii and D. Loss, Phys. Rev. Lett. **93**, 016601 (2004).

[31] L. M. Woods, T. L. Reinecke and Y. Lyanda-Geller, Phys. Rev. B **66**, 161318(R) (2002).

[32] S. I. Erlingsson and Y. V. and Nazarov, Phys. Rev. B **66**, 155327 (2002).

[33] Let us assume there is a spin-$\downarrow$ electron on the dot at the start of the read-out stage. The probability that the $\downarrow$-electron tunnels out (i.e. that it does not relax to spin-$\uparrow$) is given by $1 - \beta_1$. The probability that this tunnel event is detected (i.e. is not too fast) is given by $1 - \beta_2$. Therefore, the probability that a spin-$\downarrow$ electron tunnels out and is detected, is $(1 - \beta_1)(1 - \beta_2)$. In addition, there is the possibility that the $\downarrow$-electron relaxes, with probability β_1, but a step in the QPC signal is nevertheless detected, with probability α, due to the 'dark count' mechanism. Therefore, the total probability that a spin-$\downarrow$ electron is declared 'spin-down' is given by $(1 - \beta_1)(1 - \beta_2) + (\alpha\beta_1)$ approximately.

Chapter 8

Single-shot read-out of two-electron spin states using spin-dependent tunnel rates

R. Hanson, L. H. Willems van Beveren, I. T. Vink,
J. M. Elzerman, W. J. M. Naber, F. H. L. Koppens,
L. P. Kouwenhoven and L. M. K. Vandersypen

We present a method for reading out the spin state of electrons in a quantum dot that is robust against charge noise and can still be used when the electron temperature exceeds the energy splitting between the states. A spin dependence of the tunnel rates is used to correlate the spin states to different charge states. A subsequent fast measurement of the charge on the dot then reveals the original spin state. We experimentally demonstrate the method by performing read-out of the two-electron spin states, achieving a single-shot visibility of more than 80%. We find very long triplet-to-singlet relaxation times (up to several milliseconds), with an in-plane magnetic field dependence consistent with spin-orbit coupling as the dominant source of relaxation.

8.1 Single-shot spin read-out using spin-dependent tunnel rates

The magnetic moment associated with the electron spin is tiny and therefore hard to measure directly. However, by correlating the spin states to different charge states and subsequently measuring the charge on the dot, the spin state can be determined [1]. Such a spin-to-charge conversion can be achieved by positioning the spin levels around the electrochemical potential of the reservoir μ_{res} as depicted in Fig. 8.1a, such that one electron can tunnel off the dot from the spin excited state, $|ES\rangle$, whereas tunneling from the ground state, $|GS\rangle$, is energetically forbidden. By combining this scheme with a fast (40 kHz bandwidth) measurement of the charge dynamics, we have recently performed read-out of the spin orientation of a single electron, with a single-shot visibility up to 65% [2] (see chapter 7). (A conceptionally similar scheme has also allowed single-shot read-out of a superconducting charge qubit [3]). However, this energy-selective read-out (E-RO) has three drawbacks: (i) E-RO requires an energy splitting of the spin states larger than the thermal energy of the electrons in the reservoir. Thus, for a single spin the read-out is only effective at very low electron temperature and high magnetic fields (8 T and higher in Ref. [2]). Also, interesting effects occurring close to degeneracy, e.g. near the singlet-triplet crossing for two electrons [4], can not be probed. (ii) Since the E-RO relies on precise positioning of the spin levels with respect to the reservoir, it is very sensitive to fluctuations in the electrostatic potential. Background charge fluctuations [5], active even in today's most stable devices, can easily push the levels out of the read-out configuration. (iii) High-frequency noise can spoil the E-RO by inducing photon-assisted tunneling from the spin ground state to the reservoir. Since the QPC is a source of shot noise, this limits the current through the QPC and thereby the bandwidth of the charge detection [6]. A different read-out method is desired that does not suffer from these constraints.

In this work, we present a spin read-out scheme where spin-to-charge conversion is achieved by exploiting the difference in *tunnel rates* of the different spin states to the reservoir [7]. We outline the concept of this tunnel-rate selective read-out (TR−RO) in Fig. 8.1b. Assume that the tunnel rate from the spin excited state $|ES\rangle$ to the reservoir, Γ_{ES}, is much higher than the tunnel rate from $|GS\rangle$, Γ_{GS}, i.e. $\Gamma_{ES} \gg \Gamma_{GS}$. Then, we can read out the spin state as follows. At time $t=0$, we position the levels of both $|ES\rangle$ and $|GS\rangle$ far above the electrochemical potential of the reservoir μ_{res}, so that one electron is energetically allowed to tunnel off the dot regardless of the spin state. Then, at a time $t = \tau$,
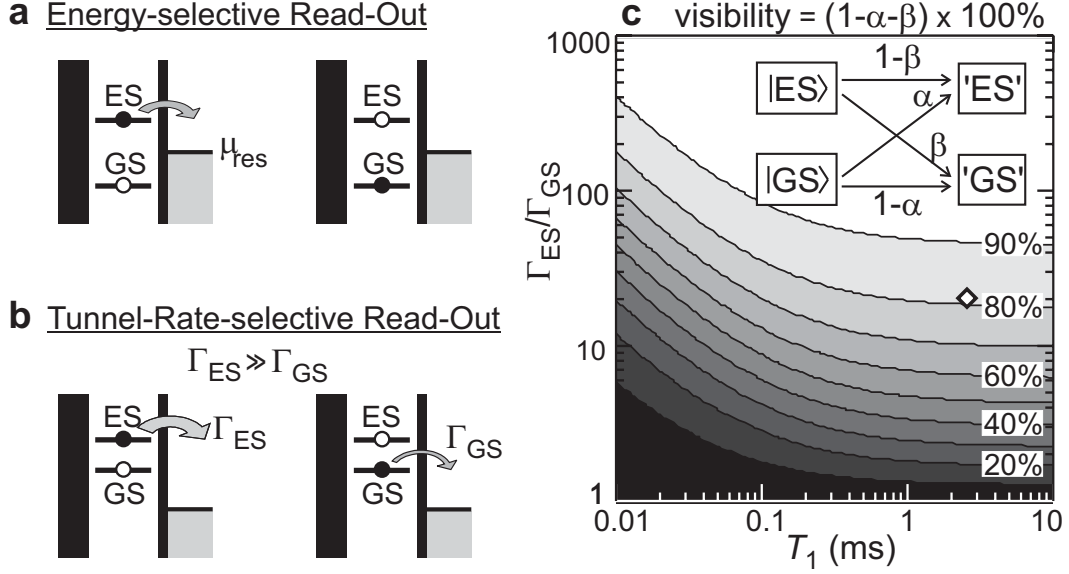
Figure 8.1: (a)-(b) Energy diagrams explaining two schemes for spin-to-charge conversion. (a) Energy-selective read-out (E-RO). Tunneling is energetically allowed from $|ES\rangle$ (left diagram), but not from $|GS\rangle$ (right diagram). (b) Tunnel rate-selective read-out (TR-RO). One electron is allowed to tunnel off the dot, regardless of the spin state, but the tunnel rate depends strongly on the spin state: $\Gamma_{ES} \gg \Gamma_{GS}$. If a charge measurement after a time τ, where $\Gamma_{GS}^{-1} \gg \tau \gg \Gamma_{ES}^{-1}$, indicates that one electron has (not) tunneled, the state is declared $'ES'$ ($'GS'$). (c) Visibility of the TR-RO as a function of spin relaxation time T_1 and the ratio Γ_{ES}/Γ_{GS}, for $\Gamma_{GS} = 2.5$ kHz. The diamond corresponds to the read-out parameters of Fig. 8.2e. Inset: definition of the error rates α and β. If the initial state is $|GS\rangle$, there is a probability α that the measurement gives the wrong outcome, i.e. $'ES'$ (β is defined similarly).

where $\Gamma_{GS}^{-1} \gg \tau \gg \Gamma_{ES}^{-1}$, an electron will have tunneled off the dot with a very high probability if the state was $|ES\rangle$, but most likely no tunneling will have occurred if the state was $|GS\rangle$. Thus, the spin information is converted to charge information, and a measurement of the number of electrons on the dot reveals the original spin state.

A major advantage of this TR-RO scheme is that it does not rely on a large energy splitting between the spin states. Furthermore, it is robust against background charge fluctuations, since these cause only a small variation in the tunnel rates (of order 10^{-3} in Ref. [5]). Finally, photon-assisted tunneling is not important since here tunneling is energetically allowed regardless of the initial spin state. Thus, we see that TR-RO can overcome the limitations of E-RO.

8.2   Measurement visibility of the read-out

We first analyze the fidelity of the TR-RO theoretically using the error rates α and β as defined in the diagram of Fig. 8.1c (inset). Here, α is the probability that one electron has tunneled even though the initial state was $|GS\rangle$, and β the probability that no tunneling has occurred even though the initial state was $|ES\rangle$. The charge measurement itself is assumed to be perfect, and spin relaxation from $|ES\rangle$ to $|GS\rangle$ is modeled by a rate $1/T_1$. We find analytically

$$\alpha = 1 - e^{-\Gamma_{GS} \cdot \tau}, \tag{8.1}$$

$$\beta = \frac{(1/T_1)e^{-\Gamma_{GS} \cdot \tau} + (\Gamma_{ES} - \Gamma_{GS})\, e^{-(\Gamma_{ES} + 1/T_1) \cdot \tau}}{\Gamma_{ES} + 1/T_1 - \Gamma_{GS}}, \tag{8.2}$$

where τ is the time at which we measure the number of electrons N [8]. The visibility of the read-out is $1 - \alpha - \beta$.

The optimal value for the read-out time for given values of T_1 and the ratio Γ_T/Γ_S, τ_{max}, is found by solving $d(\text{visibility})/d\tau = 0$ for τ. We find

$$\tau_{max} = \frac{1}{\Gamma_{ES} + 1/T_1 - \Gamma_{GS}}\; \ln\left(\frac{\Gamma_{ES} + 1/T_1}{\Gamma_{GS}}\right). \tag{8.3}$$

Inserting this expression into equations 8.1 and 8.2 yields the maximum visibility.

In Fig. 8.1c we plot the visibility for $\tau = \tau_{max}$ as a function of T_1 and the ratio of the tunnel rates Γ_{ES}/Γ_{GS}. (Here, Γ_{GS} is chosen to be 2.5 kHz, which is well within the bandwidth of our charge detection set up [6].) We see that for $\Gamma_{ES}/\Gamma_{GS} = 10$ and $T_1 = 0.5$ ms, the visibility is 65%, equal to the visibility obtained with E-RO in Ref. [2] for the same T_1. For $\Gamma_{ES}/\Gamma_{GS} > 60$ and $T_1 = 0.5$ ms, the visibility of TR-RO exceeds 90%.

The TR-RO can be used in a similar way if Γ_{ES} is much *lower* than Γ_{GS}. The visibility for this case can be calculated simply by replacing α and β in Eqs. 8.1-8.2 with $1 - \alpha$ and $1 - \beta$ respectively. Significant differences with the values in Fig. 8.1c arise only in the limit $T_1 \ll \Gamma_{ES}^{-1}$.

The main ingredient necessary for TR-RO is a spin dependence in the tunnel rates. For a single electron, this spin dependence can be obtained in the Quantum Hall regime, where a high spin-selectivity is induced by the spatial separation of spin-resolved edge channels [9, 10]. TR-RO can also be used for read-out of a two-electron dot, where the electrons are either in the spin-singlet ground state, denoted by $|S\rangle$, or in a spin-triplet state, denoted by $|T\rangle$. In $|S\rangle$, the two electrons both occupy the lowest orbital, but in $|T\rangle$ one electron is in the first excited orbital. Since the wave function in this excited orbital has more weight near the edge of the dot [11], the coupling to the reservoir is stronger than for

the lowest orbital. Therefore, the tunnel rate from a triplet state to the reservoir Γ_T is much larger than the rate from the singlet state Γ_S, i.e. $\Gamma_T \gg \Gamma_S$ [13]. We use this spin-dependence in the following to experimentally demonstrate TR-RO for two electrons.

8.3 Single-shot read-out of the two-electron spin states

A quantum dot (white dotted circle in Fig. 8.2a) and a QPC are defined in a two-dimensional electron gas (2DEG) with an electron density of $4 \cdot 10^{15}$ m^{-2}), 60 nm below the surface of a GaAs/AlGaAs heterostructure from Sumitomo Electric, by applying negative voltages to gates L, M, T and Q. Gate P is used to apply fast voltage pulses. We completely pinch off the tunnel barrier between gates L and T, so that the dot is only coupled to the reservoir on the right. The conductance of the QPC is tuned to about e^2/h, making it very sensitive to the number of electrons on the dot. A voltage bias of 0.8 mV induces a current through the QPC, I_{QPC}, of about 30 nA.

We tune the dot to the $N = 1 \leftrightarrow 2$ transition in a small parallel field $B_{/\!/}$ of 0.02 T. Here, the energy difference between $|T\rangle$ and the ground state $|S\rangle$, E_{ST}, is about 1 meV. From measurements of the tunnel rates [12], we estimate the ratio Γ_T/Γ_S to be on the order of 20. A similar ratio was found previously in transport measurements on a different device [13]. As can be seen in Fig. 8.1c, for $T_1 > 1$ ms this permits a read-out visibility $> 80\%$.

We implement the TR-RO by applying voltage pulses as depicted in Fig. 8.2b to gate P. Figure 8.2c shows the expected response of I_{QPC} to the pulse, together with the level diagrams in the three different stages. Before the pulse starts, there is one electron on the dot. Then, the pulse pulls the levels down so that a second electron can tunnel onto the dot ($N = 1 \rightarrow 2$), forming either a singlet or a triplet state with the first electron. The probability that a triplet state is formed is given by $3\Gamma_T/(\Gamma_S + 3\Gamma_T)$, where the factor of 3 is due to the degeneracy of the triplets. After a variable waiting time t_{wait}, the pulse ends and the read-out process is initiated, during which one electron can leave the dot again. The rate for tunneling off depends on the two-electron state, resulting in the desired spin-to-charge conversion. The QPC is used to detect the number of electrons on the dot. Due to the direct capacitive coupling of gate P to the QPC channel, ΔI_{QPC} follows the pulse shape. Tunneling of an electron on or off the dot gives an additional step in ΔI_{QPC} [2, 6, 14], as indicated by the arrows in Fig. 8.2c.

Now, Γ_S is tuned to 2.5 kHz, and Γ_T is therefore ≈ 50 kHz. In order to
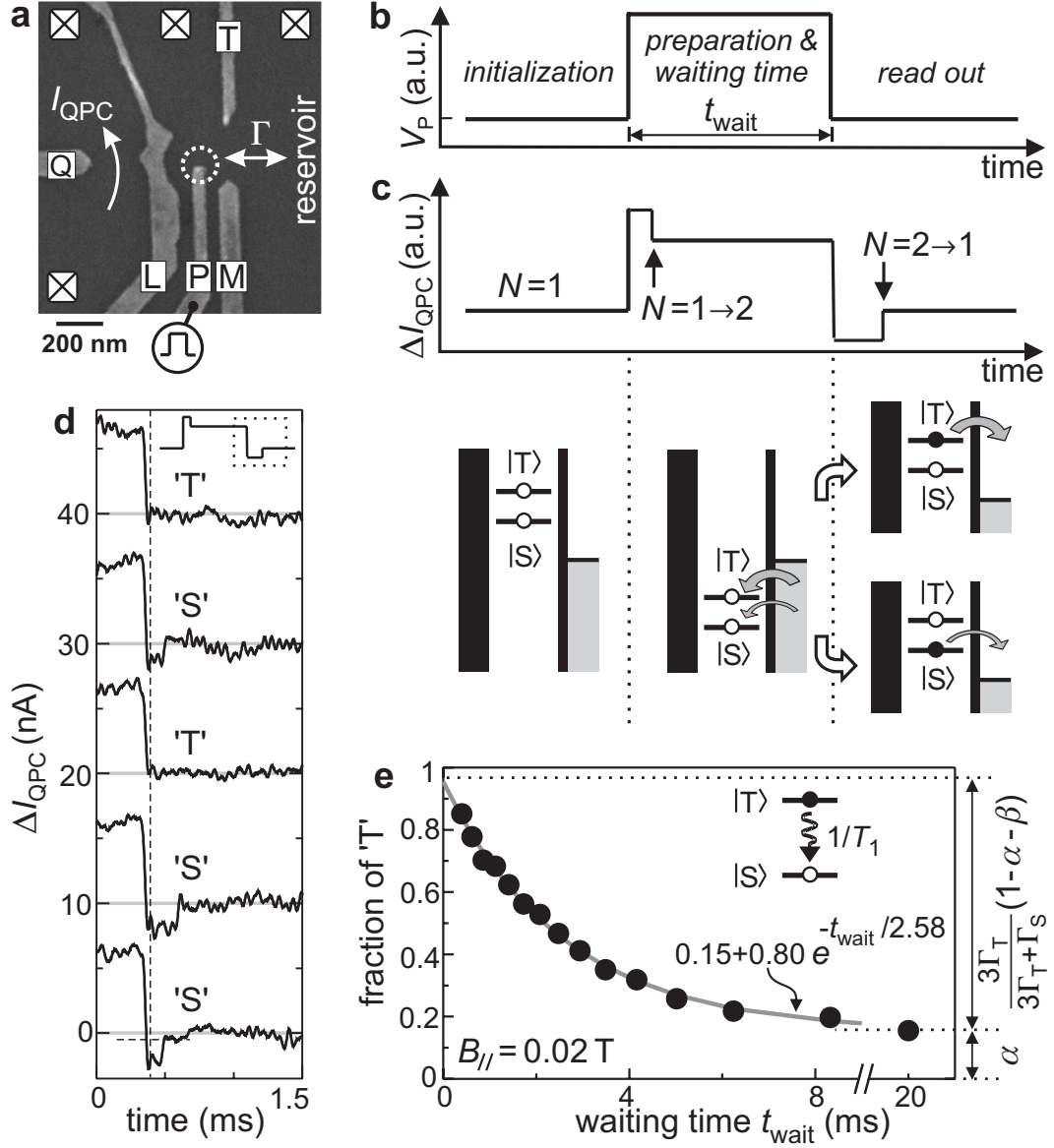
Figure 8.2: Single-shot read-out of $N=2$ spin states. (a) Scanning electron micrograph of a device as used in the experiments. (b) Pulse waveform applied to gate P. (c) Response of the QPC-current to the waveform of (b). Energy diagrams indicate the positions of the levels during the three stages. In the final stage, spin is converted to charge information due to the difference in tunnel rates for states $|S\rangle$ and $|T\rangle$. (d) Real-time traces of ΔI_{QPC} during the last part of the waveform (dashed box in the inset), for $t_{wait} = 0.8$ ms. At the vertical dashed line, N is determined by comparison with a threshold (horizontal dashed line in bottom trace) and the spin state is declared $'T'$ or $'S'$ accordingly. (e) Fraction of $'T'$ as a function of waiting time at $B_{//} = 0.02$ T, showing a single-exponential decay with a time constant T_1 of 2.58 ms.

achieve a good signal-to-noise ratio in I_{QPC}, the signal is sent through an external 20 kHz low-pass filter. As a result, many of the tunnel events from $|T\rangle$ will not be resolved, but the tunneling from $|S\rangle$ should be clearly visible.

Figure 8.2d shows several traces of ΔI_{QPC}, from the last part (300 μs) of the pulse to the end of the read-out stage (see inset), for a waiting time of 0.8 ms. In some traces, there are clear steps in ΔI_{QPC}, due to an electron tunneling off the dot. In other traces, the tunneling occurs faster than the filter bandwidth. In order to discriminate between $|S\rangle$ and $|T\rangle$, we first choose a read-out time τ (indicated by a vertical dashed line in Fig. 8.2d) and measure the number of electrons on the dot at that time by comparing ΔI_{QPC} to a threshold value (as indicated by the horizontal dashed line in the bottom trace of Fig. 8.2d). If ΔI_{QPC} is below the threshold, it means $N = 2$ and we declare the state $'S'$. If ΔI_{QPC} is above the threshold, it follows that $N = 1$ and the state is declared $'T'$. Our method for determining the optimal threshold value and read-out time is explained below.

To verify that $'T'$ and $'S'$ indeed correspond to the spin states $|T\rangle$ and $|S\rangle$, we change the relative occupation probabilities by varying the waiting time. The probability that the electrons are in $|T\rangle$, P_T, decays exponentially with the waiting time: $P_T(t) = P_T(0)\, e^{-t_{wait}/T_1}$. Therefore, as we make the waiting time longer, we should observe an exponential decay of the fraction of traces that are declared $'T'$.

We take 625 traces similar to those in Fig. 8.2d for each of 15 different waiting times. Note that the two-electron state is formed on a timescale (of order $1/\Gamma_T$) much shorter than the shortest t_{wait} used (400 μs). To find the optimal read-out parameters, we scan a wide range of read-out times and threshold values using a computer program. For each combination of these two parameters, the program determines the fraction of traces declared $'T'$ for each of the waiting times, and fits the resulting data with a single exponential decay $A\, e^{-t_{wait}/T_1} + \alpha$. The prefactor A is given by $3\Gamma_T/(\Gamma_S + 3\Gamma_T) \times (1 - \alpha - \beta)$. We see that A is proportional to the read-out visibility, and therefore the optimal read-out parameters can be determined simply by searching for the highest value of A. Here, we find the optimal values to be -0.4 nA for the threshold and 70 μs for τ (corresponding to $t = 370$ μs in Fig. 8.2d), and use these in the following.

In Fig. 8.2e, we plot the fraction of traces declared $'T'$ as a function of t_{wait}. We see that the fraction of $'T'$ decays exponentially, showing that we can indeed read out the two-electron spin states. A fit to the data yields a triplet-to-singlet relaxation time $T_1 = (2.58 \pm 0.09)$ ms, which is more than an order of magnitude longer than the lower bound found in Ref. [15]. As indicated on the right side of Fig. 8.2e, we can also extract α and β from the data. We find $\alpha = 0.15$ and

$\beta = 0.04$ (taking $\Gamma_T/\Gamma_S = 20$). The single-shot visibility is thus 81%. These numbers agree well with the values predicted by the model ($\alpha = 0.14$, $\beta = 0.05$, visibility= 81%), as indicated by the diamond in Fig. 8.1c. Note that, since the visibility is insensitive to τ near the optimal value, it is not significantly reduced by the finite bandwidth of the charge measurement.

As an extra check of the read-out, we have also applied a modified pulse where during the preparation only the singlet state is energetically accessible. Here, the read-out should ideally always yield $'S'$, and therefore the measured probability for finding $'T'$ directly gives us α. We find a fraction of $'T'$ of 0.16, consistent with the value of α obtained from the fit. This again confirms the validity of the read-out method.

8.4   Magnetic field dependence of the triplet-to-singlet relaxation

We further study the relaxation between triplet and singlet states by repeating the measurement of Fig. 8.2e at different magnetic fields $B_{//}$. Figure 8.3a shows the decay of the fraction of $'T'$, normalized to the fraction of $'T'$ at $t_{wait} = 0$, on a logarithmic scale. The data follow a single-exponential decay at all fields. Figure 8.3b shows the relaxation rate $1/T_1$ as a function of $B_{//}$. The dominant relaxation mechanisms for large values of E_{ST} are believed to originate from the
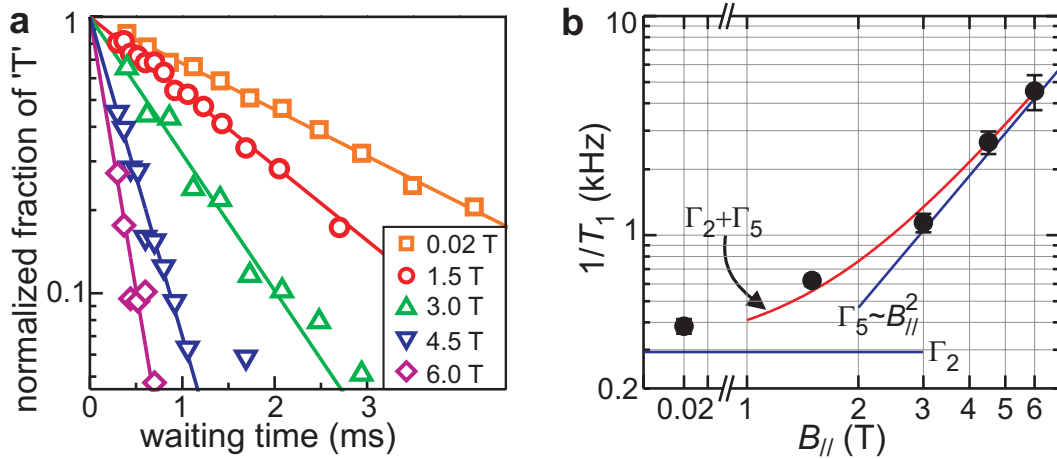
Figure 8.3: Triplet-to-singlet relaxation as a function of $B_{//}$. (a) Normalized fraction of $'T'$ vs. t_{wait} for different values of $B_{//}$. (b) Triplet-to-singlet relaxation rate $1/T_1$ as a function of $B_{//}$. The data is fit by a combination of a $B_{//}$-independent rate Γ_2 and a rate $\Gamma_5 \propto B_{//}^2$ (see text).

spin-orbit interaction [4, 16]. Ref. [16] predicts a B-independent rate Γ_2 that determines the low-B relaxation, and a Zeeman energy-related rate Γ_5, proportional to B^2, that dominates at higher B (we adopt the notation of Ref. [16]). Although the theory of Ref. [16] is based on single-spin flips, it can explain the two-electron relaxation data well. A fit to the data yields $\Gamma_2=(0.29\pm0.09)$ kHz and $\Gamma_5=(0.11\pm0.005)\cdot B_{/\!/}^2$ kHz, consistent with the prefactors found in Ref. [16]. A more extensive analysis of the relaxation data in both parallel and perpendicular field will be reported elsewhere.

8.5 Read-out of nearly degenerate states

Finally, we show that the TR-RO can still be used when $|S\rangle$ and $|T\rangle$ are almost degenerate. By mounting the device under a 45 degree angle with respect to the magnetic field axis, we can tune the singlet-triplet energy difference E_{ST} through zero [11]. In Fig. 8.4a we plot E_{ST} as a function of B, extracted from pulse spectroscopy measurements [12]. In these measurements, transitions are broadened both by the electron temperature in the reservoir and by fluctuations in the dot potential. We model these two effects by one effective electron temperature T_{eff}. For E_{ST} smaller than about 3.5 kT_{eff}, the energy splitting can not be resolved. As in previous transport and pulse spectroscopy measurements, we find here 3.5 $kT_{eff}\approx 60$ μeV (see inset of Fig. 8.4a), and therefore it is impossible to use the E-RO method beyond $B\approx 3.9$ T. From extrapolation of the data, we
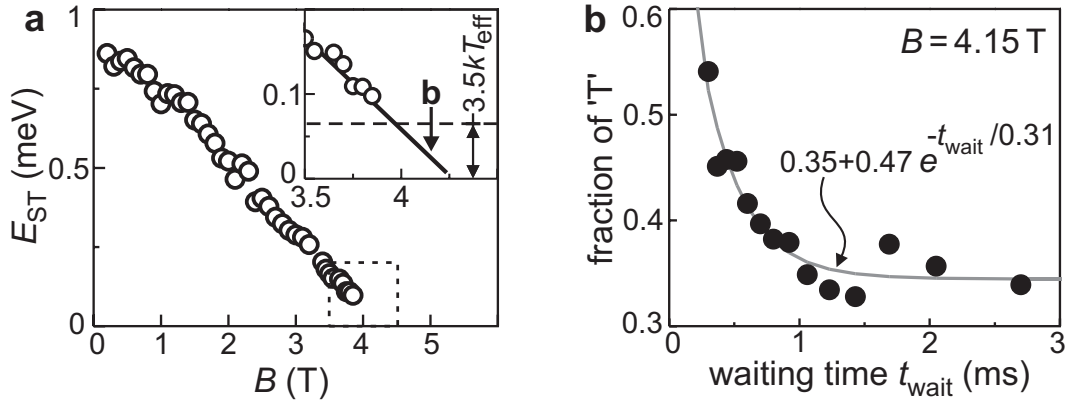
Figure 8.4: Single-shot read-out of nearly degenerate states. (a) Singlet-triplet energy difference E_{ST} as a function of magnetic field B, applied under a 45 degree angle with the 2DEG. Inset: zoom-in of the region inside the dashed square. For $B > 3.9$ T, E_{ST} is smaller than the effective electron temperature. (b) Single-shot read-out at $B = 4.15$ T. This field value is indicated with 'b' in the inset of (a).

find that the singlet-triplet ground state transition occurs at $(4.25 \pm 0.05)\,$T.

We tune B to 4.15 T (see inset of Fig. 8.4a), so that we are very close to the degeneracy point, but still certain that $|S\rangle$ is the ground state. Figure 8.4b shows the result of the read-out measurement at this field. Again, an exponential decay of the fraction of $'T'$ is observed, with a T_1 of (0.31 ± 0.07) ms. This demonstrates that even when the energy splitting E_{ST} is too small to resolve, we can still read out the spin states using TR-RO.

In future measurements, we plan to apply the tunnel-rate-selective read-out to detect relaxation and coherent manipulation of a single electron spin.

References

[1] D. Loss and D.P. DiVincenzo, Phys. Rev. A **57**, 120 (1998).

[2] J.M. Elzerman *et al.*, Nature **430**, 431 (2004).

[3] O. Astafiev *et al.*, Phys. Rev. B **69**, 180507(R) (2004).

[4] V. Golovach *et al.*, in preparation.

[5] S.W. Jung, T. Fujisawa, Y. Hirayama and Y. H. Jeong, Appl. Phys. Lett. **85**, 768 (2004).

[6] L. M. K. Vandersypen *et al.*, Appl. Phys. Lett. **85**, 4394 (2004).

[7] Similarly, spin-dependent tunneling to a second dot can be used, see H.A. Engel *et al.*, Phys. Rev. Lett. **93**, 106804 (2004).

[8] The probability β that no tunnel event has occurred at $t = \tau$, even though the initial state was $|ES\rangle$, is the sum of β_1, the probability that the state is $|ES\rangle$, and β_2, the probability that the state is $|GS\rangle$. These are given by:

$$\begin{aligned} \beta_1 &= e^{-(\Gamma_{ES}+1/T_1)\cdot\tau}, \\ \beta_2 &= \int_0^\tau P_{rel}(t) \cdot P_{GS}(\tau-t)\, dt. \end{aligned}$$

Here, $P_{rel}(t)\, dt$ is the probability that $|ES\rangle$ relaxes to $|GS\rangle$ within the time interval $[t, t + dt]$, and $P_{GS}(\tau-t)$ is the probability that no tunneling has taken place from $|GS\rangle$ during a time $\tau - t$:

$$\begin{aligned} P_{rel}(t) &= 1/T_1\, e^{-(1/T_1+\Gamma_{ES})\cdot t} \\ P_{GS}(\tau-t) &= e^{-\Gamma_{GS}\cdot(\tau-t)} \,. \end{aligned}$$

[9] M. Ciorga *et al.*, Phys. Rev. B **61**, R16315 (2000).

[10] M. Ciorga *et al.*, Appl. Phys. Lett. **80**, 2177 (2002).

[11] L. P. Kouwenhoven, D. G. Austing, and S. Tarucha, Rep. Prog. Phys. **64** (6), 701 (2001).

[12] J. M. Elzerman *et al.*, Appl. Phys. Lett. **84**, 4617 (2004).

[13] R. Hanson *et al.*, to be published in the Proceedings of the XXXIXth Rencontres de Moriond (La Thuile, 2004) "Quantum information and decoherence in nanosystems"; cond-mat/0407793.

[14] R. Schleser *et al.*, Appl. Phys. Lett. **85**, 2005 (2004).

[15] T. Fujisawa *et al.*, Nature **419**, 278 (2002).

[16] A.V. Khaetskii and Y.V. Nazarov, Phys. Rev. B **61**, 12639 (2000).

Chapter 9

Quantum computing with electron spins: current status and future directions

R. Hanson, J. M. Elzerman, L. M. K. Vandersypen,
L. H. Willems van Beveren, F. H. L. Koppens, I. T. Vink,
and L. P. Kouwenhoven

In this chapter, we review the progress towards the implemention of qubits with electron spins confined in semiconductor quantum dots. Three out of the five criteria for a scalable quantum computer have already been satisfied. We summarize current theoretical insight on the decoherence mechanisms and discuss the expected fidelity of the quantum gates. Finally, we present concrete ideas on how to proceed towards coherent spin operations and two-qubit operations and explore the possibility of a Bell test.

9.1   Current status: the DiVincenzo criteria

The work in described in this thesis is motivated by Loss and DiVincenzo's proposal to use electron spins confined in semiconductor quantum dots as spin qubits [1]. In chapter 1 we have outlined the basic ingredients of this proposal. We now consider the five criteria of DiVincenzo's checklist [2], which must *all* be satisfied for any physical implementation of a quantum computer:

    I   A scalable physical system with well-characterized qubits

    II   Initialization of the qubits to a known (pure) state

    III   Qubit read-out

    IV   Long coherence times

    V   A universal set of quantum gates

In this section, we will review the experimental progress on the spin qubit proposal using these five criteria.

9.1.1   Scalable physical system with well-characterized qubits

To start with, a scalable physical system with well-characterized qubits is needed. Well-characterized means that we know the properties of the system in which the qubit is encoded, the presence of and coupling to other states of the system, the interaction with other qubits, and the coupling to external control parameters.

In our case, the qubit is encoded in the spin orientation of a single electron in a static magnetic field B_0, where $|\uparrow\rangle$ serves as the logic $|0\rangle$, and $|\downarrow\rangle$ corresponds to the logic $|1\rangle$. The electron spin can not take on any value outside the two-dimensional Hilbert space spanned by $|\uparrow\rangle$ and $|\downarrow\rangle$. The interaction with other qubits and the coupling to external control fields will be discussed below in section 9.1.5.

Since the spin is carried by an electron confined in a quantum dot, we need to characterize this quantum dot as well. We have shown in chapter 3 that we can isolate a single electron in each of two coupled quantum dots [3]. The conventional way of characterizing dots is to measure the current through the dot as a function of applied bias voltage [4]. The smallest current that we can resolve is about 16 fA, which sets a lower bound on the tunnel rate to the reservoir, Γ, of about 16 fA/e= 100 kHz. For $\Gamma < 100$ kHz, we can use the charge detection technique [5] developed in chapters 3 and 6 [3, 6], where a nearby Quantum Point Contact (QPC) serves as an electrometer. Here the limitation arises from

the bandwidth of our charge detection setup. This bandwidth can be extended by increasing the electrostatic coupling of the QPC to the dot using a different gate design [7]. Further improvements can achieved by using a 'radio-frequency QPC' (RF-QPC), similar to the well-known RF-SET [8]. In this approach, the QPC is embedded in an LC circuit with a resonant frequency of ~ 1 GHz. By measuring the reflection or transmission of a resonant carrier wave, it is estimated that it should be possible to read out the charge state of the nearby quantum dot in ~ 1 μs, an order of magnitude faster than is currently attainable [9].

Both techniques allow a measurement of the absolute number of electrons on the dot, the discrete energy spectrum and the tunnel rate to the reservoir for the different transitions, thus providing a full characterization of a single quantum dot. We have used both techniques to identify the two basis states of the qubit, $|\uparrow\rangle$ and $|\downarrow\rangle$, and measure their energy splitting [6, 10] (see chapters 4 and 6).

The coupling between two quantum dots can be separated into a capacitive coupling and a tunnel coupling. The capacitive coupling can be easily inferred from the charge stability diagram [11]. The tunnel coupling can also be deduced from the stability diagram, either from the curvature of the lines in the "honeycomb" diagram (see e.g. Ref [12]) or from the charge distribution near the anti-crossing of the two single-dot ground states [13]. A more accurate value for the tunnel coupling can be found by performing photon-assisted tunneling spectroscopy. Here, microwaves induce transitions between the bonding and the anti-bonding state only when the photon energy equals the energy splitting between these two states, which is a simple function of the tunnel coupling. This method has been demonstrated both for transport measurements [14] and for measurements using only charge detection [13]. The double-dot exchange splitting J can in principle be determined from spectroscopy measurements [15], but in the regime of interest ($J \sim 1 - 30$ μeV) we might not be able to resolve it due to thermal broadening. The value of J can always be found from the frequency of the two-spin oscillation (see section 9.3.1).

We will finally remark on the requirement of scalability. In order to create a quantum computer consisting of, say, several hundreds of qubits, major revisions in the design and use of different fabrication techniques will most probably be necessary. We do not concern ourselves now with a possible large-scale quantum computer, but instead focus on studying decoherence and demonstrating basic quantum algorithms. For this, a circuit containing about five to ten qubits is sufficient for the near future. Our present circuit can be extended to incorporate several more quantum dots, by making minor adjustments to the design of the surface gates. Note that the charge detection schemes offer a substantial advantage here, since these only require the dot to be coupled to a single reservoir.

9.1.2   Initialization to a known pure state

Initialization of the qubits to a known pure state is required for two reasons. First, before the start of the computation the qubits have to be initialized to a known value. Second, for quantum error correction a continuous supply of (ancillary) qubits in a known pure state is needed [2].

Initialization of the spin to the pure state $|\uparrow\rangle$ – the desired initial state for most quantum algorithms [16] – can be achieved by waiting so long that energy relaxation will cause the the spin on the dot to relax to the $|\uparrow\rangle$ ground state (Fig. 9.1a). This is a very simple and robust initialization approach, which can be used for any magnetic field orientation (provided that $g\mu_B B > 5k_B T$). As it takes about $5T_1$ to reach equilibrium, it is also a very slow procedure, which might become problematic at the stage of quantum error correction [2].

A faster initialization method is to place the level $|\uparrow\rangle$ below and $|\downarrow\rangle$ above the Fermi energy of the reservoir (as in Fig. 9.1b). Then, a spin-up electron will stay on the dot, whereas a spin-down electron will tunnel out to the leads, to be replaced by a spin-up. After waiting a few times the sum of the typical tunnel times for spin-up and spin-down ($\sim 1/\Gamma_\uparrow + 1/\Gamma_\downarrow$), the spin will be with large probability in the $|\uparrow\rangle$ state. This initialization procedure can therefore be fast. A disadvantage is that the Zeeman energy splitting needs to be much larger than the electron temperature in the leads.

A third possibility is to initialize using the large spin selectivity in the tunnel rates, i.e. $\Gamma_\uparrow \gg \Gamma_\downarrow$, which is present in a perpendicular field due to the spatial separation of the spin-resolved edge channels [17, 18]. Here, we first empty the
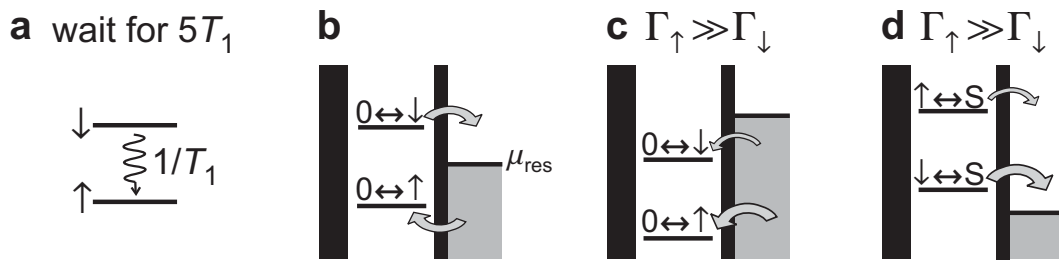
Figure 9.1: Different methods for initialization to (a)-(c)$|\uparrow\rangle$ and (d) $|\downarrow\rangle$. **(a)** Spin relaxation at a rate $1/T_1$ gives the state $|\uparrow\rangle$ after $\sim 5T_1$. **(b)** Energy-selective tunneling leads to $|\uparrow\rangle$ after a time $\sim 1/\Gamma_\uparrow + 1/\Gamma_\downarrow$. We use here explicit notations for the transitions between the zero-electron state and the one-electron spin states to avoid confusion with the transitions used in (d). **(c)** If $\Gamma_\uparrow \gg \Gamma_\downarrow$, tunneling into an empty dot will result in $|\uparrow\rangle$ with a probability $\Gamma_\uparrow/(\Gamma_\uparrow + \Gamma_\downarrow)$. **(d)** Initialization to $|\downarrow\rangle$ for $\Gamma_\uparrow \gg \Gamma_\downarrow$ by starting from the two-electron singlet state, denoted here by S.

dot, and then position both spin levels below μ_{res} (see Fig. 9.1c). The electron that will tunnel in will have spin-up with probability $\Gamma_\uparrow/(\Gamma_\uparrow + \Gamma_\downarrow)$, which is very close to unity for high spin selectivity.

For verifying read-out procedures and testing two-qubit operations (see section 9.3.1), we also need the ability to initialize to the spin-down state. The most straight-forward method is to initialize to $|\uparrow\rangle$ and rotate the spin by 180 degrees. However, controlled rotation of a single spin on a quantum dot has not yet been demonstrated. Fortunately, there are other ways to initialize to $|\downarrow\rangle$. If the tunnel rates are spin-selective as mentioned above, we can start from a two-electron singlet state $|S\rangle=(|\uparrow\downarrow\rangle-|\downarrow\uparrow\rangle)/\sqrt{2}$, and allow one electron to tunnel off the dot. Since $\Gamma_\uparrow \gg \Gamma_\downarrow$, the probability that the tunneling electron has spin-up and therefore the remaining electron has spin-down is $\Gamma_\uparrow/(\Gamma_\uparrow + \Gamma_\downarrow)$ (see Fig. 9.1d). Thus, we can initialize to $|\uparrow\rangle$ and $|\downarrow\rangle$ with the same high fidelity.

In the absence of spin-selectivity in the tunnel rates we can not initialize to $|\downarrow\rangle$, but we can initialize to a mixed state where the electron is probabilistically in $|\uparrow\rangle$ or $|\downarrow\rangle$, by first emptying the dot and then positioning both spin levels below μ_{res} (see chapter 7). The dot is then randomly filled with either a spin-up or a spin-down electron.

9.1.3   Qubit read-out

Read-out determines the result at the end of the computation by measuring specific qubits. Many proposals exist for reading out the electron spin state on a quantum dot (see chapter 7 for an extensive list of references). In this thesis, we have demonstrated two methods. In both of them, the spin information is first converted to charge information, by making the number of electrons on the dot, N, dependent on the original spin state.

The first approach makes use of the large Zeeman energy splitting induced by an in-plane magnetic field. Here, the two spin levels are positioned such that an electron can tunnel off the dot only if it carries the high-energy spin (as in Fig. 9.1b). This is followed by real-time detection of single-electron tunneling events using the QPC as an electrometer. We have used this method in chapter 7 to perform single-shot read-out of the spin of a single electron [19]. Here, the measurement visibility was $\sim 65\%$ at 10 T, limited mostly by the ~ 40 kHz bandwidth of our current measurement setup, and also by thermal excitation of electrons out of the quantum dot, due to the (in this experiment) high effective electron temperature of ~ 300 mK. We estimate that we can improve the visibility of this energy-selective read-out (E-RO) technique to more than 90% by lowering the electron temperature below 100 mK, and especially by using a faster way to

measure the charge on the dot (see section 9.1.1).

The second method that we have studied makes use of a difference in *tunnel rate* between the spin states. To read out the spin orientation of an electron on the dot, we simply raise both dot levels above μ_{res}, so that the electron can leave the dot. If the tunnel rate for spin-up electrons, $\Gamma_\uparrow$, is much larger than that for spin-down electrons, $\Gamma_\downarrow$, then after a time τ, where $\Gamma_\downarrow^{-1} \gg \tau \gg \Gamma_\uparrow^{-1}$, the dot will have a large probability to be already empty if the spin was up, but a very small probability to be empty if the spin was down. Measuring the charge on the dot at $t = \tau$ thus reveals the original spin state. In chapter 8 this tunnel-rate-selective read-out (TR-RO) method is used to read out the two-electron spin state, achieving a single-shot visibility of 81% [23]. We plan to use TR-RO also for a single electron by applying the magnetic field perpendicular to the 2DEG, so that $\Gamma_\uparrow \gg \Gamma_\downarrow$ [17, 18].

As explained in chapter 8, TR-RO has some important advantages over E-RO. In contrast to E-RO, TR-RO does not require a large energy splitting between the spin states, it is robust against background charge fluctuations and is insensitive to photon-assisted tunneling. Which of the two read-out methods is preferable will also depend on the specific demands of the particular experiment.

9.1.4   Long coherence times

The electron spin was proposed as a candidate for a qubit, because the spin state was believed to be very stable. Relaxation measurements on a single spin (chapter 7 and Ref. [20]) and on two-electron spin states (chapter 8) have shown long spin relaxation times up to several milliseconds, suggesting that indeed the spin is only weakly perturbed by the environment. In contrast, the orbital degree of freedom of electrons has been measured to decay on a 10 nanosecond timescale [21], which is five orders of magnitude faster than the spin relaxation. The true figure of merit for quantum computing, however, is the coherence time.

The timescale on which the coherence is maintained, i.e. on which the evolution of the qubit state does not deviate from the desired route (set by the internal Hamiltonian plus the control fields), is denoted by T_2. To avoid confusion here, we explicitly define T_2 to be the coherence time during free evolution of the qubit. (The coherence time can be longer when the qubit is undergoing Rabi oscillations, because (i) the oscillations have a refocusing effect and (ii) the spin is nearly parallel to the field for about half the time, such that decoherence is less effective [22]). Note that the coherence time merely reflects the lack of knowledge that we have about (the interaction of the qubit with) the environment or the inability to compensate for this interaction. Therefore, the coherence time can be

extended by increasing the knowledge of or the control over (a part of) the environment. Also, decoherence mechanisms that are constant on a timescale much longer than the typical qubit operation time can be canceled out by spin-echo and composite pulses techniques, provided that the coherence time still allows a full rotation to be performed [22].

In principle, loss of coherence can be entirely compensated for by performing quantum error correction [16]. It is estimated that if the error per operation is 10^{-4}, error correction can be successful and arbitrarily long computations can be performed. (This ratio is sometimes referred to as the 'accuracy threshold'). It implies that also T_2 has to be at least 10^4 times larger than the gate operation time.

The value of T_2 for a single electron spin in a GaAs quantum dot has not yet been measured. For electrons in bulk n-type GaAs, an ensemble-averaged measurement has yielded a spin decoherence time T_2^* of 100 ns [24]. This number has long been interpreted as a lower bound for the T_2 of electron spins on a quantum dot, i.e. $T_2 \geq T_2^*$. As we will see below, this is not correct.

Over the past few years, theoretical insight into the electron spin relaxation and decoherence mechanisms has increased enormously. At present, the dominant mechanisms are believed to be the spin-orbit interaction [25, 26], and the hyperfine interaction with the nuclei [27, 28, 29, 30]. Recent theory suggests that the spin-orbit interactions, in leading order, do not affect the transverse components of the spin [26]. This would imply that the spin-orbit limited coherence time can not be shorter than the relaxation time T_1. In contrast, the nuclear spin system is expected to have a much more severe impact on T_2 than on T_1.

The hyperfine interaction of the electron spin with the surrounding nuclear spins leads to an additional effective magnetic field B_{nucl}, the so-called Overhauser field. The polarization of the nuclei will usually be negligible in our experiments and thus the absolute value of B_{nucl} will be small compared to the external field B_0. Anyway, a static polarization just adds a constant offset to B_0 and thus has no effect on the coherence. In contrast, the *fluctuations* in B_{nucl}, denoted ΔB_{nucl}, cause uncertainty in the total effective magnetic field and can therefore lead to significant decoherence of the electron spin. In zero external magnetic field, there are three characteristic timescales connected to B_{nucl}: the period of the electron precession in ΔB_{nucl}: τ_1, the period of the nuclear spin precession in the hyperfine field of the electron, which changes the orientation of ΔB_{nucl}: τ_2, and the nuclear spin relaxation time in the dipole-dipole field of its nuclear neighbors: τ_3.

The first and shortest timescale, τ_1, is set by the value of the statistical variation of B_{nucl}: $\Delta B_{nucl} \sim A/(\sqrt{N_{nucl}}g\mu_B)$, where A is the hyperfine constant ($A =$

90 μeV in GaAs [31]), and N_{nucl} is the number of nuclei with which the electron interacts. It leads to a precession period of $\tau_1 \sim h\sqrt{N_{nucl}}/A$. For $N_{nucl}=10^5$, we have $\Delta B_{nucl} \sim 10$ mT and thus τ_1 is about 15 ns. Note that we regard the nuclear field to be 'frozen' on this timescale.

Secondly, ΔB_{nucl} varies in time due to the precession of the nuclear spins in the hyperfine field of the electron. The effective magnetic field that the nuclei feel is proportional to the square of the electron wave function at the position of the nucleus. Since the wave function is not constant over the dot, nuclei at different positions experience different hyperfine fields and thus precess with different frequencies leading to a slow variation in ΔB_{nucl}. (Note that the electron precesses much faster than the nuclei and therefore the nuclei see only a time-average of the hyperfine field of the electron). In Ref. [29] the timescale on which ΔB_{nucl} changes is estimated to be 1 μs.

The situation changes drastically when a large external magnetic field is applied. Now, both the electron spin and the nuclear spins will effectively precess around the external field. Therefore, the component of the nuclear spins along the magnetic field will not change due to precession in the hyperfine field of the electron. Furthermore, since the electron spin is directed along the strong external field, it is much less sensitive to fluctuations in the transverse direction. The conclusion is that in the case of a strong magnetic field the second timescale becomes very long and the third timescale, τ_3, becomes important. This timescale results from changes in the nuclear field due to dipole-dipole interactions. It is estimated to be about 100 μs [28, 29], and presents an upper bound on the spin decoherence time T_2. In fact, T_2 would approach τ_3 if the value of B_{nucl} would be known exactly. In practice however, B_{nucl} is not known, and the relevant decoherence time is τ_1. We thus expect T_2 to be on the order of 10 ns.

How can this number be reconciled with the T_2^* of 100 ns obtained for electron spins in bulk GaAs [24]? The answer lies in the number of nuclei with which the electron interacts. The wave function of an electron in the bulk is spread out, whereas the electron in the dot is confined to a disk of about 35 nm diameter. Therefore, an electron in the bulk interacts with many more nuclei, and since $\Delta B_{nucl} \propto 1/\sqrt{N}$ this leads to a much lower decoherence rate. We can conclude that the coherence time measured in the bulk (or in a 2DEG) can not be considered as a lower bound for T_2 of an electron on a quantum dot.

These considerations should be taken as a strong incentive to study the behavior of the nuclei in more detail experimentally. Pioneering experiments in the group of Prof. Tarucha at the University of Tokyo have already uncovered some intriguing physics, occurring when electron transport through a vertical double dot is spin-blocked due to the Pauli exclusion principle [32]. Very recently, the

Pauli spin blockade was also observed in a lateral system in the group of Prof. Marcus at Harvard [33]. Since this lateral system allows more parameters to be tuned *in situ*, further exciting results can be expected.

The quest in the next years will be for a means to 'turn off' the fluctuations in the nuclear system on longer timescales. Since the decoherence arising during the precession of the electron spin in one nuclear configuration can be exactly canceled by a precession in the opposite nuclear configuration, flipping all nuclear spins with a period much faster than τ_1 will greatly prolong the coherence. Alternatively, if the electron spin can be manipulated on timescales much shorter than τ_1, composite pulse techniques can be used [22]. In these cases, coherence can be preserved for a time τ_3 (about 100 μs). One ultimate possibility is to completely polarize the nuclear spin system, thus eliminating all fluctuations. Also, we can think of isolating the electron spin in a different host material where the nuclei possess no spin. Most notably, SiGe quantum wells and carbon nanotubes can in principle be purified to contain only spinless nuclei. These systems might one day exhibit the same excellent control over single-electrons that we have right now in GaAs structures.

To put the value of the coherence time in perspective, we need to compare it to the gate operation time, which we will estimate in the next section.

9.1.5 A universal set of quantum gates

A set of quantum gates is called universal if every unitary operation on an arbitrary number of qubits can be decomposed into combinations of only these quantum gates. It has been proved that full single-qubit control combined with the two-qubit 'quantum XOR' (or 'CNOT'), suffice to implement all possible quantum algorithms [16].

For electron spins in quantum dots, both the single-qubit control fields as well as the interactions between neighboring qubits can be completely turned on and off at will. The two-qubit CNOT can be implemented by a combination of single-qubit rotations and two-spin exchange interactions [34]. In fact, the exchange interaction is even universal by itself, i.e. without single-qubit rotations, when the state of each qubit is encoded in the state of three electron spins [35].

We consider two schemes for single-spin rotations. In one approach, an oscillating magnetic field B_{ac} is applied perpendicular to the static field B_0 at the Larmor frequency $g\mu_B B_0/h$. This induces spin rotations at a rate $f_{Rabi} = g\mu_B B_{ac}/h$, which is about 6 MHz for $B_{ac} = 1$ mT. This well-known electron spin resonance (ESR) technique has already been applied in the 1980s to GaAs/AlGaAs 2DEG electrons in the Quantum Hall regime (see e.g. Ref [36]). At dilution fridge

temperatures, it is hard to reach values of B_{ac} exceeding 5 mT using current technology (see section 9.2.1). If we assume $B_{ac} < 5$ mT, then $f_{Rabi} < 30$ MHz and the single-qubit gate operation time will be at least $1/2 f_{Rabi} \sim 15$ ns. As we have argued in the previous section, T_2 might be of the same order. Our efforts to demonstrate single-spin ESR will be discussed in section 9.2.

Alternatively, a spin rotation can be achieved by modulating the value of the electron g-factor at the Larmor frequency. This so-called g-tensor modulation has been experimentally demonstrated on electrons in an AlGaAs/GaAs/AlGaAs quantum well [37]. Here, a voltage on a backgate pulls the electron wave function from the GaAs central region, where g is -0.44, into the AlGaAs barrier region, where g is +0.4 [38]. Due to the anisotropy of the g-factor in these quantum wells, the orientation of the effective magnetic field also changes. By applying an oscillating electrical signal at the Larmor frequency to the backgate, the spin of electrons in the quantum well could be tipped by 2 degrees. For a single electron in a quantum dot, such oscillating electric fields might induce unwanted effects like photon-assisted tunneling. Furthermore, increasing the anisotropy such that it can produce rotations of 180 degrees seems challenging. Therefore, the ESR approach is likely to yield the first experimental demonstration of single-spin rotations and provide a value for T_2. Control over the g-factor might become useful to bring individual electron spins into resonance with a 'global' ESR field.

Two-spin operations are mediated by the exchange interaction, which leads to an effective Heisenberg Hamiltonian $J \vec{S}_1 \cdot \vec{S}_2$. Here, J is the strength of the exchange interaction and $\vec{S}_1$ and $\vec{S}_2$ denote the two spins. The value of J is related to the overlap of the electron wave functions, which varies exponentially with the voltage applied to the gate controlling the inter-dot tunnel barrier. Thus, by applying a (positive) voltage pulse with a certain amplitude and duration, we can temporarily turn on the exchange interaction. The two-spin operations are discussed in more detail in section 9.3.

The shortest electrical pulses applied to surface gates that can be precisely controlled are on the order of 100 ps [39], corresponding to a value of $J/h \sim 5$ GHz (for completely swapping the spin states). During the gate operation, fluctuations in the tunnel rate due to charge noise can lead to additional decoherence. It has been shown recently that background charge noise has only a very weak effect on the tunnel rate to the reservoir [40]. However, it can also lead to misalignment of the two single-dot levels, which will enhance J [41]. Since there are many factors that possibly influence the background charge noise, it is difficult to capture its effect on the coherence in a single number.

As in the case of a single spin, the nuclei can pose a significant threat: different Overhauser fields on the two dots (ΔB_{nucl} on the order of 10 mT) lead to a

difference in the effective spin splitting δE of about 0.3 μeV. The error induced by δE is $(\delta E/2J)^2$ [42]; thus we can make the error small by performing the operation within a short time. For $J=$ 20 μeV (5 GHz), the error is of order 10^{-4}.

Concluding, current insight suggests that the single-qubit gate operation time (with our present technology in GaAs) is of the same order as the expected T_2. Single-qubit operation time might be drastically shortened using new electrical or optical techniques. For two-spin operations, the gate operation time could well be much shorter. If the decoherence rate turns out to be the same for one- and two-qubit operations, the two-qubit gate will be much closer to the accuracy threshold. In that case, the scheme where one qubit is encoded in the state of three electron spins [35] is more attractive than the original single-spin proposal [1], as single-spin rotations can then be completely left out.

9.1.6   Summary of the current status

Out of the five criteria for a scalable quantum computer, three have already been satisfied: well-defined qubits, initialization and read-out. Theoretical considerations suggest that the single-qubit operation time might be of the same order as the coherence time due to the hyperfine interaction with the nuclei, while for the two-spin operations the gate operation time is possibly much smaller.

Future experiments will focus on measuring the coherence time via the coherent manipulation of single spins and the coherent coupling and manipulation of spins in neighboring dots. In the next sections we will discuss these two research paths in more detail.

9.2   Single-spin rotations

In this section, our approach to the coherent rotation of a single electron spin using the above-mentioned ESR principle is outlined. We first discuss the on-chip generation of the required microwave field. Then we propose and critically analyze several schemes for the detection of ESR.

9.2.1   On-chip generation of the oscillating magnetic field

Excitation of ESR microwave magnetic fields commonly relies on microwave cavities, but unfortunately, a lot of power is dissipated in metallic cavities: for a rectangular cavity with a high Q-factor of 10^4, the power dissipation is over 1 Watt

for $B_{ac} = 1$ mT at $f_0 = 30$ GHz and still about 100 μW for $B_{ac} = 0.01$ mT [43]. Superconducting cavities are not an option since B_0 is too large.

Instead, we intend to generate the oscillating magnetic field by sending an alternating current through an on-chip wire running close by the dot, as shown in Fig. 9.2a. Depending on the orientation of the static magnetic field that we prefer, the wire can be located next to the dot (for an in-plane magnetic field) or on top of the dot (for an in-plane or a perpendicular field). In the latter case, an insulating layer will separate the wire from the surface gate structure.

If the wire is placed well within one wavelength (which is a few mm at 30 GHz near the surface of a GaAs substrate) from the quantum dot, the dot is in the near-field regime and the electric and magnetic field distribution produced by the AC current should be the same as for a DC current [43]. The linearly oscillating field can be decomposed into a clockwise and an anti-clockwise component rotating at the same frequency. In the rotating frame, one of these components will be static (the resonant component), while the other one will be far off-resonance and can be disregarded. Note that this implies that only half of the applied oscillating field is actually effective. For a distance between the edge of the (500 nm wide and 200 nm high) wire and the centre of the dot of 200 nm, a current of ~ 2.5 mA should generate a magnetic field of about 1 mT and no electric field at the position of the dot [44, 45]. To minimize reflection and radiation losses, the wire is designed
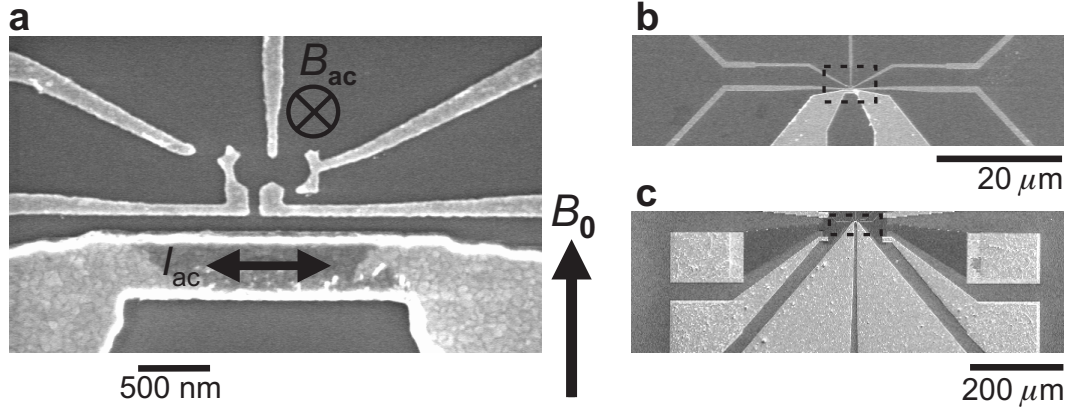
Figure 9.2: Scanning electron micrographs showing of the on-chip gold wire to apply microwaves to a nearby double quantum dot. This device was fabricated by Wouter Naber. **(a)** An AC current through the wire, I_{ac}, generates an oscillating magnetic field, B_{ac}, perpendicular to the plane. If the AC frequency is resonant with the Zeeman splitting induced by a large static in-plane magnetic field, B_0, an electron spin on the dot will rotate. **(b)-(c)** Zoom-outs of (a), showing the coplanar stripline which is designed to have 50 Ω impedance.

to be a shorted coplanar stripline (Fig. 9.2b) with a 50 Ω impedance. The total dissipation of the on-chip section (Au wire + Au waveguide) is estimated to be on the order of 10 μW for an oscillating field of 1 mT [45], which is well below the thermal budget at the mixing chamber of the dilution refrigerator (about 300 μW at 100 mK). For a field of 5 mT, the dissipation increases to about 250 μW.

9.2.2   Detection of Continuous Wave ESR

In the simplest schemes for detecting ESR, the microwave field B_{ac} is continuously on. Engel *et al.* have proposed a setup in which spin rotations on the dot [46] lead to a current flowing through the dot. This scheme is depicted in Fig. 9.3a-b for a single electron on the dot. If the ESR field is off resonance, the dot is in its ground state $|\uparrow\rangle$ and there is no current due to Coulomb blockade (Fig. 9.3a). In contrast, if the ESR field rotates the spin on the dot to $|\downarrow\rangle$, the electron has enough energy to escape to the right lead (Fig. 9.3b). A resonant current now flows via $|\downarrow\rangle$ until $|\uparrow\rangle$ becomes occupied. The current is then again blocked until the spin is rotated. In Fig. 9.3c a simulation (using the model of Ref. [46]) shows the expected current trace versus gate voltage, for two different values of B_{ac}. From the linewidth in frequency (or magnetic field) of the resonance, a lower bound on the single-electron T_2 can be derived.

A similar setup has been proposed where the ESR-induced change in the average occupation of the dot is measured [47]. Recently, measurement of a spin resonance signal using this setup from an electron in a Si MOSFET impurity trap has been reported [48].

Although these schemes are conceptually simple, it is quite hard to prove that a signal in the current as shown in Fig. 9.3c is indeed due to single-spin rotations on the dot. We discuss here two relevant parasitic effects that can lead to a similar resonance feature.

First, it is virtually impossible to completely eliminate the electrical component of the oscillating field. This electrical component can induce a photon-assisted tunnel event from $|\uparrow\rangle$ to the leads (see Fig. 9.3d). This so-called photo-ionization process leads to exactly the same situation as in Fig. 9.3b. Also, for even higher electric fields a current can flow where every tunnel event involves photon-absorption (pure photon-assisted tunneling). This will induce peaks on both sides of the main peak.

Second, if the ESR resonance frequency of electrons in the *leads* is the same as the expected resonance frequency for the electron on the dot (see Fig. 9.3e), a current will flow through the dot independent of whether the spin on the dot is actually rotated. Clearly, under these conditions there is no way to prove that
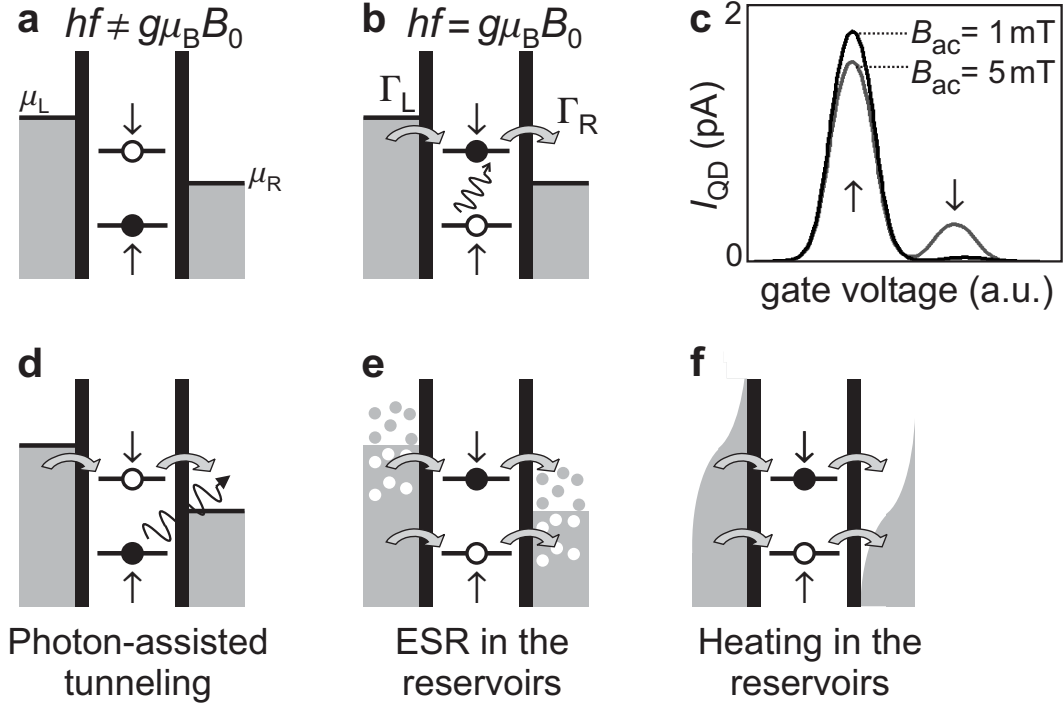
a $hf \neq g\mu_B B_0$ **b** $hf = g\mu_B B_0$ **c**

d Photon-assisted tunneling **e** ESR in the reservoirs **f** Heating in the reservoirs

Figure 9.3: Detection of Continuous Wave (CW) ESR. **(a)-(b)** Scheme for detecting CW ESR. **(a)** The electron can not leave the dot if it is in in $|\uparrow\rangle$. **(b)** If the electron is in $|\downarrow\rangle$ due to a spin rotation, it can tunnel off the dot and contribute to the current. **(c)** Simulation of the expected current as a function of gate voltage, using the model of Ref. [46]. The symbols $\uparrow$ and $\downarrow$ indicate the gate voltage at which the levels for $\uparrow$ and $\downarrow$ lie within the bias window (i.e. are between μ_L and μ_R). The ESR-induced peak is about 20 fA (400 fA) for $B_{ac}= 1$ mT (5 mT). We have used the following parameter values: $T_1=1$ ms, $T_2=100$ ns, $\Gamma_L=50$ MHz, $\Gamma_R=15$ MHz, $B_0=5$ T. Curves similar to (c) can result from the unwanted effects of **(d)** photon-assisted tunneling, **(e)** ESR in the reservoirs, or **(f)** heating of the electrons in the reservoir.

spin rotations occur on the dot. (A similar effect is present when the electrons in the leads are heated by the microwave field (Fig. 9.3f), but the frequency and magnetic field dependence of the heating process and ESR will generally be different). Both the photo-ionization process and ESR in the reservoirs can not be circumvented by changing the magnetic field, making single-spin ESR on the dot hard to prove.

9.2.3 Detection of pulsed ESR

The problems mentioned in the previous section can be avoided by separating the spin rotation and the read-out in time: B_{ac} is turned on when the levels are

well in the Coulomb blockade regime, and B_{ac} is off when the spin state is read out. In between, we allow enough time for any excitation in the reservoirs to disappear (note that the relaxation times in the leads are much shorter than T_1 on the dot). This way, photon-assisted tunneling does not provide enough energy for the electron to tunnel out, and the read-out is performed when the reservoirs are (again) in thermal equilibrium.

In the long run, we would like to combine ESR with single-shot read-out. In order to find the resonance condition and obtain first evidence of single-spin rotation, it is more convenient and much faster to apply a voltage pulse train and measure the read-out signal averaged over many cycles. In Fig. 9.4a we show the pulse amplitude V_P and the amplitude of the microwave field B_{ac} as a function of time. The spin is rotated when the levels are in Coulomb blockade (Fig. 9.4b). After the spin rotation, some time is allowed for the excitations in the leads to disappear (Fig. 9.4c). Then the levels are brought into the read-out configuration. In the transport scheme of Fig. 9.4d, the electron can tunnel out and contribute to the current only if its spin has been rotated. The two read-out configurations shown in Figs. 9.4e and 9.4f both rely on charge detection with the QPC. In the scheme of Fig. 9.4e, an electron can tunnel off the dot only if its spin was rotated. Thus, temporarily the number of electrons will be zero, reducing the average charge on the dot, which in turn affects I_{QPC}. In the scheme of Fig. 9.4f the tunneling is fast if the electron has spin-up, but becomes very slow if the spin was rotated. If the difference in tunnel rates is large enough, and $\Gamma_\uparrow \gg f_{rep}/2 \sim \Gamma_\downarrow$, then during a large part of the read-out stage there will be one electron on the dot if the electron was spin-down, and zero electrons if the electron was spin-up. Again, with the QPC we can measure this difference in charge.

We now estimate the minimum field strength of B_{ac} necessary to observe the resonance signal using transport as in Fig. 9.4d. The peak in the current has to exceed about 16 fA (the smallest detectable current in our setup). The current can be written as

$$I = e <n> f_{rep} = e\ P_\downarrow\ n_\downarrow\ f_{rep}, \tag{9.1}$$

where f_{rep} is the pulse repetition frequency and $<n>$ the average number of electrons transported per pulse cycle, which is the product of $P_\downarrow$, the probability that the spin is down at the start of the read-out stage, and $n_\downarrow$, the average number of electrons transported during the read-out stage for $P_\downarrow = 1$. Assuming we apply B_{ac} for 20 ns, which is on the order of the expected T_2, then wait 10 ns for the excitations to disappear, and use 70 ns for the read-out stage, the repetition frequency of the pulse train will be 10 MHz. The tunnel rate for spin-down in
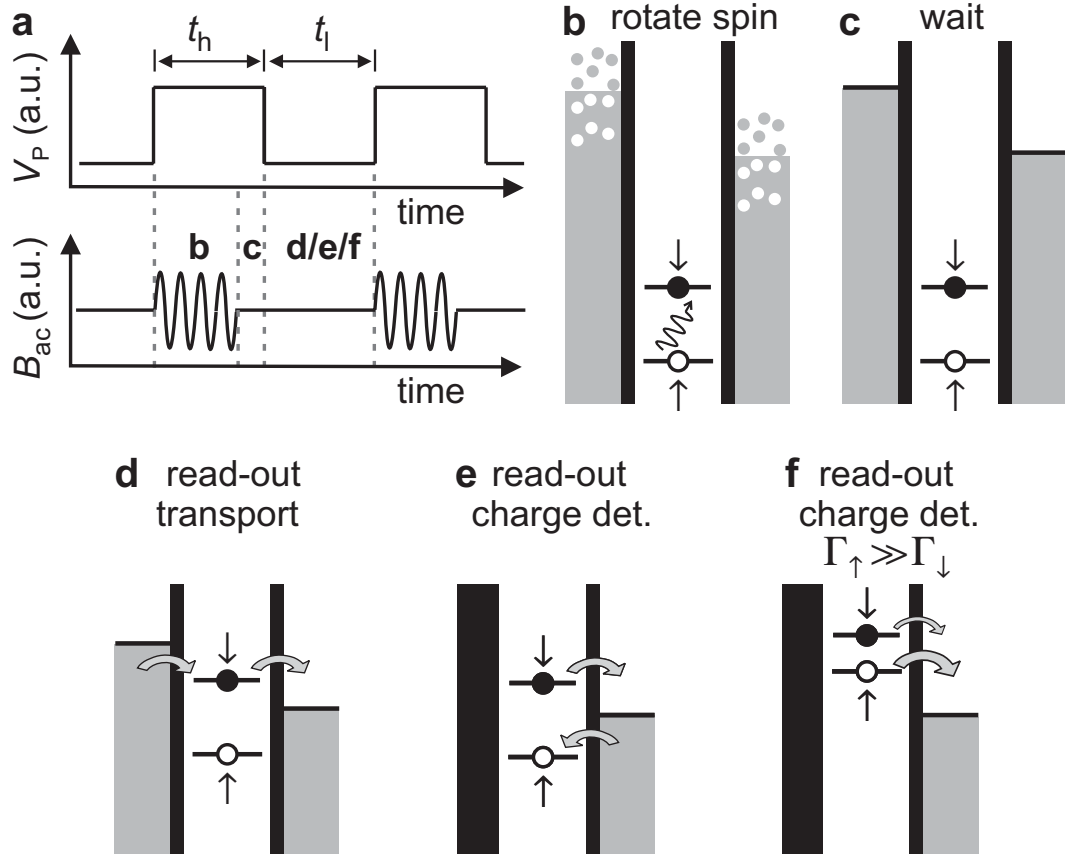
Figure 9.4: Detection of pulsed ESR. **(a)** The pulse amplitude V_P and the applied microwave field B_{ac} as a function of time. **(b)** The spin is rotated by B_{ac} when the levels are in Coulomb blockade. **(c)** Then B_{ac} is turned off, and the excited electrons in the leads relax. In the last part, the levels are brought in the read-out configuration. If the spin was rotated it results in **(d)** a change in the current due to a difference in energy, or in a change in the average charge on the dot caused by **(e)** a difference in energy or **(f)** a difference in tunnel rate.

Fig. 9.4d has to be least 50 MHz, to make sure the electron will have enough time to tunnel off the dot during the read-out stage. Then, $<n>$ needs to be at least 16 fA/(ef_{rep})=0.01. If $\Gamma_\uparrow = \Gamma_\downarrow$, $n_\downarrow$ will be of order 1, and therefore $P_\downarrow$ has to exceed 0.01, implying that the spin has to be rotated over an angle of about 6 degrees within 20 ns (assuming every cycle starts with a spin-up electron). The Rabi frequency f_{Rabi} then has to be at least 6/(360·20 ns)≈ 0.8 MHz, corresponding to a value for B_{ac} of about 0.13 mT. If B_{ac} is 1 mT, the expected current is 64 times as high (1 pA).

If the tunnel rates are spin-dependent ($\Gamma_\uparrow > \Gamma_\downarrow$), the signal can be increased by performing the experiment at the 1↔2 electron transition. The scheme is

completely similar, except that for the same f_{Rabi}, $<n>$ will be larger because $n_\uparrow$, the equivalent of $n_\downarrow$, can be much larger than 1.

In both schemes using charge detection, we can increase the signal-to-noise ratio by using lock-in detection of I_{QPC} at the pulse repetition frequency (see chapter 6). The drawback is that the pulse repetition frequency is then limited to the bandwidth of the wiring in our dilution fridge, which is about 100 kHz. More analysis is needed to find the resulting strength of the ESR signal for these charge detection schemes.

Finally, we would like to detect ESR using single-shot read-out. Finding the resonance this way is very time-consuming and can be more easily done using one of the techniques described above. However, at the resonance the single-shot measurement will allow us to map out the Rabi oscillation in time, and perform more advanced rotations such as a spin-echo.

9.3 Two-spin experiments

9.3.1 Two-spin quantum gate: SWAP

The goal of the two-spin experiments is to demonstrate the operation of the SWAP gate, which exchanges ('swaps') the states of the two spins. This two-spin operation can be explored independently of the single-spin rotations. Only for the demonstrating of a quantum-CNOT gate [1], we will need both $\sqrt{\text{SWAP}}$ operations and single-spin rotations.

The SWAP gate can be conveniently understood as follows. The two spins are initially uncoupled and reside in the single dot orbital eigenstates. When the tunnel coupling becomes nonzero due to a voltage pulse on a gate, the new eigenstates are the two-electron spin singlet state $|S\rangle = (|\uparrow\downarrow\rangle - |\downarrow\uparrow\rangle)/\sqrt{2}$ and the spin triplets $|T_+\rangle = |\uparrow\uparrow\rangle$, $|T_0\rangle = (|\uparrow\downarrow\rangle + |\downarrow\uparrow\rangle)/\sqrt{2}$ and $|T_-\rangle = |\downarrow\downarrow\rangle$. Here, the orbital part of the wave function is built up from combinations of the single-dot orbitals (see e.g. Ref. [41]). The energy difference between the singlet and the triplets is the (time-dependent) Heisenberg exchange energy $J(t)$. Now, if initially the electrons had opposite spin, we can write the two-electron spin state as

$$|\uparrow\downarrow\rangle = (|\uparrow\downarrow\rangle - |\downarrow\uparrow\rangle + |\uparrow\downarrow\rangle + |\downarrow\uparrow\rangle)/2 = (|S\rangle + |T_0\rangle)\sqrt{2}. \tag{9.2}$$

Thus the spins start in a superposition of a singlet and a triplet state. The relative phase between the two parts of the superposition will change according to their energy difference $J(t)$ (i.e. the state precesses in the new eigenbasis):

$$(|S\rangle + |T_0\rangle)/\sqrt{2} \rightarrow (|S\rangle + e^{-i \int J(t)dt/\hbar} |T_0\rangle)/\sqrt{2}. \tag{9.3}$$

After a time t_{SWAP}, defined by $\int_0^{t_{SWAP}} J(t)/\hbar\, dt = \pi$, the state has evolved to

$$(|S\rangle + e^{-i\pi}|T_0\rangle)/\sqrt{2} = (|S\rangle - |T_0\rangle)/\sqrt{2} = |\downarrow\uparrow\rangle, \qquad (9.4)$$

and the states of the two spins have been swapped. The whole period between $t = 0$ and $t = t_{SWAP}$, the two spins are entangled. Note that the important parameter here is the *integral* over $J(t)$, not its maximum value. If the two spins initially carry the same spin, they are already in a two-spin eigenstate ($|T_+\rangle$ or $|T_-\rangle$), and the SWAP operation does not change the spin states, so entanglement will arise.

The scheme for measuring the coherent oscillation between the spins follows straightforwardly from the above. We prepare qubit 1 in state $|\uparrow\rangle$ and qubit 2 in $|\downarrow\rangle$. Measurement of qubit 1 should then always give $|\uparrow\rangle$, while measurement of qubit 2 should give $|\downarrow\rangle$. Now, we pulse the tunnel barrier separating the two dots for a specified time t_{pulse}, and read out the spin states. On repeating this measurement for many values of t_{pulse}, we will find the probabilities of qubit 1 and 2 to be in $|\uparrow\rangle$ and $|\downarrow\rangle$ respectively to oscillate in phase with the frequency J/h as a function of t_{pulse}. (The control measurements for the other combinations of initial spin states can be done similarly.) These two-spin operations will yield the coherence time, the value of J, and most importantly, the basic resource for quantum computing: entanglement of electrons!

9.3.2   Measurement of Bell's inequalities

The presence of entanglement can be experimentally verified by performing a test of the well-known Bell's inequalities [16]. A violation of Bell's inequalities in the solid state has not yet been measured, partly because there it is very hard, due to the strong interactions, to separate entangled particles and subsequently measure the entangled property in different bases. There exist numerous proposals for demonstrating entanglement using noise, see e.g. Ref. [49] for an overview, but we will focus here on single measurements of the spin. We give a short overview of the ingredients necessary for a measurement of Bell's inequalities for entangled electron spins and their possible implementations. (We leave the issues of spin decoherence and relaxation aside).

Entangled particles

First of all, we need to entangle the spin states of the electrons. As was shown in the previous section, two electrons in a double quantum dot can be entangled by a nonzero tunnel coupling between the dots. We can simply start with a large

tunnel coupling, such that the electrons are in the singlet ground state, which is maximally entangled [16]. Then, we decrease the tunnel coupling to zero by changing the gate voltage that controls the tunnel barrier between the two dots. This leaves us with two electrons, separated by a large barrier and maximally entangled.

Channels to separate the particles

The Bell test requires the particles to be far enough apart that no interaction can be present between the two. In order to ascertain that the interaction between the electrons is minimized, we want to move the electrons to different places in the device. To test the presence of nonlocal correlations, the time between the measurements on the two particles needs in principle to be shorter than the shortest time needed for the two particles to exchange information (i.e. their distance divided by the speed of light). In the devices that we use, this requirement can not be fulfilled unless we convert the electron spin information to photons (research on semiconductor nanowires in our group has exactly this goal). Here we leave this requirement aside and only desire the particles to be separated over a 'macroscopic' length scale, say several micrometers. Of course, transporting one electron away from the double dot is sufficient. Note that the quantum information has to be preserved during this transportation.

A narrow channel can be created electrostatically by using the surface depletion gates. This channel can be completely emptied of electrons, and can easily connect to a quantum dot several micrometers away. We are currently investigating whether we can transport single electrons through such a channel without destroying the spin information. Possible problems include the roughness of the potential landscape, that can localize electrons within the channel, or the spin-orbit interaction, which is possibly much larger than in the zero-dimensional case [25]. (The transport of single electrons from a double dot to a quantum point contact via a 'quantum channel' for a Bell test has been extensively analyzed in Ref. [50].)

Another possibility is the use of edge channels in the Quantum Hall regime. These channels follow equipotential lines, and momentum scattering is strongly suppressed. Extraction of the electron from the channel into another quantum dot might be possible if the energy of the electron is much higher than the Fermi energy in the edge channels, and energy relaxation does not occur during the transportation time. However, this still looks problematic since the tunnel probability into the dot is very small, and the electron will need to be allowed many attempts before it will have tunneled into the dot with a high probability. Also,
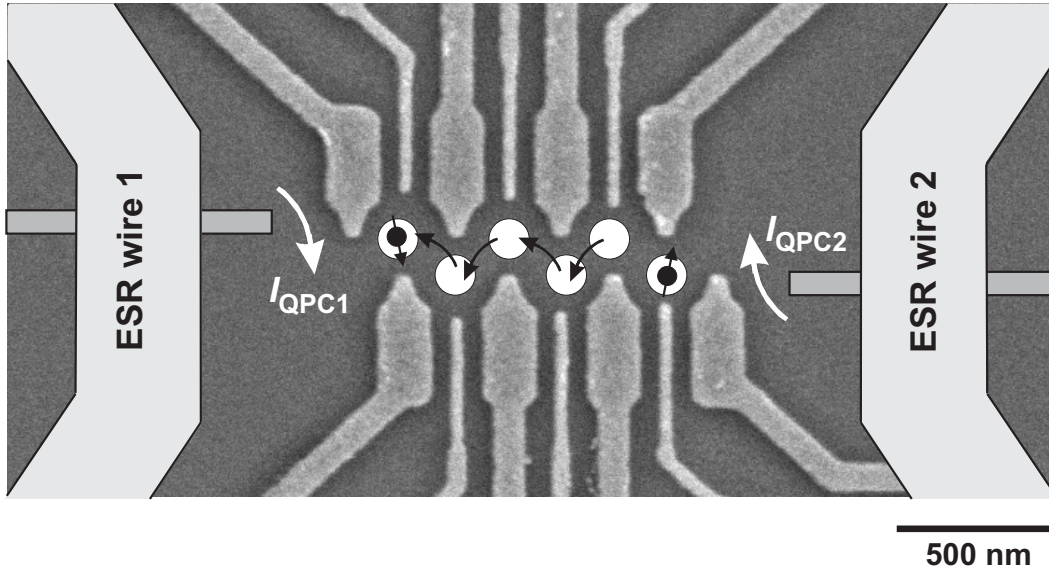
Figure 9.5: Possible device lay-out for a Bell test on two entangled electron spins. The basis of this layout is an Scanning Electron Micrograph of a device that allows six coupled dots to be formed (device was fabricated by Wilfred van der Wiel and Ronald Hanson at NTT Basic Research Laboratories). The two electrons are first entangled in the two neighboring dots on the right via the inter-dot tunnel coupling. Then, one electron is transported to the other end of the array. The spins can be selectively rotated using the oscillating magnetic field generated by the two ESR wires. Finally, we can read out the spins using spin-to-charge conversion and the two QPCs as electrometers.

it is not clear how the interaction with the other electrons in the edge channel will effect the coherence.

Finally, we could use an array of dots, and transfer one electron to the other side of the array by simply raising the electrochemical potentials in the dots one by one, such that the electron 'hops' from one dot to the next. An example of such an array containing six dots is shown in Fig. 9.5, where the maximum distance between the electrons is about one micrometer. Quantum point contacts located next to the dots can monitor the movements of the electron while it is being transferred along the array.

Read-out in different bases

When the electrons are spatially separated, we have to read out their electron spins in different bases [16]. The two read-out methods that we have at hand both project the spin state onto the eigenstates $|\uparrow\rangle$ and $|\downarrow\rangle$. To measure in a

different basis, we can rotate both spins just before reading them out using an ESR field (for a discussion on single-spin rotations see section 9.2). The choice of read-out method might also depend on the type of channel used. For instance, a perpendicular magnetic field is needed to create edge channels, and in that case the tunnel-rate selective read-out has to be used.

Summarizing, a measurement of Bell's inequalities could be performed by starting from a tunnel-coupled double dot, pinching off the tunnel barrier, then transferring one electron along an array of dots, and finally rotating the spins to a new basis and reading them out. A possible device lay-out for such an experiment is shown in Fig. 9.5. The only missing ability is the controlled rotation of the electron spins, which is likely to be achieved in the near future. Thus, we might soon be able to attempt a Bell test in the solid state!

9.4 Conclusions

The experimental research on using electron spins as quantum bits, which started only about three years ago, has already produced a number of exciting results, including isolation and read-out of a single electron spin. Experiments are now aimed at controlling the coherent properties of single spins as well as at creating and detecting entanglement between two spins. The ideas laid out in this chapter provide a detailed guide for experiments in the near future.

The question remains whether we will ever see a quantum computer based on electron spins in quantum dots. There are a number of fundamental issues, e.g. the hyperfine interaction and the scaling to more than ten qubits, that need to be resolved before we can start thinking about a true large-scale quantum computer. However, as these problems are being attacked, new theoretical ideas and experimental techniques will be developed, which are not only extremely valuable for future research on a spin quantum computer, but at the same time will yield more interesting and exciting physics.

References

[1] D. Loss and D.P. DiVincenzo, Phys. Rev. A **57**, 120 (1998).

[2] D.P. DiVincenzo, Fortschr. Phys. **48**, 771 (2000).

[3] J.M. Elzerman, R. Hanson, J.S. Greidanus, L.H. Willems van Beveren, S. De Franceschi, L.M.K. Vandersypen, S. Tarucha, and L.P. Kouwenhoven, Phys. Rev. B. **67**, 161308(R) (2003).

[4] L.P. Kouwenhoven, G. Schön, and L.L. Sohn, in *Mesoscopic Electron Transport*, Vol. 345 of *NATO Advanced Study Institute, Series E*, edited by L.L. Sohn, L.P. Kouwenhoven, and G. Schön (Kluwer Academic Publishers, Dordrecht, 1997).

[5] M. Field, C. G. Smith, M. Pepper, D. A. Ritchie, J. E. F. Frost, G. A. C. Jones, and D. G. Hasko, Phys. Rev. Lett. **70**, 1311 (1993).

[6] J.M. Elzerman, R. Hanson, L.H. Willems van Beveren, L.M.K. Vandersypen and L.P. Kouwenhoven, Appl. Phys. Lett. **84**, 4617 (2004).

[7] L.-X. Zhang, J. P. Leburton, R. Hanson and L. P. Kouwenhoven, Appl. Phys. Lett. **85**, 2628 (2004).

[8] R.J. Schoelkopf, P. Wahlgren, A.A. Kozhevnikov, P. Delsing, and D.E. Prober, Science **280**, 1238 (1998).

[9] L. M. K. Vandersypen, J. M. Elzerman, R. N. Schouten, L. H. Willems van Beveren, R. Hanson and L. P. Kouwenhoven, Appl. Phys. Lett. **85**, 4394 (2004).

[10] R. Hanson, B. Witkamp, L.M.K. Vandersypen, L.H. Willems van Beveren, J.M. Elzerman, and L.P. Kouwenhoven Phys. Rev. Lett. **91**, 196802 (2003).

[11] W.G. van der Wiel *et al.*, Rev. Mod. Phys. **75**, 1 (2003).

[12] M. Pioro-Ladrire, M. Ciorga, J. Lapointe, P. Zawadzki, M. Korkusinski, P. Hawrylak, and A. S. Sachrajda, Phys. Rev. Lett. **91**, 026803 (2003),

[13] J. R. Petta, A. C. Johnson, C. M. Marcus, M. P. Hanson, A. C. Gossard, Phys. Rev. Lett. **93**, 186802 (2004).

[14] T. H. Oosterkamp *et al.*, Nature **395**, 873 (1998).

[15] V.N. Golovach and D. Loss, Phys. Rev. B **69**, 245327 (2004).

[16] M.A. Nielsen, I.L. Chuang, *Quantum Computation and Quantum Information* (Cambridge U. Press, New York, 2000).

[17] M. Ciorga *et al.*, Phys. Rev. B **61**, R16315 (2000).

[18] M. Ciorga *et al.*, Appl. Phys. Lett. **80**, 2177 (2002).

[19] J.M. Elzerman, R. Hanson, L.H. Willems van Beveren, B. Witkamp, L.M.K. Vandersypen, and L.P. Kouwenhoven, Nature **430**, 431 (2004).

[20] M. Kroutvar, Y. Ducommun, D. Heiss, M. Bichler, D. Schuh, G. Abstreiter, and J. J. Finley, Nature **432**, 81 (2004).

[21] T. Fujisawa *et al.*, Nature **419**, 278 (2002).

[22] L.M.K. Vandersypen and I.L. Chuang, Rev. Mod. Phys. 76, 1034 (2004).

[23] R. Hanson *et al.*, submitted to Phys. Rev. Lett., see also cond-mat/0412768.

[24] J. M. Kikkawa and D. D. Awschalom, Phys. Rev. Lett. **80**, 4313 (1998).

[25] A.V. Khaetskii and Y.V. Nazarov, Phys. Rev. B **61**, 12639 (2000). A.V. Khaetskii and Y.V. Nazarov, Phys. Rev. B **64** 125316 (2001).

[26] V.N. Golovach, A. Khaetskii, and D. Loss, Phys. Rev. Lett. **93**, 016601 (2004).

[27] S.I. Erlingsson and Y.V. Nazarov, Phys. Rev. B **66**, 155327 (2002).

[28] A. V. Khaetskii, D. Loss, L. Glazman, Phys. Rev. Lett. **88**, 186802 (2002).

[29] I. A. Merkulov, Al. L. Efros, M. Rosen, Phys. Rev. B **65**, 205309 (2002).

[30] R. de Sousa and S. Das Sarma, Phys. Rev. B **67**, 033301 (2003).

[31] D. Paget, G. Lampel, B. Sapoval, and V. I. Safarov, Phys. Rev. B **15**, 5780 (1977).

[32] K. Ono, D. G. Austing, Y. Tokura and S. Tarucha, Science **297**, 1313 (2002). K. Ono and S. Tarucha, Phys. Rev. Lett. **92**, 256803 (2004).

[33] A. C. Johnson, J. R. Petta, C. M. Marcus, M. P. Hanson and A. C. Gossard, cond-mat/0410679 (2004).

[34] G. Burkard, D. Loss, and D. P. DiVincenzo, Phys. Rev. B **59**, 2070 (1999).

[35] D. P. DiVincenzo, D.P. Bacon, D.A. Lidar, and K.B. Whaley, Nature **408**, 339 (2000).

[36] M. Dobers, K. v. Klitzing and G. Weimann, Phys. Rev. B **38**, 5453 (1988).

[37] Y. Kato, R. C. Myers, A. C. Gossard and D. D. Awschalom, Science **299**, 1201 (2003).

[38] G. Salis *et al.*, Nature (London) **414**, 619 (2001).

[39] T. Hayashi, T. Fujisawa, H.D. Cheong, Y.H. Jeong, and Y. Hirayama, Phys. Rev. Lett. **91**, 226804 (2003).

[40] S.W. Jung, T. Fujisawa, Y. Hirayama and Y. H. Jeong, Appl. Phys. Lett. **85**, 768 (2004).

[41] G. Burkard, PhD thesis '*Quantum Computation and Communication using Electron Spins in Quantum Dots and Wires*, University of Basel (2001).

[42] X. Hu, R. de Sousa and S. Das Sarma, Phys. Rev. Lett. **86**, 918 (2001).

[43] J.D. Jackson, *Classical electrodynamics*, Wiley, New York (1998).

[44] L. M. K. Vandersypen *et al.*, in *Quantum Computing and Quantum Bits in Mesoscopic Systems*, Kluwer Academic, New York (2003) (see also quant-ph/0207059).

[45] J. J. Wever, M. Sc. thesis, Delft University of Technology (2003).

[46] H. A. Engel and D. Loss, Phys. Rev. Lett. **86**, 4648 (2001); H. A. Engel and D. Loss, Phys. Rev. B **65**, 195321 (2002).

[47] I. Martin, D. Mozyrsky, and H.W. Jiang, Phys. Rev. Lett. **90**, 018301 (2003).

[48] M. Xiao, I. Martin, E. Yablonovitch, and H.W. Jiang, Nature **430**, 435 (2004).

[49] D. Loss and E.V. Sukhorukov, Phys. Rev. Lett. **84**, 1035 (2000).

[50] M. Blaauboer and D. P. DiVincenzo (unpublished).

Appendix A

Extracting tunnel rates from the electron response to a pulse train

In this Appendix, we derive an analytical expression for the electron response to a pulse train, measured using a lock-in amplifier operated at the frequency of the pulse train. We show that such measurements allow us to determine the tunnel rates for ground and excited states.

A.1 Dot occupation probability with a pulse train applied

The waveform of the applied voltage pulse train is shown in Fig. A.1a. We start by calculating the probability $P_e(t)$ that the dot does *not* contain an extra electron at time t. Each cycle of the voltage pulse train, which has a repetition frequency $f_{rep} = 1/2\tau$, consists of two parts: the high phase ($0 \leq t \leq \tau$), where one electron can tunnel onto the dot and the low phase ($\tau \leq t \leq 2\tau$), where one electron can tunnel off the dot (see the energy diagrams in Fig. A.1a). We denote the total tunnel rate and P_e in the high (low) phase as Γ_h (Γ_l) and $P_{e,h}(P_{e,l})$, respectively. We start with writing down $P_e(t)$ for the two phases separately:

$$P_{e,h}(t) = P_{e,h}(0) \cdot e^{-\Gamma_h t}, \qquad for\ t \in [0, \tau], \tag{A.1}$$

$$P_{e,l}(t) = 1 - (1 - P_{e,l}(\tau)) \cdot e^{-\Gamma_l(t-\tau)}, \quad for\ t \in [\tau, 2\tau]. \tag{A.2}$$

Now we have to find $P_{e,h}(0)$ and $P_{e,l}(\tau)$. In the steady state, the probability function is continuous. Thus, there is only one value for $P_e(t)$ at any time t. This implies

$$P_{e,h}(0) = P_{e,l}(2\tau), \tag{A.3}$$

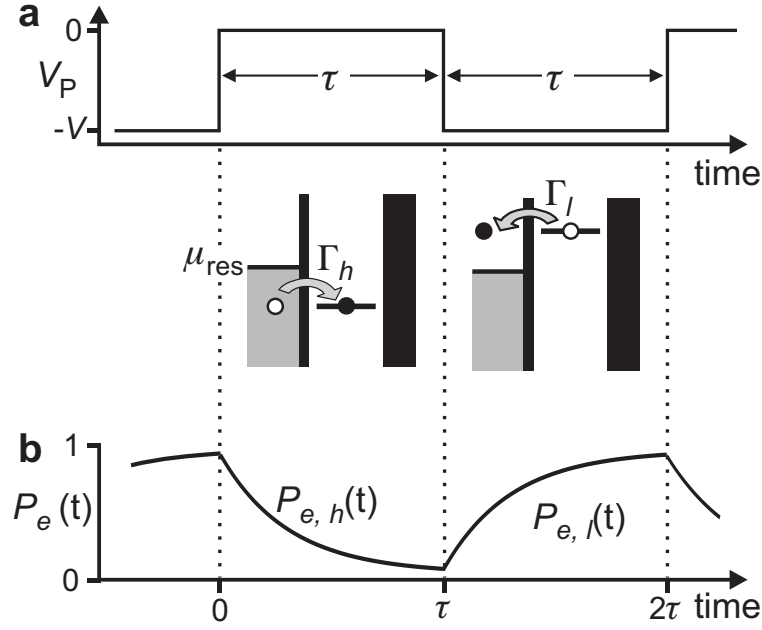$$P_{e,h}(\tau) = P_{e,l}(\tau). \tag{A.4}$$

Figure A.1: (a) Pulse waveform applied to the gate, with the resulting level configurations in the dot indicated. **(b)** The probability $P_e(t)$ that the dot does not contain an extra electron as a function of time, for $\Gamma \sim 1/\tau$.

Solving these equalities yields the values of $P_e(t)$ at $t = (0, 2\tau)$ and $t = \tau$:

$$P_e(0) \;=\; P_e(2\tau) = \frac{1 - e^{-\Gamma_l \tau}}{1 - e^{-(\Gamma_h + \Gamma_l)\tau}}, \tag{A.5}$$

$$P_e(\tau) \;=\; e^{-\Gamma_h \tau} \cdot P_e(0) \;=\; \frac{e^{-\Gamma_h \tau} - e^{-(\Gamma_h + \Gamma_l)\tau}}{1 - e^{-(\Gamma_h + \Gamma_l)\tau}}. \tag{A.6}$$

With this, we know the value of P_e for the whole cycle. In Fig. A.1b, P_e is shown as a function of time for $\Gamma_h, \Gamma_l \sim 1/\tau$.

A.2 Lock-in amplifier signal due to electron tunneling

The current through the QPC, I_{QPC}, is directly related to the probability P_e: $\Delta I_{QPC} = C \cdot P_e$, where C denotes the maximum electron response (see Fig. 6.1c). The lock-in amplifier multiplies I_{QPC} with a sine function of frequency f_{rep} and integrates the corresponding signal. This way, only fluctuations in I_{QPC} at the frequency f_{rep} lead to a nonzero output value. We now calculate the lock-in amplifier signal (LAS) using the probability function P_e obtained in the previous

section:

$$
\begin{aligned}
LAS &= \frac{C}{2\tau} \int_0^{2\tau} P_e(t) \cdot sin\left(\frac{t\pi}{\tau}\right) dt \\
&= \frac{C}{2\tau} \int_0^{\tau} P_{e,h}(t) \cdot sin\left(\frac{t\pi}{\tau}\right) dt + \frac{C}{2\tau} \int_\tau^{2\tau} P_{e,l}(t) \cdot sin\left(\frac{t\pi}{\tau}\right) dt \quad \text{(A.7)}
\end{aligned}
$$

The first part of this integral is

$$
\frac{C}{2\tau} \int_0^{\tau} P_e(0) \cdot e^{-\Gamma_h t} \cdot sin\left(\frac{t\pi}{\tau}\right) dt = \frac{CP_e(0)}{2} \frac{\pi}{\Gamma_h^2\tau^2 + \pi^2} \left(e^{-\Gamma_h\tau} + 1\right) \quad \text{(A.8)}
$$

The second part gives

$$
\begin{aligned}
\frac{C}{2\tau} &\int_\tau^{2\tau} \left(1 - (1 - P_e(\tau)) \cdot e^{-\Gamma_l(t-\tau)}\right) \cdot sin\left(\frac{t\pi}{\tau}\right) dt \\
&= \frac{C(1 - P_e(\tau))}{2} \frac{\pi}{\Gamma_l^2\tau^2 + \pi^2} \left(e^{-\Gamma_l\tau} + 1\right) - \frac{C}{\pi} \quad \text{(A.9)}
\end{aligned}
$$

We see that the LAS is 0 for $\Gamma_l, \Gamma_h \ll 1/\tau$, and is C/π for $\Gamma_l, \Gamma_h \gg 1/\tau$.

For the case $\Gamma_h = \Gamma_l = \Gamma$,

$$
P_e(0) = 1 - P_e(\tau) = \frac{1 - e^{-\Gamma\tau}}{1 - e^{-2\Gamma\tau}} = \frac{1}{1 + e^{-\Gamma\tau}}, \quad \text{(A.10)}
$$

and Eq. A.7 is reduced to the simple expression

$$
LAS = \frac{C}{\pi} \left(\frac{\pi^2}{\Gamma^2\tau^2 + \pi^2} - 1\right) \quad \text{(A.11)}
$$

From this equation, we find that the LAS is maximally sensitivity to changes in Γ when $\Gamma = \pi/(\sqrt{3}\tau)$ and LAS is 0.25 of the maximum response C/π. In Fig. A.2a we plot the LAS as a function of the asymmetry in the tunnel rates Γ_l/Γ_h, with Γ_h set to $\pi/(\sqrt{3}\tau)$.

A.3 Extracting tunnel rates from the lock-in signal

In Fig. A.2b the LAS is plotted as a function of Γ, with $\Gamma_h = \Gamma_l = \Gamma$. By comparing the measured value of LAS for a certain τ to the values in this plot, one can determine the tunnel rate. Furthermore, by increasing the pulse amplitude, an excited state can be made to enter the pulse window. From the resulting change in LAS, the tunnel rate for this extra level can be deduced. Finally, when an
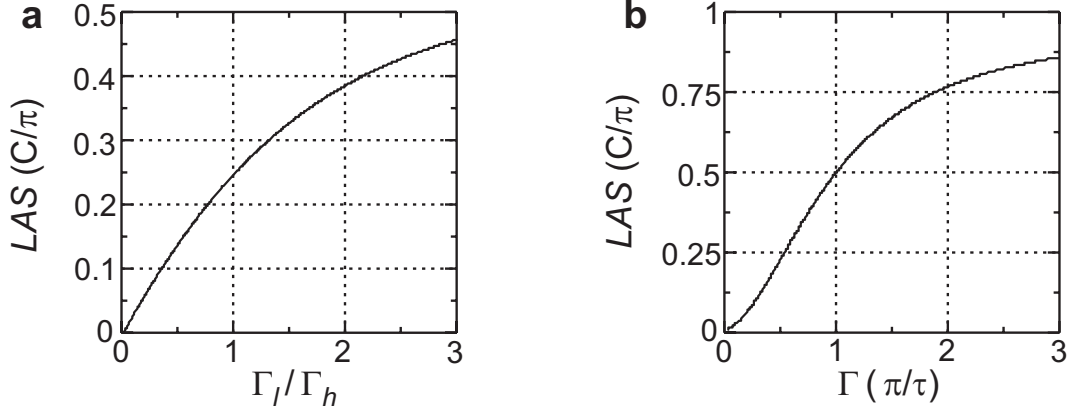
Figure A.2: **(a)** Lock-in amplifier response signal (LAS) to a voltage pulse train, as a function of the tunnel rate asymmetry Γ_l/Γ_h. Here, Γ_h is fixed to $\pi/(\sqrt{3}\tau)$. **(b)** LAS as a function of Γ, for $\Gamma_h=\Gamma_l=\Gamma$.

electron entering the excited state relaxes to the ground state in a time much shorter than τ, it will tunnel out again with a rate corresponding to the ground state. In this case the tunnel rates Γ_h and Γ_l will not be the same. As one now decreases τ to a value much shorter than the relaxation time, this difference will gradually disappear. Thus, from the dependence of the tunnel rate asymmetry on τ, this relaxation time can be extracted.

Summary

Electron spins in semiconductor quantum dots

This thesis describes a series of experiments aimed at understanding and controlling the behavior of the spin degree of freedom of single electrons, confined in semiconductor quantum dots. This research work is motivated by the prospects of using the electron spin as a quantum bit (qubit), the basic building block of a quantum computer. Here, the envisioned basis states (logical 0 and 1) of the qubit are the two possible orientations of the spin in a magnetic field: 'spin-up' (parallel to the field) and 'spin-down' (anti-parallel to the field). In this thesis, a number of important steps towards the use of electron spins as qubits are reported: the isolation of a single electron in a quantum dot, energy spectroscopy of the electron spin states, development of a new technique to probe a nearly-isolated quantum dot, 'single-shot' read-out of the electron spin orientation, and increased understanding of the interaction of the electron spin with its environment.

A quantum dot can be thought of as a small 'box' filled with a controllable number of electrons. This box is coupled via tunnel barriers to reservoirs, with which electrons can be exchanged, and is coupled capacitively to one or more gate electrodes that allow the number of electrons on the dot to be varied. Due to the small dot size (typically ~ 50 nm), comparable to the Fermi wavelength of the electrons, it exhibits a discrete energy spectrum. The quantum dot devices studied in this work are defined in a two-dimensional electron gas (2DEG) of a GaAs/AlGaAs heterostructure, by applying negative voltages to metallic gate electrodes fabricated on top of the heterostructure.

The electronic properties of a quantum dot are conventionally studied by looking at the transport of electrons through the dot. A bias voltage is applied over the device, and the resulting current flowing through it is measured. The dependence of the current on bias voltage and on the voltage that is applied to the surface gates provide detailed information on the energy level spectrum and the coupling of the different states to the reservoirs.

The basic 'hardware' for all the experiments is a small circuit that consists of two coupled quantum dots, each flanked by a Quantum Point Contact (QPC). A QPC is a narrow channel in the 2DEG, of which the conductance can be made very sensitive to the electrostatic environment. By applying a bias voltage over the constriction, and measuring the resulting current flowing through it, the QPC is operated as an electrometer and allows the detection of changes in the number of electrons on the nearby quantum dot.

Complete control over the number of electrons (down to zero) on each of the two coupled dots is demonstrated, using both charge detection and transport measurements. Even in the few-electron regime, the coupling between the two dots as well as the coupling to the reservoirs remain fully tunable. By increasing the bandwidth of the electrometer to about 40 kHz, single-electron tunneling on and off the dot is observed in real time.

The spin states of a one- and a two-electron quantum dot are first investigated using transport measurements. By applying a large magnetic field parallel to the 2DEG, the Zeeman energy splitting of a single electron is measured directly. Furthermore, a lower bound on the spin relaxation time of 50 μs is found by using fast voltage pulses. In the two-electron dot, both the spin-singlet ground state as well as the Zeeman-split spin-triplet excited states are identified. The measurements demonstrate that, in first order, a one-electron dot only allows spin-up electrons to pass, whereas a two-electron dot transmits only electrons with spin-down. Thus, a few-electron dot can be operated as an electrically tunable, bipolar spin filter.

Then, a new technique is developed for extracting all relevant parameters of the quantum dot using the QPC as an electrometer. The number of electrons on the dot and the tunnel rate between the dot and the reservoir can be determined even in the regime of very weak coupling of the dot to only one reservoir (this regime is inaccessible to transport measurements). The excited states can be identified by the changes they cause in the effective tunnel rate, allowing the complete energy level spectrum to be obtained.

Two methods are presented for reading out the electron spin state on a quantum dot, both relying on 'spin-to-charge' conversion. Here, the spin information is first converted to charge information by making the number of electrons on the dot dependent on the initial spin state. A subsequent fast measurement of the number of electrons on the dot using the QPC thus reveals the spin state.

The first method for spin-to-charge conversion relies on a large energy difference between the spin states, induced by an applied magnetic field. The levels are aligned such, that a spin-up electron is trapped on the dot, whereas a spin-down electron has enough energy to escape. Using this technique, read-out of an

individual electron spin is performed, with a single-shot measurement visibility up to 65%.

Alternatively, spin-to-charge conversion can be induced by spin-dependent tunnel rates. This method is applied to read out the two-electron spin state. Here, tunneling from a triplet state is about twenty times as fast as tunneling from a singlet state, resulting in a single-shot measurement visibility of more than 80%.

The read-out techniques also allow the spin relaxation times to be extracted. Both for a single spin and for the two-electron spin states, the relaxation is found to be very slow (relaxation times up to milliseconds). These long times, five orders of magnitude longer than the typical orbital relaxation time for an electron in a dot, indicate that the electron spin degree of freedom is well isolated from the environment. A strong magnetic field dependence suggests that the spin-orbit interaction is the dominant relaxation mechanism.

Finally, the progress on the 'electron spin qubit' proposal is reviewed, and the important problems are identified and critically analyzed. A number of key experiments are proposed for the demonstration of coherent control over the spin state and the presence of entanglement.

<div align="right">

Ronald Hanson

January 2005

</div>

Samenvatting

Elektronenspins in halfgeleider quantum dots

Dit proefschrift beschrijft een reeks experimenten, die het doel hebben om het gedrag van de spinvrijheidsgraad van enkele elektronen, opgesloten in een halfgeleider quantum dot, te begrijpen en onder controle te krijgen. De motivatie voor dit onderzoek is de mogelijke toepassing van de spin van een elektron als quantum bit (of qubit), de elementaire bouwsteen van een quantum computer. De beoogde basistoestanden van de qubit (de logische 0 en 1) komen overeen met de twee mogelijke richtingen van de spin van een elektron in een magneetveld: 'spin-omhoog' (parallel aan het magneetveld) en 'spin-omlaag' (antiparallel aan het magneetveld). In dit proefschrift wordt verslag gedaan van een aantal belangrijke stappen richting het gebruik van de spin van elektronen als qubits: opsluiting van een enkel elektron in een quantum dot, energie spectroscopie van de spintoestanden van het elektron, de ontwikkeling van een nieuwe techniek waarmee een bijna-geïsoleerde quantum dot kan worden onderzocht, uitlezing van de spintoestand van een elektron in een enkele meting, en kennis over de interactie van de spin van het elektron met de omgeving.

Een quantum dot kan worden beschouwd als een klein 'doosje' gevuld met een regelbaar aantal elektronen. Dit doosje is via tunnel barrières gekoppeld aan reservoirs, waarmee elektronen kunnen worden uitgewisseld, en het is capacitief gekoppeld aan één of meer 'gate' elektroden waarmee het elektronenaantal op de dot gevarieerd kan worden. Vanwege de kleine afmetingen van de dot (typisch ~ 50 nm), vergelijkbaar met de Fermi golflengte van de elektronen, vertoont de dot een discreet energie spectrum. De in dit werk bestudeerde quantum dots zijn gedefinieerd in een tweedimensionaal elektronengas (2DEG) van een GaAs/AlGaAs heterostruktuur, door negatieve spanningen aan te brengen op metalen 'gate' elektroden bovenop de heterostruktuur.

De conventionele manier om de elektronische eigenschappen van een quantum dot te bestuderen is door te kijken naar het transport van elektronen door de dot. Een spanningsverschil wordt aangelegd over de structuur, en de stroom die er als

gevolg doorheen vloeit wordt gemeten. De afhankelijkheid van die stroom van het aangelegde spanningsverschil en de spanning op de 'gate' elektroden geeft gedetailleerde informatie over het spectrum van energieniveaus en de tunnelkoppeling naar de reservoirs.

De basis 'hardware' voor alle experimenten is een structuur bestaande uit twee gekoppelde quantum dots, elk geflankeerd door een quantum puntcontact (QPC). Een QPC is een nauw kanaaltje in het 2DEG, waarvan de geleiding erg gevoelig gemaakt kan worden voor de elektrostatische omgeving. Door een spanningsverschil aan te leggen over het kanaaltje, en de resulterende stroom die er doorheen loopt te meten, kan de QPC worden gebruikt als een ladingsmeter en kunnen veranderingen in het aantal elektronen op de vlakbij gelegen dot worden gedetecteerd.

Volledige controle over het aantal elektronen (tot aan nul) op elk van de twee gekoppelde dots is aangetoond, zowel met ladingsmetingen als met transportmetingen. Zelfs met nog maar een paar elektronen op de dots blijven zowel de tunnelkoppeling tussen de dots als de tunnelkoppeling naar de reservoirs volledig instelbaar. Met een verhoogde bandbreedte van de ladingsmeter (ongeveer 40 kHz) is het tunnelen van een enkel elektron naar en van de dot geobserveerd in 'real-time'.

De spintoestanden in een één-elektron en een twee-elektron dot zijn eerst onderzocht met transportmetingen. In een sterk magneetveld, aangelegd in het vlak van het 2DEG, is de Zeemanenergie van een enkel elektron op een directe manier gemeten. Bovendien is voor de spinvervaltijd, welke aangeeft op welke tijdschaal een 'spin-omlaag' toestand vervalt naar de grondtoestand 'spin-omhoog', een ondergrens van 50 microseconden gevonden. In een dot met twee elektronen zijn zowel de spin-singlet grondtoestand als de door Zeemanenergie gesplitste spin-triplet aangeslagen toestanden geïdentificeerd. De metingen laten zien dat een dot met één elektron alleen elektronen met 'spin-omhoog' doorlaat, terwijl een dot met twee elektronen alleen elektronen met 'spin-omlaag' doorlaat. Derhalve kan een dot met enkele elektronen gebruikt worden als een elektrisch regelbaar, bipolair spinfilter.

Een nieuwe techniek is ontwikkeld waarmee alle relevante parameters van de quantum dot te bepalen zijn. Het aantal elektronen op de dot en de tunnelfrequentie tussen de dot en het reservoir kunnen ermee worden bepaald, zelfs in het regime waarin de dot zeer zwak gekoppeld is naar maar één reservoir, een regime dat niet toegankelijk is voor conventionele transportexperimenten. De aangeslagen toestanden kunnen worden geïdentificeerd door de verandering die ze veroorzaken in de effectieve tunnelfrequentie te meten, zodat het complete energiespectrum kan worden verkregen.

Twee methodes worden gepresenteerd waarmee de spintoestand op de quantum dot kan worden uitgelezen, beiden gebruik makend van 'spin-naar-lading conversie'. Hierin wordt de spininformatie eerst omgezet naar ladingsinformatie, door het aantal elektronen op de dot afhankelijk te maken van de initiële spintoestand. Vervolgens onthult een snelle meting van het aantal elektronen op de dot met behulp van de QPC de spintoestand.

De eerste methode voor 'spin-naar-lading conversie' berust op een groot verschil in energie tussen de spintoestanden als gevolg van een aangelegd magneetveld. De niveaus van de spintoestanden worden zo gepositioneerd dat een elektron vastzit op de dot als het 'spin-omhoog' heeft, terwijl een elektron de dot kan verlaten als het 'spin-omlaag' heeft. Met deze techniek is het gelukt de spinrichting van een enkel elektron uit te lezen, met een enkele-meting nauwkeurigheid tot aan 65%.

De 'spin-naar-ladings conversie' kan op een andere manier worden gerealiseerd met behulp van tunnelfrequenties die afhangen van de spintoestand. Deze methode is toegepast op de uitlezing van de spintoestand van twee elektronen. De tunnelfrequentie van een spin-triplet is twintig maal zo hoog als die van een spinsinglet, wat resulteert in een enkele-meting nauwkeurigheid boven de 80%.

Met deze uitleestechnieken kunnen ook de spinvervaltijden worden bepaald. Zowel voor een enkele spin als voor de spintoestanden van twee elektronen is een zeer langzaam verval gevonden (vervaltijden tot aan milliseconden). Deze vervaltijden, vijf ordegroottes langer dan de typische baanvervaltijden van een elektron in een dot, geven aan dat de spinvrijheidsgraad van een elektron goed geïsoleerd is van de omgeving. De sterke magneetveldafhankelijkheid suggereert dat spin-baan interactie het dominante vervalmechanisme is.

Tot slot is een overzicht gegeven van de vooruitgang op het 'elektron spin qubit' gebied, en zijn de belangrijkste problemen geïdentificeerd en kritisch bekeken. Een aantal sleutelexperimenten is voorgesteld voor het aantonen van coherente controle over de spintoestand en de aanwezigheid van verstrengelde toestanden.

Ronald Hanson
januari 2005

Curriculum Vitae

Ronald Hanson

20-11-1976	Born in Groningen, the Netherlands.
1988-1994	Grammar school at the GSG in Emmen.
1994-1999	M.Sc. Applied Physics, University of Groningen. Graduate research in the group of prof. dr. ir. B. J. van Wees. Subject: Controllable supercurrent through a coupled SINIS-SNS Josephson junction.
1999-2000	Japan Prizewinners Programme, Leiden University and JNI, Japan. Including internship at Hitachi Advanced Research Labs, Japan.
2000-2005	Ph.D research at Delft University of Technology under supervision of prof. dr. ir. L. P. Kouwenhoven. Subject: Electron spins in semiconductor quantum dots. Including device fabrication at NTT Basic Research Labs, Japan.

List of publications

1. *Single-shot read-out of electron spin states in a quantum dot using spin-dependent tunnel rates*
   R. Hanson, L. H. Willems van Beveren, I. T. Vink, J. M. Elzerman, W. J. M. Naber, F. H. L. Koppens, L. P. Kouwenhoven, and L. M. K. Vandersypen,
   Submitted to Physical Review Letters.
   See also http://xxx.lanl.gov/abs/cond-mat/0412768 (2004).

2. *Experiments and simulations on a few-electron quantum dot circuit with integrated charge read-out*
   R. Hanson, J. M. Elzerman, L. H. Willems van Beveren, L. M. K. Vandersypen, L.-X. Zhang, P. Matagne, J. P. Leburton and L. P. Kouwenhoven,
   Proceedings of the 27th International Conference on the Physics of Semiconductors (2004) (in press).

3. *Semiconductor few-electron quantum dots as spin qubits*
   J. M. Elzerman, R. Hanson, L. H. Willems van Beveren, S. Tarucha, L. M. K. Vandersypen and L. P. Kouwenhoven,
   in *Quantum Dots: a Doorway to Nanoscale Physics*, Springer (2005).

4. *Semiconductor few-electron quantum dot operated as a bipolar spin filter*
   R. Hanson, L. M. K. Vandersypen, L. H. Willems van Beveren, J. M. Elzerman, I. T. Vink and L. P. Kouwenhoven,
   Physical Review B **70**, 241304(R) (2004).

5. *Semiconductor few-electron quantum dots as spin qubits*
   J. M. Elzerman, R. Hanson, L. H. Willems van Beveren, L. M. K. Vandersypen and L. P. Kouwenhoven,
   To appear in *Quantum Computation: solid state systems*, Kluwer Academic/Plenum Publishers (due 2005).

6. *Electron spin qubits in quantum dots*
   R. Hanson, J. M. Elzerman, L. H. Willems van Beveren, L. M. K. Vandersypen and L. P. Kouwenhoven,
   Technical Digest of the 2004 IEEE International Electron Devices Meeting.

7. *Real-time detection of single electron tunneling using a quantum point contact*
   L. M. K. Vandersypen, J. M. Elzerman, R. N. Schouten, L. H. Willems van Beveren, R. Hanson and L. P. Kouwenhoven,
   Applied Physics Letters **85**, 4394 (2004).

8. *Tunable few-electron double quantum dots with integrated charge read-out*
   J. M. Elzerman, R. Hanson, J. S. Greidanus, L. H. Willems van Beveren, S. De Franceschi, L. M. K. Vandersypen, S. Tarucha and L. P. Kouwenhoven,
   Physica E **25**, 135 (2004).

9. *Engineering the quantum point contact response to single-electron charging in a few-electron quantum dot circuit*
   L.-X. Zhang, J. P. Leburton, R. Hanson and L. P. Kouwenhoven,
   Applied Physics Letters **85**, 2628 (2004).

10. *Measurement efficiency and n-shot read out of spin qubits*
    H. A. Engel, V. N. Golovach, D. Loss, L. M. K. Vandersypen, J. M. Elzerman, R. Hanson and L. P. Kouwenhoven,
    Physical Review Letters **93**, 106804 (2004).

11. *Determination of the tunnel rates through a few-electron quantum dot*
    R. Hanson, I. T. Vink, D. P. DiVincenzo, L. M. K. Vandersypen, J. M. Elzerman, L. H. Willems van Beveren and L. P. Kouwenhoven,
    To appear in Proceedings of XXXIXth Rencontres de Moriond (2004).
    See also http://xxx.lanl.gov/abs/cond-mat/0407793 (2004).

12. *Single shot read-out of an individual electron spin in a quantum dot*
    J. M. Elzerman, R. Hanson, L. H. Willems van Beveren, B. Witkamp, L. M. K. Vandersypen and L. P. Kouwenhoven,
    Nature **430**, 431 (2004).

13. *Single-electron charging and detection in a laterally-coupled quantum dot circuit in the few-electron regime*
    L.-X. Zhang, P. Matagne, J. P. Leburton, R. Hanson and L. P. Kouwenhoven,
    Physical Review B **69**, 245301 (2004).

14. *Excited-state spectroscopy on a nearly-closed quantum dot via charge detection*
    J. M. Elzerman, R. Hanson, L. H. Willems van Beveren, L. M. K. Vandersypen and L. P. Kouwenhoven,
    Applied Physics Letters **84**, 4617 (2004).

15. *Zeeman energy and spin relaxation in a one-electron quantum dot*
R. Hanson, B. Witkamp, L. M. K. Vandersypen, L. H. Willems van Beveren,
J. M. Elzerman and L. P. Kouwenhoven,
Physical Review Letters **91**, 196802 (2003).

16. *Few-electron quantum dot circuit with integrated charge read-out*
J. M. Elzerman, R. Hanson, J. S. Greidanus, L. H. Willems van Beveren, S. De
Franceschi, L. M. K. Vandersypen, S. Tarucha and L. P. Kouwenhoven,
Physical Review B **67**, 161308 (2003).

17. *Quantum computing with electron spins in quantum dots*
L. M. K. Vandersypen, R. Hanson, L. H. Willems van Beveren, J. M. Elzerman,
J. S. Greidanus, S. De Franceschi and L. P. Kouwenhoven,
in *Quantum Computing and Quantum Bits in Mesoscopic Systems*, Kluwer Aca-
demic/Plenum Publishers (2003).
See also http://xxx.lanl.gov/abs/quant-ph/0207059 (2002).

18. *Out-of-equilibrium Kondo effect in a mesoscopic device*
S. De Franceschi, R. Hanson, W. G. van der Wiel, J. M. Elzerman, J. J. Wijp-
kema, T. Fujisawa, S. Tarucha and L. P. Kouwenhoven,
Physical Review Letters **89**, 156801 (2002).

19. *Investigation of ramp-type Josephson junctions with surfac-modified barriers*
Y. Soutome, R. Hanson, T. Fukazama, K. Saitoh, A. Tsukamoto, Y. Tarutani
and K. Takagi,
IEEE Transactions on Applied Superconductivity 11, 163 (2001).